Lubricant Behavior under Heat-Assisted Magnetic Recording (HAMR) Conditions

by

Mohammad Soroush Ghahri Sarabi

A dissertation submitted in partial satisfaction of the

requirements for the degree of

Doctor of Philosophy

in

Engineering - Mechanical Engineering

in the

Graduate Division

of the

University of California, Berkeley

Committee in charge:

Professor David B. Bogy, Chair

Professor Stephen Morris

Professor Per-Olof Persson

Spring 2017

The dissertation of Mohammad Soroush Ghahri Sarabi, titled Lubricant Behavior under Heat-Assisted Magnetic Recording Conditions, is approved:

Chair _____ Date 2-22-2017

_____ Date 2017. 02. 23

_____ Date 2/22/2017

University of California, Berkeley

Abstract

Lubricant Behavior under Heat-Assisted Magnetic Recording (HAMR) Conditions

by

Mohammad Soroush Ghahri Sarabi

Doctor of Philosophy in Mechanical Engineering

University of California, Berkeley

Professor David B. Bogy, Chair

In the developing Heat-Assisted Magnetic Recording (HAMR) technology, a laser heats up the magnetic media to the Curie temperature of a few hundred degrees Celsius for a few nanoseconds. Accordingly, the thin-film lubricant coating on the disk experiences severe thermal conditions leading to thermo-capillary and evaporation effects followed by its local depletion. The resulting non-uniform lubricant profile can cause slider modulations leading to poor HDD read/write performance. In order to maintain a reliable head-disk interface, the lubricant needs to return to the initial uniform profile, in a process known as lubricant reflow, driven by the inter-molecular forces. This dissertation is dedicated to modeling the behavior of the Perfluoropolyether (PFPE) lubricants under such conditions.

To study the lubricant depletion behavior, we employ a Finite Volume Method (FVM) combined with the lubrication theory to solve the lubrication equation for the Z-tetraol family of lubricants with 4 hydroxyl end-groups, including Z-tetraol 1200 with a low molecular weight and Z-tetraol 2200 with a high molecular weight, and also for ZTMD (2,200 Da) with 8 hydroxyl end-groups as a multi-dentate lubricant. All studies are performed for 4 initial film thicknesses of 5, 7, 12, and 14A. These numbers are chosen to provide a fair comparison with a previous study for Z-dol with 2 hydroxyl end-groups. Additionally, we investigate the relative effects of evaporation and thermo-capillary shear stress on lubricant depletion. It is found that after 2ns of laser irradiation, a trough and two side ridges across the down-track direction can be seen in the lubricant. The performances of the lubricants can be ranked mainly based on the trough depth and also evaporation such that better lubricants show less deformation and trough depth under equal conditions of thermal spot size and peak temperature. We also found that all of the lubricants deplete rapidly and their depletion rate decreases gradually.

To investigate the reflow performance of the lubricants, we perform numerical simulations (FVM) to solve the lubrication equation, which (in case of reflow) is similar to a nonlinear Fickian diffusion equation. Then, we compare the calculated recovery (or reflow) times for HDD lubricants with similar molecular weights. The lubricant reflow is modeled for a wide range of film thicknesses and laser spot sizes, based on published material properties obtained by experiments. From a design standpoint, the recovery time for the lubricants should be very short, and in particular, it should be shorter than the required time for one disk revolution, around 10-15ms. The results show that the recovery times for Z-tetraol 2200 and ZTMD are significantly longer than that for Z-dol 2000, while the recovery time for ZTMD is close to that for Z-tetraol, despite its higher viscosity value. This observation is due to the improved disjoining pressure properties for the multi-dentate ZTMD. It is also shown that all lubricants have an optimum film thickness for recovery time, and this optimum point largely depends on the dewetting and polar behavior of the lubricant.

In the first part of this dissertation, the effects of the laser irradiation on lubricant

depletion and recovery are investigated based on the assumption that the lubricant is an ultra-thin film viscous fluid and its behavior can be modeled using lubrication theory. This method is very well-established in the HDD industry. However, PFPE lubricant depletion and recovery behavior at the timescale of HAMR conditions (microsecond to millisecond) is known to be that of a viscoelastic fluid. In the later part of the dissertation, we introduce a modification to the traditional lubrication equation that takes into account the effect of a non-zero Maxwell relaxation time and accommodates the viscoelastic effects. The results suggest that this method is numerically unstable for the small laser spot sizes close to the target of HAMR. Accordingly, we developed a novel approach to model the viscoelastic depletion and recovery behavior of PFPE ultra-thin films using a Finite Element Analysis. We show that this new method is able to model the entire range of material viscoelasticity, from purely viscous to purely elastic extremes. The results show that the viscoelastic effects become remarkably pronounced with a decrease in the laser spot size. For the micron-size laser spots, close to typical experimental conditions, the lubricant behaves like a viscous fluid. However, for the laser spot size of 20nm, close to the industry target for HAMR, it behaves like an elastic solid. In exposing the consequences of this viscoelastic behavior, this study predicts that lubricant flow due to thermo-capillary effects will not be a significant issue in the development of the HAMR technology. Rather, future efforts should concentrate on the thermal degradation and evaporation aspects of the HDD lubricants.

To the kind father
a brilliant sun to the world, way out in the horizon, out of the
reach of the hands and the eyes.
the luminous full moon, shining like a bright lamp and a
dazzling light, a guiding star in the dark gloom, the arid deserts
and the crashing seas.
the quenching water for the thirsty, and a guide to lead away
from destruction.
the guiding fire on the desert highlands, whose heat will warm
the seekers of his warmth.

Contents

List of Figures

List of Tables

Nomenclature

List of Abbreviations

CML   Computer Mechanics Lab

FEA   Finite Element Analysis

FVM   Finite Volume Method

FWHM   Full-Width Half-Maximum

HAMR   Heat-Assisted Magnetic Recording

HDD   Hard Disk Drive

HDI   Head-Disk Interface

NFT   Near-Field Transducer

OSA   Optical Surface Analyzer

PFPE   perfluoropolyether

TFC   Thermal Flying Height Control

List of symbols

(τ_x, τ_y) shear stress within the lubricant

$(\tau_{x,ext}, \tau_{y,ext})$ thermo-capillary shear stress on the lubricant surface

(q_x, q_y) mass fluxes in the planar x and y direction

$\boldsymbol{\sigma}$ stress tensor

$\boldsymbol{e}$ deviatoric strain tensor

$\boldsymbol{n}$ lubricant surface normal vector

$\Delta E_{vap}^*, \Delta S_{vap}^*$ activation evaporation energy and entropy

$\Delta E_{vis}^*, \Delta S_{vis}^*$ activation flow energy and entropy

ΔT difference between HAMR peak and room temperatures

$\dot{m}$ evaporative mass flux, $[kg/(m^2 \Delta s)]$

η local viscosity

γ surface tension

γ_s^d, γ_s^p dispersive and polar components of surface energy

λ_i Maxwell relaxation time

Π, Π' disjoining pressure and its derivative $(= d\Pi/dh)$

Π_d, Π_p dispersive and polar components of disjoining pressure

A Hamaker constant

c the slope of the surface tension-temperature curve $(= d\gamma/dT)$

D diffusion coefficient

De Deborah number

$G(t)$ viscoelastic shear modulus

G_i shear rigidity

h local lubricant thickness

h_0 initial lubricant film thickness

L laser spot size, length scale in x,y direction, FWHM

M_w molecular weight

p pressure within the lubricant

P_{vap}^* lubricant vapor pressure

t time

T_0 glass temperature

T_∞	room temperature
t_r	recovery time
t_s	timescale
U	Disk speed
u, v, w	continuum velocity components
x, y, z	space coordinates

Chapter 1

Introduction

Hard Disk Drives (HDDs) are one of the key parts of the data storage industry. The worldwide need for data storage is growing everyday. Many tech industries such as digital banking, and cloud services store multiple copies of their assets, and this data redundancy pushes the need for data storage even further. HDDs have been and are a significant part of the consumer electronics, enterprise internet sector, and the Content Distribution Networks (CDN). This exploding need for data storage must be satisfied and HDDs are still the most cost effective answer to this need. Accordingly, the HDD industry is pushing the limits to increase the data density and reliability of the devices in order to provide cheaper and better solutions for the market demand.

The following sections give an overview of the development of the HDD technology and introduce the future technologies that are expected to help reach higher data densities. In particular, the concept of Heat-Assisted Magnetic Recording (HAMR) is introduced as a new promising HDD technology, and finally, the objectives and the organization of the dissertation as well as its contributions to the development for HAMR are outlined.

1.1   Hard Disk Drive History

The IBM 305 RAMAC was the first HDD introduced in 1956 to serve the U.S. Navy and private corporations. It had a 5MB capacity and needed a room with an area of about $500 ft^2$, designed to meet the need of real-time accounting in business. The later version in 1957 was the IBM 350, leased to the businesses at a cost of $3,200 per month, equivalent to around $27,000 today [1]. Over 50 years of technological advancements, the HDD's cost and data density improved dramatically, so that at present, a Seagate 10TB Enterprise Helium Drive with physical dimensions as small as 147x100x26mm costs less than $500. Over the course of time, more than 200 companies have contributed to the development of the HDDs, which are consolidated into three major companies today, namely Western Digital, Seagate, and Toshiba, shipping more 400 million HDD units per year.

The data storage market can be divided into four major market segments: Desktop Computers, Enterprise Servers, Mobile Devices, and Consumer Electronics. With the advent of the Solid State Drives (SSDs), the two latter market segments have changed their emphasis on HDDs. For example, by the 3rd quarter of 2016, Apple launched the entire series of its
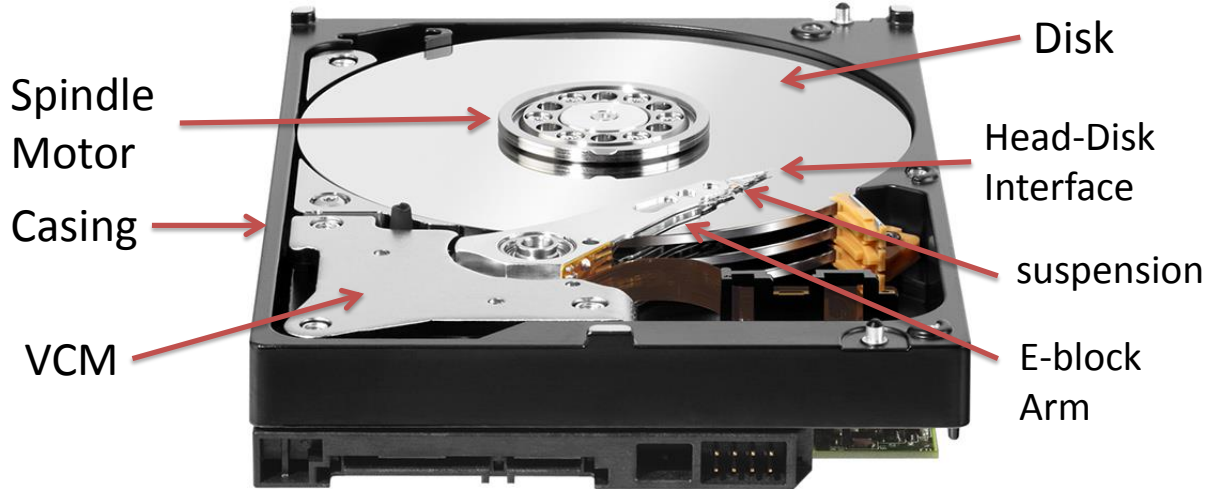
Figure 1.1: Different components of a modern HDD

Laptop and hand-held devices with SSDs only. However, a major portion of the Enterprise, and a good portion of the Desktop market segments such as Apple iMac and Lenovo M and Y series still rely on HDD technology for their mass storage.

Studies show that the start-up [2], random access[3], and latency times [4] as well as the power consumption are much lower for SSDs compared to HDDs. Also, SSDs have better data transfer rates, reading performance [5], and resistance against acoustic, temperature, and corrosion. These are the among the reasons for the HDD sales decline in the mobile and consumer electronics market segments.

On the other hand and in contrast to SSDs, HDDs can overwrite data directly on the drive in an arbitrary sector. Additionally, when the data is stored offline (unpowered in shelf) in long term, the magnetic medium of HDD retains data significantly longer than the flash memory used in SSDs. Also, the risk of a sudden, catastrophic data loss is lower for HDDs compared to SSDs [6]. Finally and most importantly, SSDs are much more expensive compared to the HDDs with a significant price margin. The typical values for the SSDs are around \$300/TB compared to \$50/TB for HDDs. The Total Cost of Ownership (TCO) is a significant incentive for the Enterprise market which keeps the HDDs still the best solution for the Data Centers and business applications. The development of the new technologies such as Bit-Patterned Media (BPM) and Heat-Assisted Magnetic Recording (HAMR) are expected to enable the HDD industry not only to improve the cost efficiency of the products even further, but also to respond to the accelerating worldwide need for the data storage.
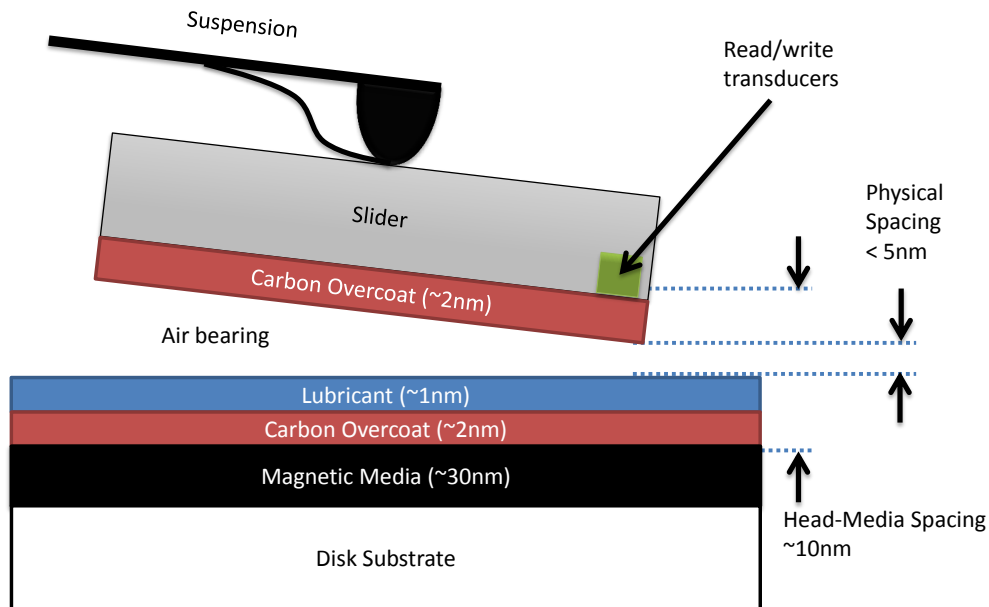
Figure 1.2: A schematic view of a typical Head-Disk Interface (HDI) including the key parts of the disk and slider

1.2 Head-Disk Interface (HDI)

A Hard Disk Drive mainly consists of a set of rotating disks (a.k.a. Platters) which store the data in terms of the magnetic bits, and a head assembly which reads and writes the data from and to the disk (Fig. 1.1). The disk is divided to radial segments known as the Tracks, and each track is divided into multiple sectors where the magnetic bits are stored.

A spindle motor, fixed to the HDD casing, maintains an accurate rotational speed for the disk, varying between 4200RPM for energy-efficient portable drives and 15000RPM for high-performance server drives. Similarly, a Voice-Coil Motor (VCM) controls the arm angle and helps the head assembly to have access to different radial positions and different tracks on the disk. The head assembly (Fig. 1.1) is attached to the VCM by the E-block Arm and includes a suspension part and a slider that contains the read/write elements, as illustrated in Fig. 1.2.

Fig. 1.2 shows the head assembly where the disk and the head have active mechanical and magnetic interactions, also known as the Head-Disk Interface (HDI). In order to prevent the wear and friction effects, the mechanical contact between the head and the disk is avoided. Rather, an air-bearing pressure due to the disk speed maintains the clearance between the disk and the slider. The relative motion between the disk and slider pressurizes the air bearing region between them, and the resulting force and moment caused by the air bearing pressure are balanced by the suspension load which pushes the slider towards the disk (downward in Fig. 1.2). The slider is therefore flying over the disk, and its dynamic stability is guaranteed by the process stated above.

The read/write elements are magnetic transducers located at the slider trailing edge, and the physical spacing between these elements and the disk surface is known as the flying height (FH). The strength of the read/write output signals has an inverse exponential relation with the disk-slider spacing such that the readback signal for a $1\mu m$ flying height is less than 1% of the amplitude that would be obtained when the slider and the disk are in contact [7]. Accordingly, the main two tribological challenges faced by the industry are not only to minimize the flying height, but also to maintain the stability of the slider's flying attitude (head-disk spacing, pitch, and roll) within 10% of the design point. In modern HDDs a new technology known as the Thermal Flying-Height Control (TFC) allows the HDD to actively control the flying height which dramatically improves the performance of the slider and the read/write transducers. In the TFC technology, a resistive heater is integrated into the slider's trailing edge near the read/write transducers. When a voltage is supplied, the heater generates a heating power raising the local temperature which leads to a mechanical protrusion in the slider's trailing edge. This protrusion is proportional to the supplied heating power and controls the physical spacing between the read/write transducers and the disk.

The Disk has different layers, as illustrated in Fig. 1.2. The main part of the disk is the magnetic layer made of a cobalt-based alloy with a thickness of around 30nm which is deposited on an aluminum or glass substrate disk. The magnetic medium layer is where the magnetic bits are stored in terms of the magnetic field polarization directions. In earlier HDDs, longitudal recording was employed where the magnetic field direction was in the disk plane, along the track. However, the data density in this design is significantly limited due to the superparamagnetic effects. In order to overcome such limitations, perpendicular recording was introduced where the magnetic field direction is normal to the disk plane. Toshiba was the first to ship the perpendicular recording HDDs in 2005, a technology that is widely used by the HDD industry nowadays [8].

The magnetic medium layer is a relatively soft material and is protected by a hard Diamond-Like Carbon (DLC) overcoat with a typical thickness of 2-3nm and covered with a thin polymer lubricant layer with a thickness of 1-2nm. This thin layer of lubricant is a Perfluoropolyether (PFPE) polymer in the modern generation of HDDs. PFPE lubricants are clear colorless fluorinated synthetic oil materials and are perfect for the HDD applications because they are nonflammable in chemical and oxygen service, long lasting, and show nice adhesion properties when covering the disk DLC overcoat [9].

As discussed earlier, the read/write performance of the HDD is highly sensitive to the mechanical stability of the slider flying over the disk. The slider surface facing the disk is called the Air Bearing Surface (ABS). This surface has a special etched design in order to control the airflow in the air-bearing region to stabilize the slider's flying attitude and to minimize the flying height which eventually helps increase the HDD data density. Additionally, different recently developed technologies like TFC and promising technologies such as Bit Patterned Media (BPM) and Heat-Assisted Magnetic Recording (HAMR) are expected to make a great contribution in increasing the data density.

1.3 Heat Assisted Magnetic Recording(HAMR): Concept and Challenges

The data density in HDDs has been constantly growing, and it is now approaching a $1TB/in^2$ limit due to the superparamagnetic effect. This effect becomes significant when the size of the magnetic regions on the disk become so small that the molecular thermal fluctuations overcome the magnetic orientation of that region, which corrupts the data stored there in terms of the magnetic orientations i.e. up and down in the case of perpendicular recording. In order to solve this problem, materials with higher coercivity are employed as the proper choice for the magnetic media. Coercivity is the material reluctance against the change in the magnetic orientation, and a good example used by the HDD industry is the high anisotropy granular FePt media. By choosing such materials for the magnetic media, the magnetic orientation and data stored on each bit is preserved at room temperature, and the data density of the disk can be further increased beyond the conventional material limits. At the Intermag 2015 Conference in Beijing, China, Seagate reported a successful HAMR recording on FePt media at an areal density of $1.402Tb/in^2$ [10].

However, this technology has its own challenges. Materials with higher coercivity, need a huge magnetic field to change the magnetic orientation of the bit and write on the disk. This magnetic field is often too large for the conventional write transducers to provide. The material coercivity, on the other hand, has an inverse relationship with temperature. In particular, the coercivity drops to zero as the temperature reaches the Curie temperature in which the material loses its permanent magnetic properties. The Curie temperature is around 700K or 430^oC for FePt which is the main candidate for the HAMR magnetic media.

In the proposed HAMR technology, a laser heats the disk up to the Curie temperature and a transducer with a small magnetic field writes the data on the point of interest. Then, the magnetic media cools down to the room temperature and the data stored on the disk freezes on the disk. In order to achieve a data density of around 4 to $5TB/in^2$, the HDD industry has targeted a thermal spot with a Full Width Half Maximum of less than 25nm and a peak temperature of around 500^oC [11].

This technology is promising but it has serious challenges that have to be addressed. First, the media, the protective Carbon overcoat, and the lubricant are exposed to high temperatures and rapid laser irradiations and cooling of the order of a few nanoseconds. The materials need to be heated up to the Curie temperature and quickly be restored to room temperature. This imposes numerous problems for the materials, including but not limited to, thermal fatigue, degradation and evaporation.

Second, The 25nm thermal spot size target for HAMR requires the laser beam to have a same beam size of around 25nm which is far below the diffraction limit for the laser beam, and therefore, a special aperture or antenna, also known as the Near-Field Transducer (NFT), must be employed to maintain the laser focus at this beam size. The NFT has faced many challenges, and it is identified as one the key obstacles to developing the HAMR technology. The output beam size from the NFT is much smaller than the wavelength of the laser used, which causes the current NFT designs to be highly inefficient with a significant energy loss. Additionally, the distance between the NFT and the media is less than 2nm in the current HDD designs, and due to this proximity, a thermal back heating is possible from

the high temperature disk to the NFT. These effects together increase the NFT temperature significantly, while the NFT is known to be highly vulnerable against the high temperature conditions since it is made of a thin film of metal (usually gold). These effects together decrease the reliability of the NFT significantly.

In addition to the temperature considerations stated above, the proposed HAMR technology with a data density of $4TB/in^2$ requires the physical spacing between the write transducers and the magnetic medium (known as the head-media spacing) to be decreased even further from about 10nm (for the current HDD designs) to 4.5nm for HAMR. Fig. 1.2 shows that the head-media spacing consists of the thickness of the Carbon overcoat layers on the slider and the disk, the lubricant thickness, and the air bearing clearance. Accordingly, the thickness of the carbon overcoat layers on the slider and the disk should be decreased to less than 1.5nm for the target design for HAMR. In addition, the physical spacing (minimum Fly Height) as well as the thickness of the lubricant covering the disk need to decrease to less than 1nm. Decreasing the thickness of each of these layers is highly challenging and must be addressed through the proper material and ABS design for the $4TB/in^2$ target of HAMR.

1.4 Objective and Organization of this Dissertation

In traditional HDDs the assumption of modeling the HDD components under isothermal conditions is reasonable since no significant source of heating existed. However in Heat-Assisted Magnetic Recording (HAMR) technology, a laser exposes the magnetic media to a high temperature in order to reduce the magnetic material's coercivity during the writing process. As such, two areas of highest concern for HAMR technology research and development are material performance and reliability. More specifically, research needs to address hard disk drive (HDD) lubricant depletion and recovery under HAMR conditions.

This dissertation focuses on the effect of the HAMR conditions on the behavior of the PFPE lubricants covering the disk, and it strives to improve the current numerical models. This is accomplished by applying lubrication theory and the theory of viscoelasticity to the lubricants, including the effects of polymer viscoelasticity, thermo-capillary shear stress, thin-film disjoining pressure, viscosity, and evaporation.

The objective of this dissertation is to study the performance of the disk lubricants under HAMR conditions by

- developing a lubricant model based on lubrication theory for Newtonian viscous fluids

- performing numerical simulations for the depletion and recovery behaviors of various PFPE lubricants

- developing a viscoelastic model for the polymeric lubricants, based on the nonlinear models for viscoelastic Maxwell fluids

- developing a Finite Element Analysis for lubricants as linear viscoelastic Maxwell fluids

- Investigating the effect of viscoelasticity on lubricant behavior by performing numerical simulations using the developed models.

In the following chapters each item is discussed in detail. Chapter 2 outlines the lubricant model under HAMR conditions. Chapter 3 explains the lubrication theory for HDD lubricants under HAMR conditions. Chapter 4 introduces the material properties used for different lubricants of this study, based on the experimental measurements. Chapters 5 and 6 present the results of the numerical analysis based on lubrication theory for lubricant depletion and recovery under HAMR conditions. Chapter 7 introduces the viscoelastic properties of HDD lubricants. Chapter 8 introduces the theory of viscoelasticity for Maxwell fluids and discusses the key viscoelastic parameters related to the HDD lubricants. Chapter 9 presents the analytic development and results of the numerical analysis for viscoelastic lubricants based on the nonlinear viscoelastic constitutive equations. Chapter 10 introduces the Finite Element Analysis and the corresponding results for viscoelastic HDD lubricants, based on the linear constitutive equations for Maxwell fluids. Finally, Chapter 11 presents a summary and concludes this dissertation.

Chapter 2

Problem Definition

In the proposed future hard disk drive (HDD) magnetic recording technology known as Heat Assisted Magnetic Recording (HAMR), there are several head-disk interface issues to be addressed and solved. One key issue among those regards the behavior of the polymer lubricant that coats the HAMR recording media. The lubricant, mostly from the perfluoropolyether (PFPE) family of lubricants, is ideally supposed to cover the HAMR media uniformly. However, several events can occur in which the lubricant layer deforms, or depletes, and subsequently, it loses the ideal uniform profile. This can decrease the stability of the slider's flying attitude over the disk, which may impair the performance and reliability of the Head Disk Interface (HDI). Therefore, several studies have aimed to improve the performance of the lubricants via optimization of the molecular structure of the basic lube designs such as Fomblin Z. Such studies introduced new molecular structures such as the Z-dol and Z-tetraol families, which include hydroxyl polar end-groups. The molecular structure of these conventional lubricants is:

$$X - [(OCF_2)_m - (OCF_2CF_2)_n - (OCF_2CF_2CF_2)_p - (OCF_2CF_2CF_2CF_2)_q]_{x_0} - OX$$

where the non-polar Fomlin Z has the non-reactive end-groups of $X = -CF_3$, Z-dol has two hydroxyl end-groups with $X = -CF_2CH_2 - OH$ and Z-tetraol has 4 hydroxyl end groups with $X = CF_2CH_2 - O - CH_2CH(-OH)CH_2 - OH$ [12]. These hydroxyl end-groups help the molecule establish stronger bonds with the substrate, improving the viscosity, disjoining pressure, and evaporation properties of the lubricant. Recent studies have improved the behavior of these lubricants by merging two Z-dol or Z-tetraol molecules to create Multi-Dentate lubricants such as ZDMD and ZTMD, which also include hydroxyl groups in the middle of the molecule chain (Fig. 2.1) [13]. The design of these lubricants gives them the special ability to bond to the Diamond Like Carbon (DLC) substrate, reducing the free chain length and improving the lubricant properties. The molecular weight for each of these lubricants can be modified through changing the degree of polymerization, i.e. parameters m, n, p, x_0 in the formulation above.

Among simulation analyses performed on HDD lubricant behavior, two groups of modeling methods stand out. In some studies, the Molecular Dynamics model is favored over a continuum model since the typical value for lubricant film thickness is of the order of $h_0 = 1nm$, close to the characteristic size of the lube molecules. In other studies such as
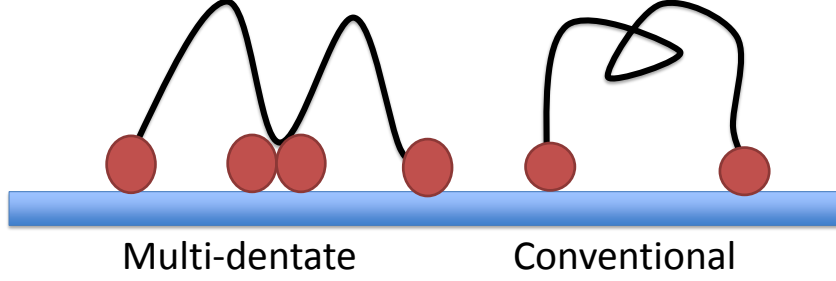
Figure 2.1: Molecular structure of a typical multi-dentate lubricant like ZTMD versus the molecular structure of a conventional End-Group Functional lubricant like Z-dol and Z-tetraol. The red beads represent the active hydroxyl (-OH) group that has a polar interaction with DLC layer [13]

Refs. [14, 15, 16, 17], the continuum models are favored because they provide a more cost effective means of analysis when factoring in the other length scales of the problem such as the HAMR laser spot size, around $20nm$, and the slider's characteristic size, around $800\mu m$. Specially, the separation of the length scales in the ultra-thin film problem implies the use of lubrication theory for a Newtonian fluid as a first order approximation, even though the PFPE lubricants' behaviors are viscoelastic and nonlinear [12]. Many researchers found that the mentioned method can describe the behavior of the PFPEs very well; specifically, Refs. [18, 19] report that the continuum model can agree well with experiments, and the much more expensive Molecular Dynamics simulations to describe the lubricant behavior. Therefore, the lubricant in this study is modeled using a continuum theory. The first part of this dissertation uses lubrication theory for a viscous fluid model, and the later part models the lubricant as a viscoelastic Maxwell fluid.

The lubricant is assumed to be bonded to the substrate (no slip condition), and have a free surface with an unknown local thickness of $h(x, y; t)$, a pressure $p(x, y; t)$ constant across the film, and a shear stress $\tau_{ext}(x, y; t)$. The pressure field is a function of thickness h as well as x, y, and t (Fig. 2.2).

Figure 2.2 shows a schematic view of the laser irradiated on the disk, moving with a speed of U down the track. Due to this laser exposure, a high temperature field is observed in the lubricant which can be described with a Gaussian distribution of the form:

$$T(x, y; t) = T_\infty + \Delta T \exp \left[-\frac{(x - x_0 - Ut)^2 + y^2}{2L^2\sigma^2} \right] \tag{2.1}$$

where $T(x, y; t)$ is the lubricant local temperature, T_∞ is the room temperature, $\Delta T = T_p - T_\infty$ is the difference between the HAMR peak and room temperatures, L is the Full-Width Half-Maximum (FWHM) of the temperature distribution, close to the laser beam diameter, $\sigma = (2\sqrt{2\ln 2})^{-1}$ is a dimension-less constant relating the FWHM to the Gaussian distribution, U is the laser speed, around 5-10m/s for a typical HDD, and $x_0 + Ut$ is the position of the laser spot at time t along the track (x-direction). This moving localized high temperature has different effects on the lubricant, including polymer thermal degradation, evaporation, and thermo-capillary effects. In the next chapters, we discuss the relation-
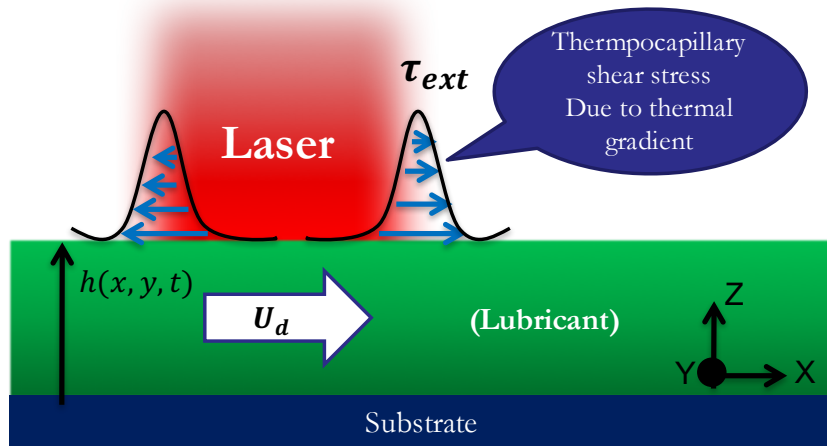
Figure 2.2: A schematic illustration of the lubricant under HAMR conditions.

ship between evaporation, lubricant thickness and local temperature. The effect of thermal degradation on the lubricant depletion is not studied in this work, however, one can add it as an extra term similar to that for evaporation. The thermo-capillary effects are due to the relation between the surface tension and temperature, so that the thermo-capillary (Maragoni) shear stress on the lubricant surface is proportional to the temperature gradient $\boldsymbol{\nabla} T$, driving the lubricant from high temperature/low surface tension to low temperature/high surface tension regions.

In Chapter 4, we will discuss how the pressure depends on the local thickness $p(h)$. Also for the thin film case, an effective viscosity is assumed that takes into account the effects of temperature and lubricant thickness.

Chapter 3

Lubrication Theory for HAMR lubricants

Lubrication theory is a branch of Fluid Mechanics that describes the dynamics of the lubricants, including gasses and liquids, for geometries where one of the structural dimensions is significantly smaller than the other ones. In the case of HDD lubricants, the characteristic (initial) film thickness h_0 is much smaller than the characteristic length in the directions parallel to the disk L: $h_0 \ll L$. Lubrication theory can be used for either internal flows or free film lubrication cases.

Internal flow lubrication theory is employed when the lubricant fills the media between two fixed boundaries. It is a powerful and cost-effective tool for designing fluid bearings and has many applications in various industries such as automotive, power plant, and so on. In the HDD industry, the internal flow lubrication is used to analyze the lubricant dynamics of the spindle motor bearing as well as the dynamics of the air-bearing between the slider and the disk. In this theory, the geometry and the boundary conditions of the fluid are known and the lubrication theory solves for the pressure distribution within the fluid.

Free film lubrication theory is employed when the thin fluid films are bounded to a known surface on one side and have a free surface on the other side. In this case, the position of the free surface is unknown, and the free film lubrication theory can solve for the local film thickness. Coating is one of the major applications of this theory including but not limited to painting, thin-films, printing, and adhesives. The polymer lubricants covering the HDD platters, which are the concern of this dissertation, are one of the best examples of free film lubrication. The ultra-thin film of PFPE lubricants covering the disk have a typical thickness of 1nm which is substantially smaller than the other characteristic dimensions along the disk surface. In the case of free film lubrication, many factors such as thin-film viscosity, surface tension, wetting, and dewetting become important. For the ultra-thin films (thinner than a few micrometers) of this study, intermolecular effects such as Van der Waals and disjoining forces become significant as well. Chapter 4 will introduce these parameters for the HDD lubricants in more detail.

Lubrication theory is based on the assumption that the lubricant behaves like a viscous fluid and obeys the Navier-Stokes equations. In addition, the following assumptions are made for the case of HAMR lubricants:

- Negligible body forces.

- Negligible inertia forces.

- Considerably small thickness compared to in-plane length scales ($h0 \ll L$)

- Constant fluid density.

- Laminar flow.

- No slip at boundaries.

- Rigid and smooth solid surfaces.

In lubrication theory fluids are often considered as Newtonian viscous. However, upon using the proper numerical scheme, one can also add the shear thinning and shear thickening effects by modifying the effective viscosity to be a function of the shear-rate at each timestep. In addition, the viscosity is often considered to be constant across the film. In the case of HDD lubricants, experimental results show a sharp change in the lubricant viscosity and mobility across the film due to the dual-layer behavior of the polymer lubricants. In this work, we use an effective viscosity model for the lubricant which can be considered constant across the film but can be a function of film thickness and temperature. This model is further discussed in the following chapters. In the following sections we discuss the lubrication theory by introducing the mass conservation law and Navier-Stokes equations, and deriving the lubrication equation.

3.1   Mass Conservation Law

The derivation of the Lubrication equation starts from the Continuity equation which has the following form for a general fluid:

$$\frac{\partial \rho}{\partial t} + \frac{\partial (\rho u)}{\partial x} + \frac{\partial (\rho v)}{\partial y} + \frac{\partial (\rho w)}{\partial z} = 0, \tag{3.1}$$

where u, v, and w are the velocity components in x, y, and z directions, and ρ is the local density, assumed to be constant for the PFPE lubricants since they behave dominantly as incompressible.

As discussed earlier, the lubricant is modeled as a thin-film bonded to the disk substrate. Fig. 3.1 shows the boundary conditions where the lubricant is bonded to the disk at $z = 0$, and at $z = h$ it has a free surface. External fields such as shear stress $\tau_{x,ext}, \tau_{y,ext}$ and pressure p_{ext} can be exerted on the free surface, balanced by the shear stress τ_x, τ_y and the pressure fields within the fluid. Accordingly, the following boundary conditions are applied to the lubricant:
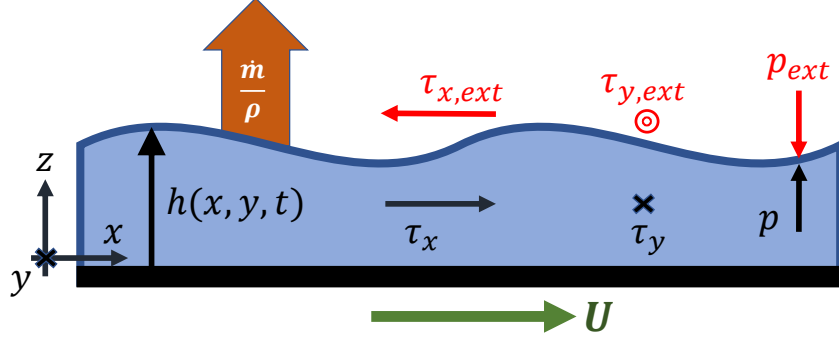
Figure 3.1: HAMR lubricant write process schematic: Lubricant flow is driven by the resulting external thermo-capillary shear stresses $(\tau_{x,ext}, \tau_{y,ext})$ and the pressure gradient$(\nabla p)_{ext}$. Some lubricant is also removed from the film via mass evaporation $\dot{m}$. The thin lubricant film of unknown thickness $h(x,y;t)$ is subjected to a scanning laser spot of speed U, which is represented by a prescribed Gaussian temperature distribution $T(x,y;t)$, as shown in Fig. 2.2.

$$\text{at } z = 0 : u = U, v = 0, w = 0 \quad \text{no slip,} \tag{3.2}$$

$$\text{at } z = h(x,y,t) : \eta\frac{\partial u}{\partial z} = \tau_{x,ext}, \frac{\partial v}{\partial z} = \tau_{y,ext}, \quad \text{stress balance,} \tag{3.3}$$

$$w = \frac{dh}{dt} = \frac{\partial h}{\partial t} + u|_{z=h}\frac{\partial h}{\partial x} + v|_{z=h}\frac{\partial h}{\partial y} \quad \text{kinematic condition,} \tag{3.4}$$

where U is the disk velocity, and $h(x,y,t)$ is the local lubricant thickness. Eq. 3.1 can be simplified for our incompressible case and be integrated across the lubricant in the Z-direction, with the following apparent result:

$$\int_0^h \frac{\partial(\rho u)}{\partial x}dz + \int_0^h \frac{\partial(\rho v)}{\partial y}dz + [\rho w]_0^h = 0. \tag{3.5}$$

The first and second terms in the equation above can be further simplified using the Leibnitz's rule of integration into:

$$\int_0^h \frac{\partial(\rho u)}{\partial x}dz = \frac{\partial}{\partial x}\left[\int_0^h \rho u dz\right] - \rho u|_{z=h}\frac{\partial h}{\partial x}, \tag{3.6}$$

$$\int_0^h \frac{\partial(\rho v)}{\partial y}dz = \frac{\partial}{\partial y}\left[\int_0^h \rho v dz\right] - \rho v|_{z=h}\frac{\partial h}{\partial y}. \tag{3.7}$$

The third term in Eq. 3.5 can be computed from the boundary conditions (Eq. 3.2-3.4) as:

$$[\rho w]_0^h = [\rho w]_{z=h} = \rho\frac{\partial h}{\partial t} + \rho u|_{z=h}\frac{\partial h}{\partial x} + \rho v|_{z=h}\frac{\partial h}{\partial y}. \tag{3.8}$$

Combining these three terms with Eq. 3.5, and simplifying the result we find:

$$\rho\frac{\partial h}{\partial t} + \frac{\partial}{\partial x}\left[\int_0^h \rho u dz\right] + \frac{\partial}{\partial y}\left[\int_0^h \rho v dz\right] = 0. \tag{3.9}$$

This is the integral form of the mass conservation law for the thin film of incompressible lubricant, which can be obtained using a control volume across the lubricant as well. The equation above can be re-arranged in terms of the mass flow rates q_x and q_y as:

$$\rho\frac{\partial h}{\partial t} + \frac{\partial q_x}{\partial x} + \frac{\partial q_y}{\partial y} = 0, \tag{3.10}$$

where q_x and q_y are the mass fluxes in the planar X and Y directions integrated across the film and have the following forms:

$$q_x = \int_0^h \rho u dz, \tag{3.11}$$

$$q_y = \int_0^h \rho v dz. \tag{3.12}$$

The Eq. 3.10 holds for the thin-film of lubricant regardless of the constitutive equation used to describe the material behavior. In this chapter, we will derive the lubrication equation for a purely viscous Newtonian fluid. However, the PFPE lubricants of this study are known to behave viscoelastically, as discussed in chapters 8-10. The integral form of the mass conservation law (eq. 3.10) holds for both of these cases and will be used for the viscoelastic lubricants as well.

3.2 Lubrication equation for Newtonian viscous fluids

The Navier-Stokes equations describe the behavior of a purely viscous fluid. The vector notation of these equations for an incompressible fluid has the following form:

$$-\boldsymbol{\nabla}p + \eta\nabla^2\boldsymbol{v} + \rho\boldsymbol{b} = \rho\dot{\boldsymbol{v}}, \tag{3.13}$$

where p is the pressure within the fluid, $\boldsymbol{v}$ is the velocity vector, η is the viscosity, ρ is the density, $\boldsymbol{b}$ is the body force vector and $\dot{\boldsymbol{v}}$ is the acceleration term. This equation is nonlinear in $\boldsymbol{v}$ due to the acceleration term since it can be expanded to $\dot{\boldsymbol{v}} = \partial\boldsymbol{v}/\partial t + (\partial\boldsymbol{v}/\partial\boldsymbol{x})\boldsymbol{v}$. However, for the case of lubrication flow, based on the lubrication assumptions discussed earlier, the lubricant's inertia and body forces can be neglected. Accordingly, the equation

above is simplified to the following form:

$$\frac{\partial p}{\partial x} = \frac{\partial}{\partial z}\left(\eta \frac{\partial u}{\partial z}\right), \tag{3.14}$$

$$\frac{\partial p}{\partial y} = \frac{\partial}{\partial z}\left(\eta \frac{\partial v}{\partial z}\right), \tag{3.15}$$

$$\frac{\partial p}{\partial z} = 0. \tag{3.16}$$

Equations 3.14-3.15 are accurate to order $(h_0/L)^2$ and Eq. 3.16 to order h_0/L [20]. One should note that we did not assume a constant pressure across the film, rather it is a natural result of the lubrication assumptions. As discussed earlier, viscosity varies in the x-y plane as a function of the local temperature and film thickness $\eta = \eta(T, h)$, with η assumed to be constant across the film. Integrating Equations 3.14 and 3.15 in the Z-direction, and considering the boundary conditions in Equations 3.2-3.3, we find the velocity components in the X and Y directions:

$$u = \frac{1}{\eta}\frac{\partial p}{\partial x}\left(\frac{1}{2}z^2 - hz\right) + \frac{\tau_{x,ext}}{\eta}z + U, \tag{3.17}$$

$$v = \frac{1}{\eta}\frac{\partial p}{\partial y}\left(\frac{1}{2}z^2 - hz\right) + \frac{\tau_{y,ext}}{\eta}z, \tag{3.18}$$

where $0 < z < h$, and $(\tau_{x,ext}, \tau_{y,ext})$ are the components of the thermo-capillary shear stress. These velocity profiles can be combined with the mass conservation law (Eq. 3.10). In addition, a source term of the form $\dot{m}/\rho$ is added to the mass conservation law to take into account the effect of evaporation. Performing these steps, we find the governing evolution equation for the lubricant film to be

$$\frac{\partial h}{\partial t} + U\frac{\partial h}{\partial x} + \frac{\partial}{\partial x}\left[\frac{h^2}{2\eta}\tau_{x,ext} - \frac{h^3}{3\eta}\frac{\partial p}{\partial x}\right] + \frac{\partial}{\partial y}\left[\frac{h^2}{2\eta}\tau_{y,ext} - \frac{h^3}{3\eta}\frac{\partial p}{\partial y}\right] + \frac{\dot{m}}{\rho} = 0, \tag{3.19}$$

where $\dot{m}$ has the unit of $kg/s/m^2$. The evaporation properties of the lubricants will be discussed in Chapter 4. The terms $(\tau_{x,ext}, \tau_{y,ext})$ are the X and Y components of the thermo-capillary shear stress, which for HAMR are proportional to the temperature gradient ∇T and will be determined by the HAMR conditions imposed on the lubricant. The equation above will be used to describe the evolution of the lubricant profile in time in the presence of the laser exposure, where the local lubricant thickness $h(x, y, t)$ is the unknown to be determined subjected to the boundary conditions for h. The term p is the pressure term which is related to the local lubricant thickness through the Inter-molecular forces, as will be discussed in Chapter 4. The developed Finite Volume Method (FVM) solves for the equation above to simulate the behavior of the HAMR lubricants under laser irradiation, the results of which can be found in Chapter 5.

After the laser irradiation to the disk stops, the lubricant cools down to the uniform room temperature, and the effects of thermo-capillary shear stress and evaporation vanish and the lubricant has a non-uniform profile. In this case, the following equation describes how the

17

disturbed lubricant flows back to the uniform profile:

$$\frac{\partial h}{\partial t} + \frac{\partial}{\partial x}\left[-\frac{h^3}{3\eta}\frac{\partial p}{\partial x}\right] + \frac{\partial}{\partial y}\left[-\frac{h^3}{3\eta}\frac{\partial p}{\partial y}\right] = 0. \tag{3.20}$$

The equation above suggests that the timescale of the recovery is determined by a balance between the disjoining pressure gradient ∇p, as a driving force for reflow, and viscosity η. A more detailed discussion about the reflow timescale can be found in Section 6.2.

Several previous papers have used Eq. 3.20, and it is well known in the field [17, 21]. Some other studies [22, 23, 24, 25] use another variation of the equation that is a nonlinear diffusion equation with a diffusion coefficient $D(h)$ as a function of the lubricant thickness h. This variation of the equation is

$$\frac{\partial h}{\partial t} + \frac{\partial}{\partial x}\left[D(h)\frac{\partial h}{\partial x}\right] + \frac{\partial}{\partial y}\left[D(h)\frac{\partial h}{\partial y}\right] = 0. \tag{3.21}$$

For the case of HAMR reflow, an explicit relation can be found between the diffusion coefficient $D(h)$ in Eq. 3.21 and the disjoining pressure $\Pi(h)$ and viscosity $\eta(h)$ in Eq. 3.20 [26], as discussed in Section 6.2. Chapter 6 presents the simulation results for HAMR reflow based on the governing equation 3.20.

Chapter 4

Perfluoropolyether Lubricant Properties

In Chapter 2, we briefly introduced the Perfluoropolyether (PFPE) lubricants. A more detailed introduction of these lubricants along with other HDD lubricants can be found in [12]. Three families of PFPE lubricants including Z-dol, Z-tetraol, and ZTMD are widely used in the HDD industry. Accordingly, this chapter gives an overview of these lubricants' properties with a significant effect on their behavior under HAMR conditions. These properties, including surface tension, disjoining pressure, effective viscosity, and evaporation, can modify the Eqs. 3.19 and 3.20.

4.1   Surface Tension Effects

In the ultra-thin films of lubricants, the surface tension depends on both the temperature and lubricant thickness. Reference [27] gives an expression for such a dependence for Fomblin Z03. However, the formulation by Ref. [27] shows a small dependence of the surface tension on the lubricant thickness which can be almost neglected. Also, the dependence of surface tension on the lubricant thickness is far more complicated for polar lubricants such as Z-dol, Z-tetraol and ZTMD. In order to avoid such complexities, we only include the dominant effect of the temperature on the surface tension.

   Surface tension has two important effects on the physics of this problem. The first effect is a restoring force normal to the interfacial element of the liquid that is caused by the curvature of the surface element. This normal force is called the Laplace pressure, and it can be described as

$$p_{Laplace}\boldsymbol{n} = -\gamma(\nabla.\boldsymbol{n})\boldsymbol{n} = \gamma(\nabla^2 h)\boldsymbol{n}, \tag{4.1}$$

where $\boldsymbol{n}$ is the unit vector normal to the lubricant-air interface, γ is the local surface tension, and h is the local lubricant thickness. The second effect of surface tension is the Maragoni [28] or thermo-capillary shear stress which appears when a non-uniform distribution of surface tension is present on the liquid-gas interface. In the case of HAMR, this phenomenon occurs because of the Gaussian temperature distribution, since the surface tension highly depends on the temperature. This effect can be formulated in terms of a tangential shear force exerted

on the interfacial element due to the surface tension gradient $\boldsymbol{\nabla}\gamma$ as:

$$\boldsymbol{\tau} = \boldsymbol{\nabla}\gamma - \boldsymbol{n}(\nabla\gamma.\boldsymbol{n}), \tag{4.2}$$

where $\boldsymbol{n}$ is the interface unit normal vector and $\boldsymbol{\nabla}$ is the two dimensional gradient operator $\boldsymbol{\nabla} = \frac{\partial}{\partial y}\boldsymbol{e_x} + \frac{\partial}{\partial y}\boldsymbol{e_y}$, where $\boldsymbol{e_x}$ and $\boldsymbol{e_y}$ are the unit vectors of the tangential coordinates x and y (along the thin-film). For quasi-parallel films, including thin-film lubricants, $|\boldsymbol{\nabla}h| \ll 1$, $\boldsymbol{n} \approx \boldsymbol{e_z}$, where $\boldsymbol{e_z}$ is the unit vector normal to the disk (across the thin-film). Thus $\boldsymbol{\nabla}\gamma.\boldsymbol{n} \approx 0$, therefore, the components of the surface tension force is simplified to

$$p_{Laplace}\boldsymbol{n} = \gamma(\nabla^2 h)\boldsymbol{e_z}, \tag{4.3}$$

$$\boldsymbol{\tau} = \boldsymbol{\nabla}\gamma = \frac{\partial\gamma}{\partial y}\boldsymbol{e_x} + \frac{\partial\gamma}{\partial y}\boldsymbol{e_y}. \tag{4.4}$$

The surface tension of a non-polar PFPE lubricant was measured in the limited temperature range of $10 - 180^o C$ and found to be linear [27]. Reference [15] assumes that the functional PFPE lubricants such as Z-dol have a similar slope, and in their model, they use the slope $\partial\gamma/\partial T = -0.06 mN/(m^o C)$. The same assumption is made here for the Z-tetraol family of lubricants. Under these assumptions, we can rewrite Eq. 4.4 as

$$\boldsymbol{\tau}_{ext} = \boldsymbol{\nabla}\gamma = \frac{d\gamma}{dT}\frac{\partial T}{\partial y}\boldsymbol{e_x} + \frac{d\gamma}{dT}\frac{\partial T}{\partial y}\boldsymbol{e_y}, \tag{4.5}$$

where the spatial derivatives of temperature can be found from the prescribed temperature function $T(x, y)$.

4.2 Surface Energy and Disjoining Pressure

For thin films, the liquid-air and liquid-solid interfaces come so close to each other that the interaction between them cannot be neglected. The inter-molecular forces between the thin-film lubricant and its surrounding can be modeled in terms of disjoining pressure [29]. First introduced by Derjaguin [30], disjoining pressure is defined as an equivalent pressure exerted on the lubricant surface representing the intermolecular forces between lubricant molecules and surrounding lubricant, disk, and gas molecules. Disjoining pressure Π has two components, Π_d the dispersive and Π_p the polar components. The dispersive component is due to the Van der Waals interactions between the molecules and the polar component is due to the polar interaction between the lubricant end-groups and the Diamond-Like Carbon (DLC) substrate [26, 31]. For non-polar lubricants like Fomblin Z, the disjoining pressure is limited only to the dispersive component, while for lubricants with hydroxyl end-groups such as Z-dol, Z-tetraol, and ZTMD, the effect of the polar disjoining pressure can be significant. Disjoining pressure can generally be a function of molecular weight, lubricant thickness, and the production processes such as annealing [32]. The disjoining pressure can be expressed in the form of a point-wise normal force that is exerted on a surface element of the liquid-air interface. Such a force causes a difference between the pressure of the liquid and pressure of

the ambient air as follows (Fig. 3.1)

$$\Pi(h) = p - p_\infty, \tag{4.6}$$

where $\Pi(h)$ is the disjoining pressure as a function of h, p is the liquid pressure, p_∞ is the air pressure out side of the liquid. Many researchers tried to obtain an appropriate expression for the surface energy and disjoining pressure of PFPE lubricants. Reference [33, 34] gives expressions for the surface energies of Z-tetraol 1200 and Z-tetraol 2200. Reference [13] gives an expression for the surface energy of ZTMD for both components of dispersive and polar. Reference [35] gives an accurate expression for the disjoining pressure of the Z-dol 1600. Reference [32] gives expressions for the components of surface energy of Z-dol 2000 (unannealed) under 2A thickness. One can use the surface energy of the lubricant to find the disjoining pressure as a function of lube thickness according to the equation:

$$\Pi(h) = -\frac{\partial \gamma_s}{\partial h} = -\frac{\partial \gamma_s^d}{\partial h} - \frac{\partial \gamma_s^p}{\partial h} = \Pi^d(h) + \Pi^p(h), \tag{4.7}$$

where the γ_s^d and γ_s^p distinguish the dispersive and polar components of the thin-film surface energy γ_s, and the parameters $\Pi^d(h)$ and $\Pi^p(h)$ represent the dispersive and polar components of the disjoining pressure $\Pi(h)$. In order to fit a curve to the experimental data of surface energy, Ref. [33] uses a general form of

$$\gamma_s^d = \frac{A_{eff}}{12\pi} \frac{1}{(d_0 + h)^2} + \gamma_\infty \tag{4.8}$$

for the dispersive component of the surface energy of Z-dol 1600; where γ_∞ is the bulk surface energy, A_{eff} is the effective Hamaker constant, and d_0 is a fitting parameter. A_{eff} and d_0 indicate the strength of interaction between the PFPE main molecular chain and the carbon substrate. Some scholars define the Hamaker constant in the equation above using a prefactor of $1/24\pi$ instead of $1/12\pi$. For convenience, we converted all Hamaker constants in the different references to the standard form of Eq. 4.8 and included these numbers in Table 4.1.

For the polar component of surface energy of Z-dol 1600, Ref. [35] uses a polynomial expansion of degree 7 since it matches the experimental measurements very well

$$\gamma_s^p = \gamma_\infty \sum_{n=0}^{7} a_n \left(\frac{h}{d_1}\right)^n, \tag{4.9}$$

with the curve fitting parameters a_n and d_1 listed in Table 4.1. With the similar approach, we fit the polynomials up to degree 7 to the polar surface energy curves of Z-dol 1600, Z-tetraol 1200, Z-tetraol 2200, and ZTMD and obtain the curve fitting parameters for these lubricants, which are also available in Table 4.1. The surface energy and disjoining pressure of the five different lubricants, Z-dol 1600, Z-dol 2000, Z-tetraol 1200, Z-tetraol 2200, and ZTMD are plotted against the lube thickness in Figures 4.1 and 4.2, respectively.
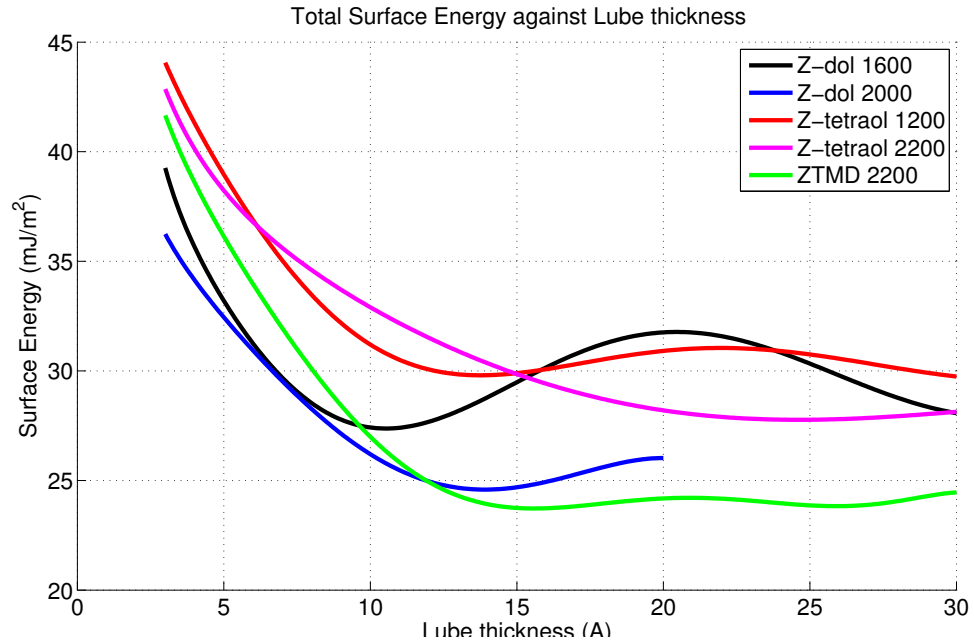
Figure 4.1: Total (sum of dispersive and polar components) surface energy as a function of lubricant thickness for Z-dol 1600, Z-dol 2000, Z-tetraol 1200, Z-tetraol 2200, and ZTMD. Surface Energy Parameters are calculated for both dispersive and polar components of the disjoining pressure for these lubricants according to Refs. [35], [32], [33], and [13]
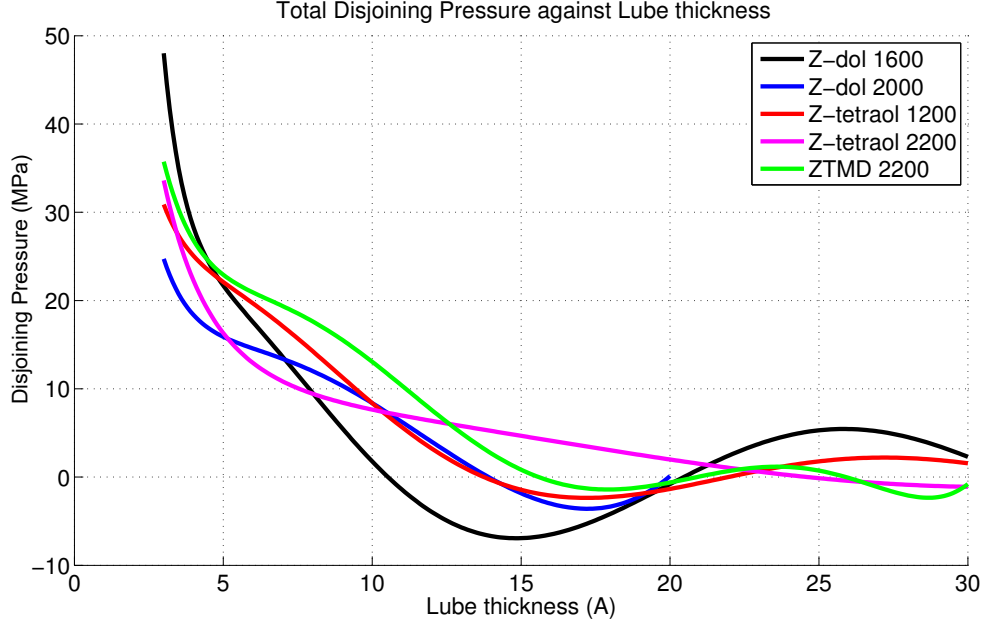
Figure 4.2: Total (sum of dispersive and polar components) disjoining pressure as a function of lubricant thickness for Z-dol 1600, Z-dol 2000, Z-tetraol 1200, Z-tetraol 2200, and ZTMD. It is noticeable that ZTMD and Z-tetraol 1200 have a close disjoining pressure and critical lubricant thickness (where $d\Pi/dh = 0$). This graphs are obtained according to Eq. 4.7 differentiating the surface energy function with respect to the lubricant thickness.

Fig. 4.2 shows the disjoining pressure derivative as a function of lubricant thickness. From this figure, the disjoining pressures for 5 cases of lubricants have been obtained via differentiating the surface energy with respect to lubricant thickness according to Eq. 4.7. In the governing equation, the disjoining pressure gradient $\boldsymbol{\nabla}\Pi$ plays the role of the restoring force. Using the chain rule, we can rewrite this gradient, $\boldsymbol{\nabla}\Pi$, in terms of lubricant thickness gradient, $\boldsymbol{\nabla}h$

$$\boldsymbol{\nabla}\Pi = \frac{d\Pi}{dh}\boldsymbol{\nabla}h \tag{4.10}$$

Therefore, the disjoining pressure gradient works as a restoring force only if $\frac{d\Pi}{dh} < 0$. This is true for all PFPE lubricants shown in Fig. 4.2 under a critical lubricant thickness of $\frac{d\Pi}{dh} = 0$. It should be noted that the critical thickness is slightly more than the dewetting thickness, the minimum surface energy point. This critical thickness is about 15, 17, 17, 30, and 18A for Z-dol 1600, Z-dol 2000, Z-tetraol 1200, Z-tetraol 2200, ZTMD, respectively. So, the disjoining pressure derivative $\frac{d\Pi}{dh}$ plays a key role in restoring the lubricant to its ideal undeformed state. Reference [36] names this quantity as "lubricant stiffness" and verifies that a stable state of lubricant requires this parameter to be negative.

Parameters	ZD1600	ZD2000	ZT1200	ZT2200	ZTMD
$A_{eff}(J)$	2.36e-20	4.59e-20	1.05e-19	0.95e-19	1.6e-19
$d_0(m)$	0	1.72e-10	2.5e-10	2.5e-10	3.1e-10
$d_1(m)$	4e-10	4e-10	2.5e-10	2.5e-10	3.1e-10
$\gamma_\infty(J/m^2)$	26e-3	15.8e-3	14e-3	14e-3	13e-3
a_0	0.356	0.806	0.968	1.51	1.121
a_1	0.944	0.482	0.988	-0.0152	0.351
a_2	-1.09	-0.480	-0.622	-0.0222	-0.0707
a_3	0.494	0.129	0.156	2.10e-3	-0.118
a_4	-0.10	-0.0106	-1.97e-2	6.81e-05	5.30e-2
a_5	1.256e-2		1.326e-3	-1.45e-05	-8.92e-3
a_6	-7.28e-4		-4.56e-05	5.56e-07	6.76e-04
a_7	1.68e-5		6.28e-07	-6.51e-09	-1.94e-05

Table 4.1: Surface Energy Parameters for Z-dol 2000, Z-tetraol 1200, Z-tetraol 2200, and ZTMD according to Refs. [35], [33], and [13]

4.3   Thin-film Effective Viscosity

References [12, 37] derived an explicit relation for viscosity of HDD lubricants as a function of temperature and film thickness, $\eta = \eta(T, h)$, by applying the method of absolute reaction rates to pure liquids. In this approach, also know as Eyring's rate theory [38], an explicit formula can be derived for viscosity, in terms of activation flow energy ΔE and entropy ΔS, describing the behavior of the PFPE lubricants for both bulk and thin-film modes. Using lubricant spin-off method, Ref. [37] conducted a comprehensive set of measurements for Z-dol and characterized the viscosity of this lubricant. In this method, the lubricant on the disk is under the shear stress due to the air flow on the lubricant-air interface, which causes the lubricant to flow radially in a timescale much longer than that for the airflow. Accordingly, an the effective viscosity (i.e. the equivalent constant viscosity across the lubricant thickness) is measured, although the viscosity might be non-uniform across the film. In contrast to the studies on Z-dol, no experiments have investigated the effect of material confinement on viscosity for Z-tetraol and ZTMD families. In this section, the activation parameters ΔE and ΔS are introduced and calculated for the bulk material using the measurements of viscosity at different temperatures. Then, the effect of material confinement on the activation parameters is estimated for Z-tetraol and ZTMD.

In order to obtain a proper estimation of the thin-film effective viscosity of each lubricant, one must first have a good estimation about the bulk behavior of the material. Then one can introduce assumptions on how and why the viscosity of a lubricant in the thin-film model is different. Karis [12] gives estimates of the bulk viscosity behavior of the Z-dol and Z-tetraol families of lubricants. In order to describe the bulk viscosity of the thin-film as a function of temperature, he applies Eyring's rate theory to the PFPE lubricants and provides the

equation

$$\eta(T) = \frac{N_A h_P}{V_l} exp(\frac{\Delta E^*_{vis} - T\Delta S^*_{vis}}{RT}), \tag{4.11}$$

which describes the viscosity as a function of temperature in which N_A, h_P, and V_l are Avogadro's number, Planck's constant and the molar volume of the lubricant, which can be calculated based on its molecular weight and density as:

$$V_l = \frac{M_w}{\rho}. \tag{4.12}$$

Also, in Eq. 4.11, the terms ΔE^*_{vis} and ΔS^*_{vis} are key parameters, the so called activation flow energy and entropy, respectively. Reference [12] finds the ΔE^*_{vis} and ΔS^*_{vis} for Z-dol and Z-tetraol using a curve fitting method on the experimental data of bulk viscosity of these materials as functions of temperature. So, by using two constants of ΔE^*_{vis} and ΔS^*_{vis}, we are able to express the bulk viscosity as a function of temperature. Reference [13] reports some experimental data of bulk viscosity of ZTMD as a function of temperature, as shown in Fig. 4.3. So, we can fit a curve using Eyring's theory on these experimental data and find the activation flow energy and entropy for ZTMD. Figure 4.3 shows the curve fitted on ZTMD experimental viscosities versus temperature as well as the bulk viscosities of Z-dol and Z-tetraol family of lubricants. Therefore, we can summarize the bulk activation flow
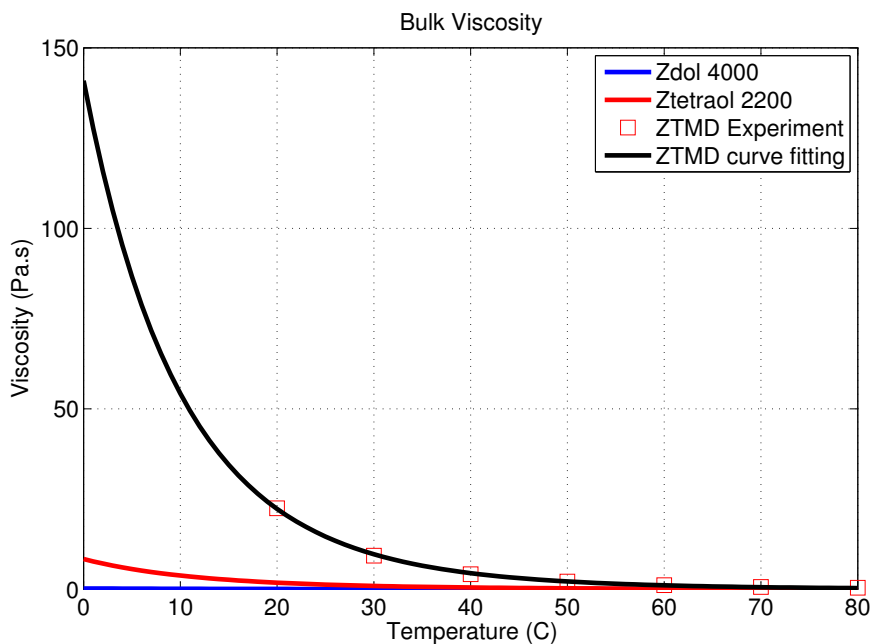
Figure 4.3: Bulk viscosity as a function of temperature for 3 different type of lubricants including Z-dol, Z-tetraol and ZTMD. It is clear that ZTMD has a greater viscosity compared to Z-tetraol and Z-tetraol compared to Z-dol.

energy and entropy for Z-dol, Z-tetroal and ZTMD in Table 4.2. The flow-activation entropy and energy have a great impact on viscosity since they appear in the exponential of Eq. 4.11

such that a slight modification in these parameters can considerably change the viscosity model.

Lubricant	$\Delta E_{vis}^*[KJ/mol]$	$\Delta S_{vis}^*[J/molK]$
Z-dol	34.7	9.87
Z-tetraol	50.8	44
ZTMD	61.4	59.2

Table 4.2: Bulk activation flow energy and entropy for different materials

The next step in establishing an accurate model for the physics of this problem is to amend the bulk viscosity model to a viscosity that also takes into account the effect of the thin-film regime. Reference [12] states that the ΔE_{vis}^* and ΔS_{vis}^* for bulk liquids can be amended to a new form of activation flow energy and entropy as a function of lubricant thickness as follows

$$\Delta E_{vis}(h) = \Delta E_{vis}^* - \frac{\mu(h)}{n}, \tag{4.13}$$

where$\Delta E_{vis}(h)$ is the activation flow energy for the thin film as a function of lubricant thickness h. ΔE_{vis}^* is the activation flow energy of the bulk material mentioned above, μ is the chemical potential, which is a function of the dispersive component of the disjoining pressure and the molar volume as follows

$$\mu(h) = V_l \Pi^d(h). \tag{4.14}$$

In Eq. 4.13, n is the ratio of activation evaporation energy to activation flow energy as follows:

$$n = \frac{\Delta E_{Evap}^*}{\Delta E_{vis}^*}. \tag{4.15}$$

Physically, the activation evaporation energy is equivalent to the energy needed to remove a molecule from the system of molecules and fill the remaining hole with the remaining liquid molecules. The activation flow energy is equivalent to the energy needed to move a molecule among other molecules. Normally, the ratio n between these two activation energies is around 3 to 5 depending on the molecular weight of the liquid and other factors. The ΔS_{vis}^* corresponding to the bulk material can also be amended to a new form of $\Delta S_{vis}(h)$ which is a function of lubricant thickness h; however, it is observed [37] that under a specific lubricant thickness of $2nm$, $\Delta S_{vis}(h)$ is constant for the Z-dol family. The term $\Delta S_{vis}(h)$ corresponds to the arrangement of the molecules and how this arrangement changes with the change in the state of the system. The arrangement of the molecules on a DLC substrate, and how they change during shearing, is almost the same for all types of PFPE lubricants that exhibit a spaghetti-like long carbon chain and polar end-groups that are attached to the disk. Therefore, we can assume that $\Delta S_{vis}(h)$ is constant for Z-tetraol and ZTMD lubricants as well. According to Ref. [12], we can write the new activation entropy as the sum of the bulk

value and a correction term as:

$$\Delta S_{vis}^{thin}(h) = \Delta S_{vis}^* + \Delta \tilde{S}(h), \tag{4.16}$$

where $\Delta \tilde{S}(h) = 0$ for the bulk material when h is large and $\Delta \tilde{S}(h)$ is constant for $h < 2nm$. Using a few iterations, we found that we can assume the same $\Delta \tilde{S}(h)$ for different PFPE lubricants, representing the difference between the thin-film and bulk modes. Such a choice gives a nicely estimated thin-to-bulk viscosity ratio $\eta(h)/\eta_\infty$. Assuming all these thin-film modifications, we amend Eyring's theory to a new form that accommodates the effect of lubricant thickness. Therefore, with a slight change, we can rewrite Eq. 4.11 in the form of

$$\eta(T,h) = \frac{N_A h_P}{V_l} exp(\frac{\Delta E_{vis}(h) - T\Delta S_{vis}^{thin}}{RT}). \tag{4.17}$$

Then using this equation, we can find the viscosity model for 3 different types of lubricants, Z-dol, Z-tetraol, and ZTMD. Fig. 4.4 shows the viscosity versus lubricant thickness for different temperatures for all 3 different types of lubricants. The viscosity shown in this figure for Z-dol has been used in former studies such as Refs. [12] and [15]; however, no published data is found for the viscosity of thin-film Z-tetraol and ZTMD. The viscosities found and shown in Fig. 4.4 for Z-tetraol and ZTMD are estimated based on the above explanations. In order to compare the viscosities of Z-tetraol and ZTMD with that for Z-dol, we plot in Fig. 4.5 the ratio of the viscosity between Z-tetraol and Z-dol as well as ZTMD and Z-dol. According to Fig. 4.5, the viscosity ratio of Z-tetraol to Z-dol varies between 1 and 80. The viscosity ratio of ZTMD to Z-dol is between 10 and 4000.

One may argue that such viscosity ratios are too high for lubricants that share the same structure. However, experiments on lubricant reflow show that this estimation is reasonable and the viscosity of Z-tetraol and ZTMD are far higher than Z-dol. Specifically, Ref. [22] studied the spreading of droplets of PFPE lubricants on unlubricated, carbon-overcoated disk surfaces. He reports the time needed for a droplet to spread over the disk and reports that as the number of hydroxyl groups on a molecular structure increases from zero, for Fomblin Z, to two for Z-dol, to four for Z-tetraol, to eight for ZTMD, the spreading time dramatically increases, which indicates the strong decrease in mobility of the lubricant and subsequently, a drastic increase in the effective viscosity. Therefore, such a high value of viscosity for Z-tetraol and ZTMD compared to Z-dol agrees with the experimental work by that reference.

4.4 Evaporation

The same approach that was used for viscosity of a thin-film is used for its evaporation. First, we introduce bulk evaporation properties of the materials and explain how we estimate them. Second, we use the disjoining pressure properties of the material to calculate the evaporation properties of the thin films. Finally, we can find the mass flux due to evaporation using the obtained data. The mentioned approach has been used in former studies [15, 12]. However, previous works estimate only the properties for the Z-dol family of lubricants but do not give any estimation about newer lubricants such as the Z-tetraol family and ZTMD. The
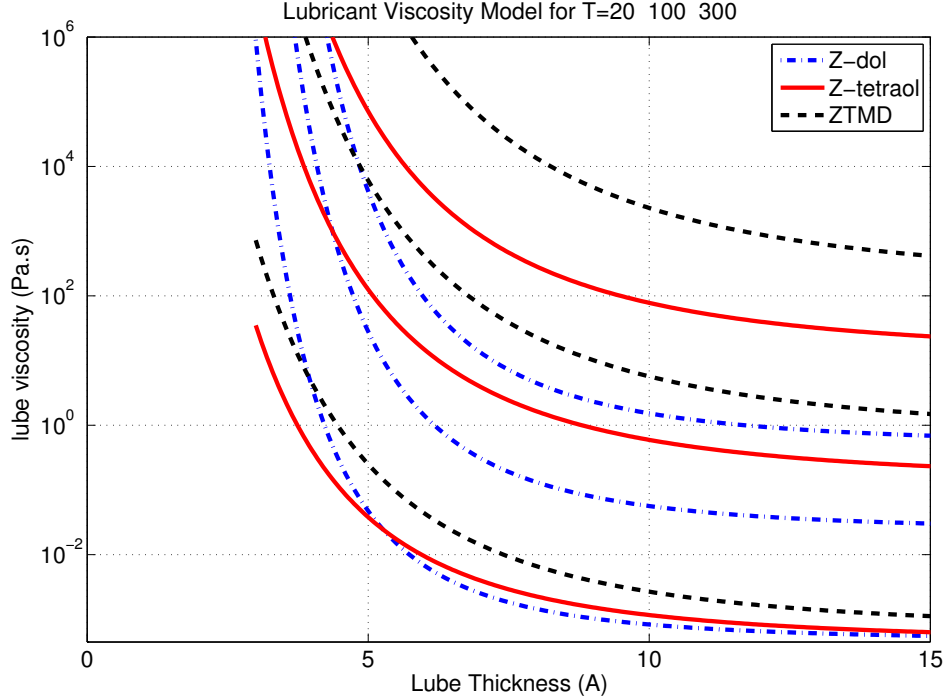
Figure 4.4: Thin-film effective viscosity as a function of lubricant thickness for different temperatures for different lubricants. For each lubricant, 3 graphs are plotted corresponding to viscosity as a function of temperatures: $T = \{20, 100, 300^oC\}$. Higher curves correspond to lower temperatures (closer to room temperature)

vapor pressure of PFPEs depends on many factors among which the temperature, molecular weight, activation evaporation energy and entropy stand out. Therefore, we can write the vapor pressure of the liquid in the form of $P_{vap}^* = p(M_w, T, \Delta E_{vap}^*, \Delta S_{vap}^*)$. Reference [12] applied the Clapeyron equation to estimate the vapor pressure of the pure liquid lubricant, which can be represented as

$$P_{vap}^* = p_0 exp(\frac{-\Delta E_{vap}^* - T\Delta S_{vap}^* + RT}{RT}). \tag{4.18}$$

This equation suggests that for bulk liquids, the activation evaporation energy and entropy are functions of molecular weight and temperature. For the Z-dol family of lubricants, experimental measurements of vapor pressure exhibit a linear relation between the molecular weight and the activation evaporation energy. Reference [12] states that this relation for Z-dol has the form

$$\Delta E_{vap}^*[KJ/mol] = 50 + 29M_w[Kg/mol] \tag{4.19}$$

which comes from the comparison between the simulated data and the experimental data obtained from thermogravimetric analysis (TGA). However, there is no such useful accurate experimental information about the Z-tetraol family of lubricants. So, we need to somehow estimate this key parameter in order to predict the bulk vapor pressure of Z-tetraol as well as ZTMD. To find an expression for the activation evaporation energy of the Z-tetraol family, we
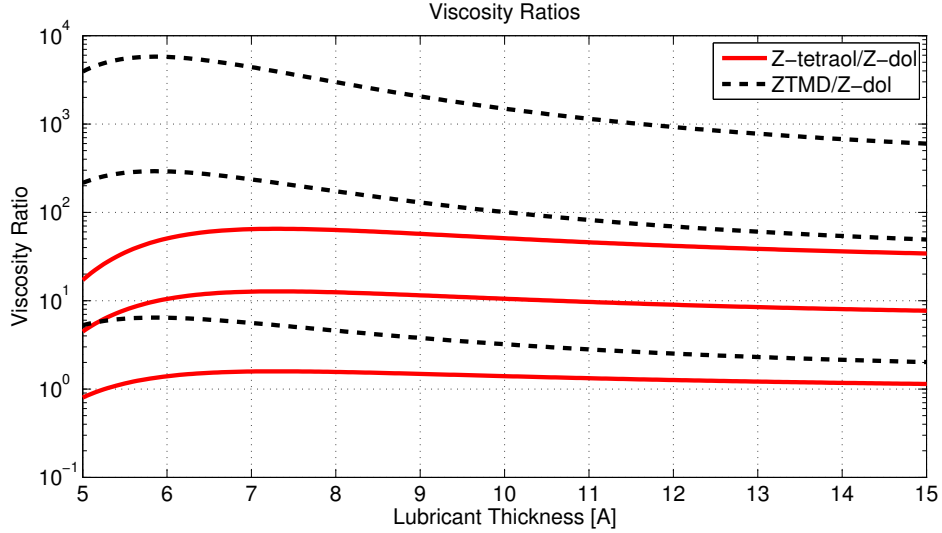
Figure 4.5: Thin-film effective viscosity ratio of Z-tetraol to Z-dol and ZTMD to Z-dol as a function of lubricant thickness for different temperatures for different lubricants. This is a comparison between these families of lubricants at temperatures $T = \{20, 100, 300^oC\}$. Higher curves correspond to lower temperatures (closer to room temperature)

make the same assumption of a linear relation between ΔE_{vap}^* of Z-tetraol and its molecular weight M_w, with two unknown parameters of β_1 and β_2 to be determined, and we write

$$\Delta E_{vap}^* = \beta_1 + \beta_2 M_w \tag{4.20}$$

By comparing the equation above with Eq. 4.19, we find $\beta_1 = 50 KJ/mol$ and $\beta_2 = 29 KJ/Kg$ for the Z-dol family of lubricants.

The physics of evaporation and viscosity are very close to each other. In evaporation, some energy is injected into the system to activate the molecules to escape from the liquid phase. In viscosity, the activation energy is needed for molecules to overcome the bonds and van der Waals forces between the liquid and substrate molecules, and, in the case of thin-film shear motion, move along the disk. So, there must be a quantitative relation between these two activation energies. Eq. 4.15 illuminates this relation in terms of a parameter n. According to the literature [12], the parameter n should be in the range of 3 to 5 depending on the lubricant's molecular weight for the class of HDD lubricants (For Z-dol between 2.3 and 4.8). Due to the lack of enough experimental information about this parameter for the Z-tetraol family, we consider the same range as for Z-dol, and therefore, we can formulate an inequality for Z-tetraol:

$$2.3 \leq n = \frac{\Delta E_{Evap}^*}{\Delta E_{vis}^*} \leq 4.8 \tag{4.21}$$

Our calculations show that we can extract two limits of low molecular weight $M_w = 1200 Da$

and high molecular weight $M_w = 4000 Da$ for this inequality and write

$$\Delta E^*_{vap} = \beta_1 + \beta_2 M_w = 2.3 \Delta E^*_{vis} \qquad M_w = 1.2 [Kg/mol] \qquad (4.22)$$

$$\Delta E^*_{vap} = \beta_1 + \beta_2 M_w = 4.8 \Delta E^*_{vis} \qquad M_w = 4 [Kg/mol] \qquad (4.23)$$

Solving this system of equations and knowing $\Delta E^*_{vis} = 50.8 [KJ/mol]$ for Z-tetraol, we obtain the parameters $\beta_1 = 61 KJ/mol$ and $\beta_2 = 45.7 KJ/Kg$.

Researchers and engineers have a tendency to use longer and heavier molecule chains in lubricant design to suppress the effect of evaporation as much as possible; but, there is a trade-off between disjoining pressure properties and evaporation properties of the lubricants. According to Ref. [13], ZTMD as a multi-dentate lubricant, which is made of two Z-tetraol short chain molecules (1000 Da), has the critical lube thickness and disjoining pressure properties close to those of Z-tetraol 1200; while, it should have the evaporation properties of Z-tetraol 2200. This appears to be correct because the disjoining pressure behavior of the ZTMD is close to that for Z-tetraol 1200 according to Fig. 4.2. And, the molecular weight of ZTMD is close to that of Z-tetraol 2200. Therefore, it is reasonable to assume the same bulk evaporation properties for Z-tetraol 2200 and ZTMD in this study, assuming Z-tetraol 2200 and ZTMD have the same molecular weight.

Chapter 5

Simulation of Viscous Lubricant Depletion under HAMR conditions

The integrated HAMR system has a laser delivery system that conveys the energy to the magnetic layer and heats the target point above the Curie temperature in order to perform a proper process of magnetic flux reversal and hence write on the media. The lubricant coating on the disk plays a vital role in the stability of the slider's flying over the disk. In the HAMR technology, this lubricant layer is subjected to the high temperature and depletes at the target point due to evaporation and thermo-capillary shear stress. The resulting non-uniform lubricant profile can cause slider modulations leading to the poor mechanical stability for the HDI, as seen in some experiments [39].

We investigate the problem of evolution of lubricant thickness under laser illumination. The physics of heat transfer from the Near Field Transducer (NFT) to the magnetic media and the reverse nano scale heat transfer from media to NFT are still matters of discussion and are not yet well understood. To avoid such complication, we prescribe a Gaussian temperature distribution on the disk (Eq. 2.1) and therefore on the lubricant with a full width half maximum (FWHM) close to that of the so-called laser spot. In this study the FWHM is set to the goal of the hard disk industry, which is $20nm$. In addition, the last result section of this chapter discusses the effect of the laser spot size on the lubricant depletion by presenting the depletion for different laser spot sizes of $L = 20nm, 100nm, 1\mu m$. The maximum temperature of the laser spot is set to 350^oC for all cases, and the ambient condition is $T_0 = 25^oC$ and $p_0 = 1atm$, close to the target of proposed HAMR systems [40]. In this study the effects of external shear stress and pressure from the air bearing are neglected since they change on a length scale of a few microns; while, in the laser spot the thermo-capillary shear stress and disjoining and Laplace pressures change on a length scale of few nanometers (of the order of laser spot size). Therefore, the gradients of thermo-capillary shear stress and disjoining and Laplace pressures at the laser spot are far higher compared to the mechanical shear stress and pressure from the air bearing, by a factor of a thousand. According to the governing equation (Eq. 3.19), the evaporation and thermo-capillary shear stress are the driving forces for the lube depletion, while disjoining pressure gradient plays the role of a restoring force, and viscosity would be the resistance against the fluid motion.

5.1 Effect of Hydroxyl End-groups on Lubricant Depletion

Previously, Ref. [15] studied the lubricant deformation for Z-dol 2000 with two hydroxyl end-groups for different maximum temperatures, different cases of disjoining pressure, and different possibilities for the evaporation model. Here, we perform some simulations on the Z-dol and Z-tetraol families with 2 and 4 hydroxyl end-groups, including Z-dol 1600 and Z-tetraol 1200 as low molecular weight members and Z-dol 2000 and Z-tetraol 2200 as high molecular weight members, and also, on ZTMD ($M_w = 2200Da$) with 8 hydroxyl end-groups as a multi-dentate lubricant, which is manufactured based on the Z-tetraol family. All studies are performed for 4 cases of lubricant thickness including 0.5, 0.7, 1.2, and 1.4nm. These numbers are chosen to provide a fair comparison with the previous study on Z-dol.

Since both evaporation and thermo-capillary shear stress are the driving forces for lubricant depletion, it is essential to figure out which one has a more significant role. In section 5.2, we discuss the relative effect of evaporation with respect to the thermo-capillary shear stress.

After a $2ns$ illumination of the laser, a trough and two side ridges along the down-track direction can be seen in the lubricant. Figure 5.1 shows an example of the trough and the side ridges. The performance of the lubricants can be ranked mainly based on the trough depth and evaporation in that better lubricants show less deformation and trough depth under equal conditions of thermal spot size and peak temperature.
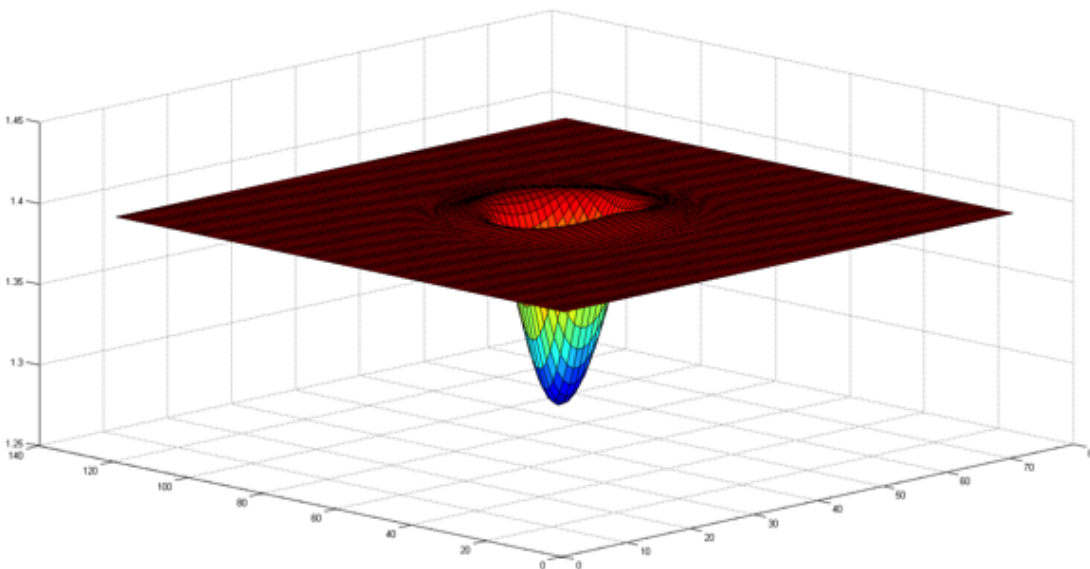
Figure 5.1: An example of the lubricant depletion including trough and side ridges for a typical laser shine condition of $2ns$ illumination with $20nm$ laser spot and 350^oC peak temperature of the spot.

Figures 5.2, 5.3, 5.4, and 5.5 show the simulation results for 0.5, 0.7, 1.2, and 1.4nm film thicknesses, respectively. Figure 5.2 shows a comparison between the different lubricants

with 0.5nm initial lubricant thickness. For all 4 cases of lubricants at 0.5nm thickness, the deformation is less than 4% of the initial lubricant thickness, which is negligible. This graph shows the accuracy and stability of the numerical method since the method is working for such an ultra-thin film as small as 0.5nm.
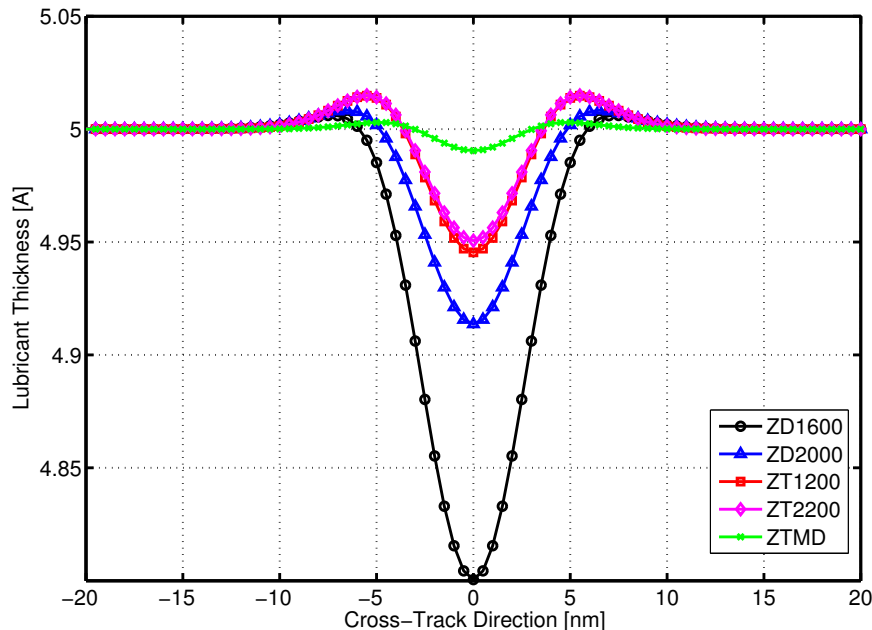
Figure 5.2: Final lubricant thickness profile for different lubricants at 5A initial lubricant thickness($h_0 = 5A$) after $2ns$ of laser shine.

Figure 5.3 shows a comparison of the lubricant with 0.7nm initial thickness. The deepest trough in this case belongs to Z-dol 1600 which has almost 15% of the initial thickness ($1A$). The deformation for the Z-tetraol family is around 8% of the initial thickness, which is less than that for the Z-dol family. ZTMD exhibits a 4% trough depth, which is less than all other lubricants. This shows the superiority of the performance of ZTMD in sub-nanometer thin-film regimes.
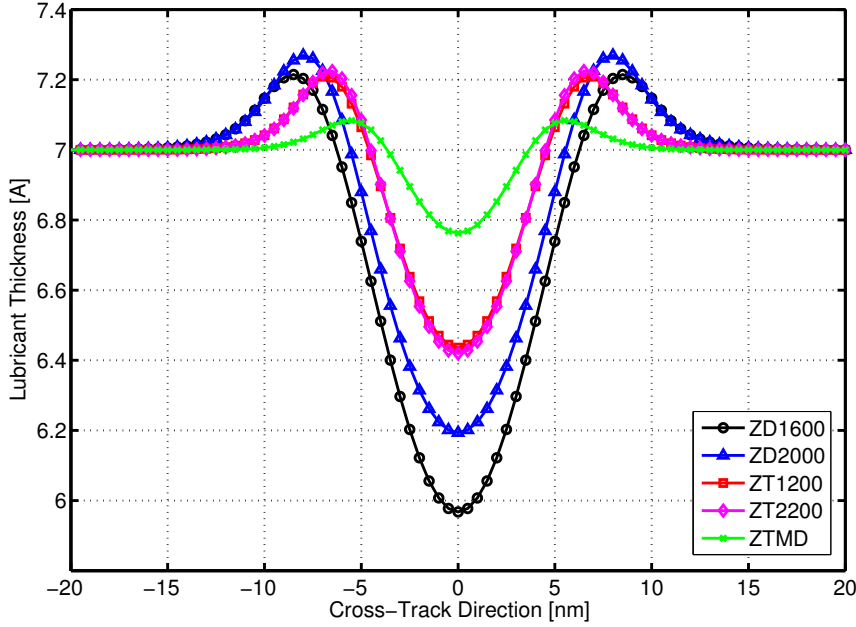
Figure 5.3: Final lubricant thickness profile for different lubricants at 7A initial lubricant thickness($h_0 = 7A$) after $2ns$ of laser shine. The profiles of Z-tetraol 1200 and 2200 nearly coincide.

Figure 5.4 shows that for a case of 1.2nm film thickness the Z-dol family and Z-tetraol 2200 show considerable trough depths between $4A$ and $5A$, which is more than 30% of the initial thickness. Z-tetraol 1200 and ZTMD show less deformation in this case ($3A$ and $2A$ respectively). Z-tetraol 2200 shows a considerable deformation, which can be explained by its weaker disjoining derivative $\Pi'(h)$, according to Fig. 4.2. Again in this case, we can see that ZTMD shows a better performance. It has less evaporation, less lubricant mobility, and stronger disjoining pressure derivative compared to other lubricants, which explains the performance of this lubricant.
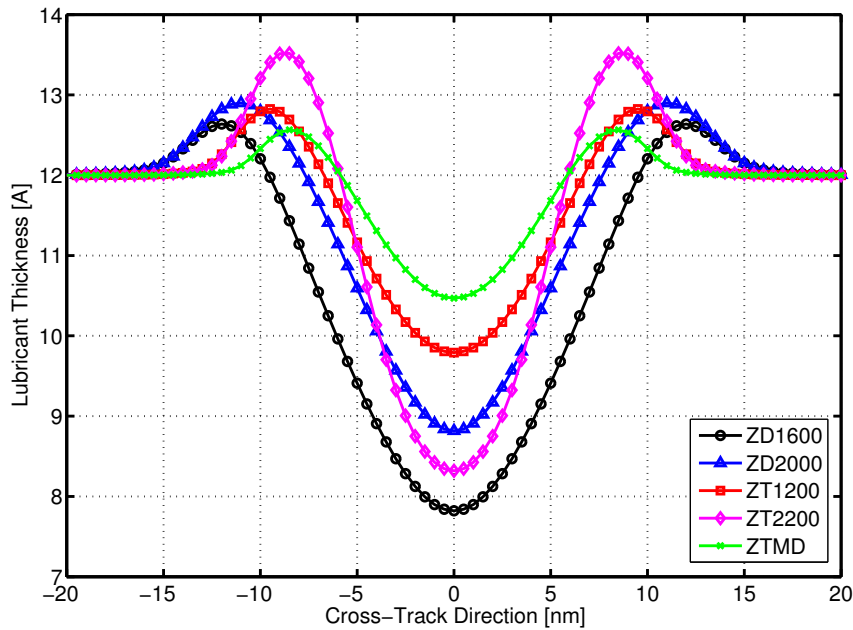
Figure 5.4: Final lubricant thickness profile for different lubricants at 12A initial lubricant thickness($h_0 = 12A$) after $2ns$ of laser shine. Z-tetraol 2200 exhibits a huge deformation due to its weak film stiffness (low disjoining pressure derivative)

For the case of $1.4nm$ initial lubricant thickness, Fig. 5.5 shows the same regime as seen in the $1.2nm$. In this case, Z-dol 1600 and Z-tetraol 2200 exhibit relatively large trough depths of 6A and 7A respectively, that are more than 40% of the initial thickness while the deformation for the Z-tetraol 1200 is less, and it is still less than 3A for ZTMD.
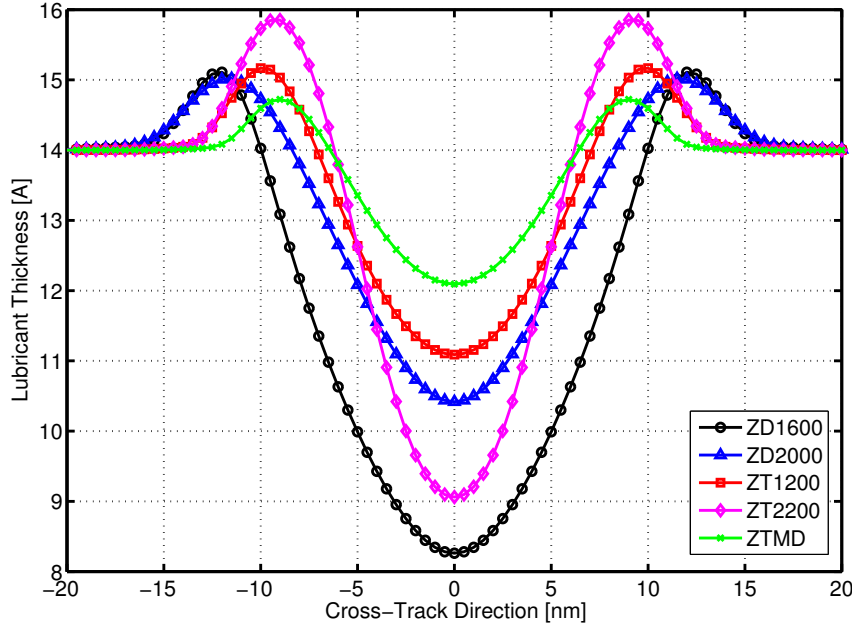
Figure 5.5: Final lubricant thickness profile for different lubricants at 14A initial lubricant thickness($h_0 = 14A$) after 2ns of laser shine.

All four figures imply that ZTMD shows a better performance under HAMR conditions compared to the other types of lubricants. This behavior comes from its better bonding properties which leads to better viscosity, evaporation and disjoining pressure properties.

5.2   Evaporation under HAMR Conditions

As discussed earlier, the lubricant depletion under HAMR conditions can be due to both evaporation and thermo-capillary effects. The results of our simulations show that evaporation contributes in lubricant depletion relatively less than the thermo-capillary shear stress. We observe that almost 25% of the depletion is due to evaporation for Z-dol 1600, and it is almost 5% for Z-tetraol 1200 and Z-dol 2000. For the case of Z-tetraol 2200 and ZTMD the contribution of the evaporation is almost negligible in all cases.

As discussed in Section 4.4, the contribution of the evaporation in the depletion process can be described by the bulk vapor pressure and the evaporation activation energy of the materials, which are directly functions of their molecular weight and number of hydroxyl end-groups. Z-dol 2000, according to Eq. 4.19, has an activation evaporation energy of $108KJ/mol$. The value for Z-tetraol 1200 as a short chain molecule, is $115.8KJ/mol$ according to Eq. 4.20. Since we assume a similar molecular weight for Z-tetraol 2200 and ZTMD, both lubricants will share the value of $\Delta E^*_{vap} = 170.7KJ/mol$ according to Eq. 4.20. Eq. 4.17 shows the importance of the activation evaporation energy on the bulk pressure of the material; as ΔE^*_{vap} increases, the p_{vap} and, consequently, $\dot{m}$ decrease exponentially. Fig. 5.6 also supports this argument since it shows a considerably lower mass flux due to evaporation for Z-tetraol 2200 and ZTMD.
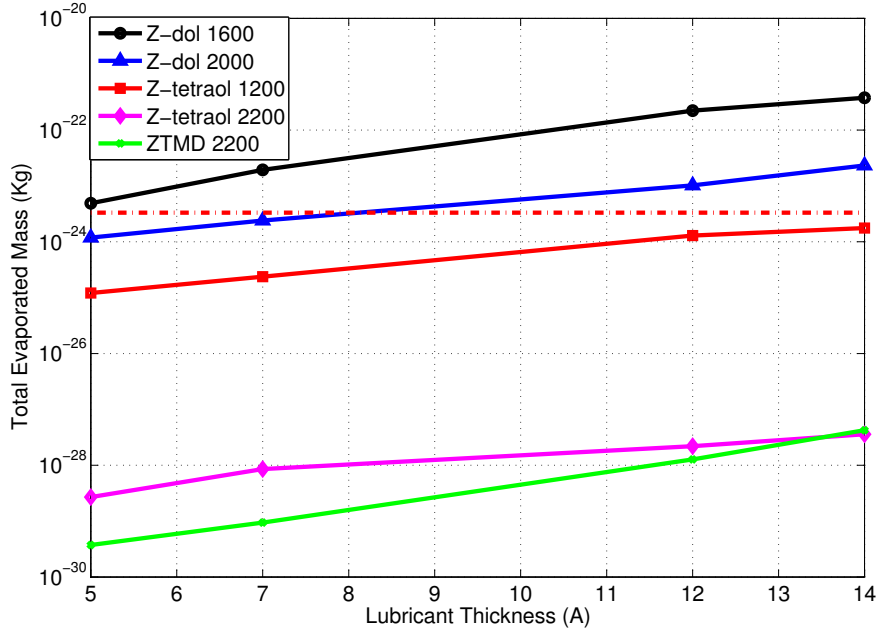
Figure 5.6: Evaporation as a function of lubricant thickness for different lubricants. As the lubricant thickness increases, the amount of evaporation also increases since the lube bonding ratio decreases. ZTMD and Z-tetraol 2200 exhibit much less evaporation due to their smaller bulk evaporation pressure. The red dashed line represents the mass of a typical molecule with $M_w = 2000Da$

Hence, we can distinguish the thermo-capillary shear stress as the main driving force for depletion in Z-tetraol 2200 and ZTMD. Additionally, comparing the deformation of ZTMD with those for Z-dol and Z-tetraol (Figs. 5.2-5.5) we conclude that this lubricant is more resistant against motion (due to its high viscosity and low mobility), and it has a stronger restoring force (due to disjoining pressure gradient).

The effect of molecular weight on evaporation is also of interest here. Fig. 5.6 implies that an increase in molecular weight from Z-tetraol 1200 to Z-tetraol 2200 decreases the evaporation by a factor of 10^{-4}. Also, the molecular weight increase from Z-dol 1600 to Z-dol 2000 decreases the evaporation by a factor of 10^{-2}. So, increasing the molecular weight decreases the evaporation significantly, which is desired for HAMR lubricants. On the other hand, Fig. 4.2 for Z-tetraol 1200 and 2200 shows that increasing the molecular weight decreases the lubricant stiffness ($d\Pi/dh$) and therefore, weakens the restoring force of the lubricant, which is the disjoining pressure gradient in this case. That is why Z-tetraol 2200 exhibits greater trough depths compared to Z-tetraol 1200. So, there is a trade-off in increasing the molecular weight of the Z-tetraol lubricant. As the molecular weight increases, the evaporation properties improve while the disjoining pressure gradient becomes weaker, making the lubricant more vulnerable against thermo-capillary shear stress.

Depending on whether the thermo-capillary or evaporation effects are dominant, the depletion profile changes. The depletion profile depends on the shape of the trough and side ridges. In cases where the evaporation is more dominant, our results show that the side

ridges are smaller and the trough is wider, whereas for the cases of the thermo-capillary dominant regime, the side ridges are larger and more comparable to the trough depth. This observation can be useful for future experiments on lubricant deformation under HAMR conditions to determine the relative effect of evaporation.

5.3 Depletion Rate

As the laser is exposed to the disk, the uniform layer of the lubricant deforms and the trough grows. As shown in Figs. 5.2-5.5, the depth of the trough is defined as the distance between the highest point of the side ridges and the lowest point of the trough. Figure 5.7 shows the trough depth (in Angstrom) versus time (for a scope of $2ns$ laser-shine) for different lubricants and different initial lubricant thicknesses with $FWHM = 20nm$.
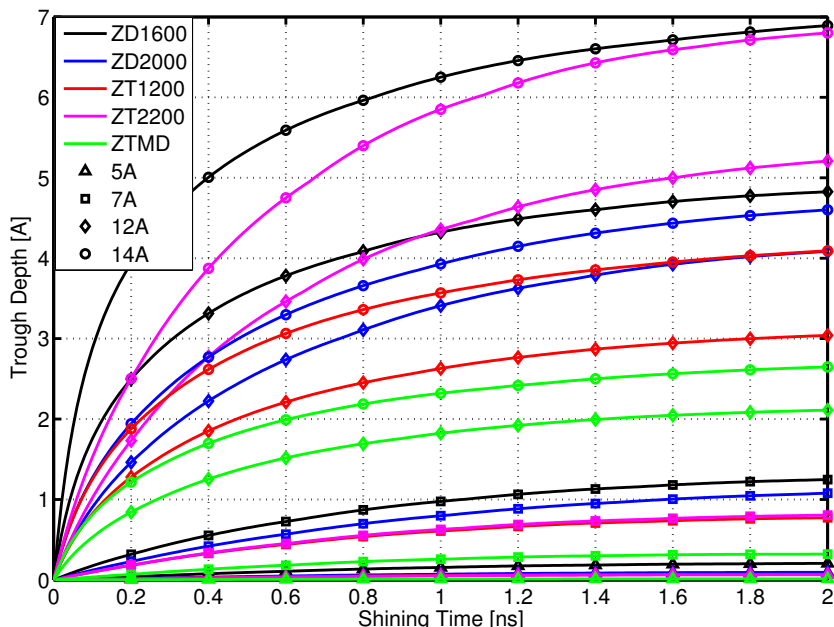
Figure 5.7: Trough depth versus time for different lubricants (different colors) and different initial lubricant thicknesses (different markers).

Figure 5.7 indicates that the trough grows fast initially. However, as the exposure continues, the depletion speed decreases. This behavior can be explained by viscosity and disjoining pressure properties. As the trough grows, evaporation decreases and the viscosity and disjoining pressure gradient increase. Higher viscosity leads into lower lubricant mobility and therefore, slower depletion. A larger trough not only has a higher lube thickness slope $\partial h / \partial x$, but it also has a higher disjoining pressure derivative $d\Pi/dh$ since the lube thickness is decreased (according to Fig. 4.2). Therefore according to the chain rule Eq. 4.10, as the trough grows, the disjoining pressure gradient increases and the lubricant depletion process slows because the disjoining pressure gradient plays the role of the main restoring force in this problem.

5.4 Laser Spot Size Effect

In the previous sections, we presented the simulation results for Z-dol 1600, Z-dol 2000, Z-tetraol 1200, Z-tetraol 2200, and ZTMD (2200) under HAMR writing conditions for an exposure time of $t_{ex} = 2ns$, a laser spot size of $L = 20nm$, and a HAMR peak temperature of $T_p = 350^o C$. In this section, we select Z-dol 2000, Z-tetraol 2200, and ZTMD with similar molecular weights to study the effect of laser spot size (FWHM) on the lubricant depletion behavior. In addition to $L = 20nm$, we included the laser spot size of $1\mu m$, close to that used in experiments in which the focusing is optical, and an intermediate laser spot size of 100nm similar to the previous work on Z-dol [16]. Each laser spot size has a specific exposure time proportional to its laser spot size. We expose the laser spot sizes of L =20nm, 100nm, and $1\mu m$ for durations of $2ns$, $10ns$, and $100ns$, respectively. These exposure times are enough for the troughs to fully develop. Figure 5.8 shows the results of these simulations.

Our results include film thicknesses of $h_0 = 0.7, 1.0, 1.2, 1.4nm$ for Z-dol 2000, $h_0 = 1.0, 1.2, 1.4, 2.0, 2.1, 2.2nm$ for Z-tetraol 2200, and $h_0 = 1.0, 1.2, 1.4, 1.6$ for ZTMD. Lubricant films with larger thicknesses are avoided since they show a dewetting behavior with unstable disjoining pressure properties ($d\Pi/dh > 0$). Also, lubricants with smaller thicknesses ($h_0 < 1nm$) are mostly avoided since the lubricant depletion is negligible in that case [41]. Reference [15] developed the set of simulations for Z-dol 2000, under HAMR writing conditions whose results are included here in Fig. 5.8 and are compared with our simulation results for Z-tetraol 2200 and ZTMD, using the same Finite Volume method. Accordingly, Fig. 5.8
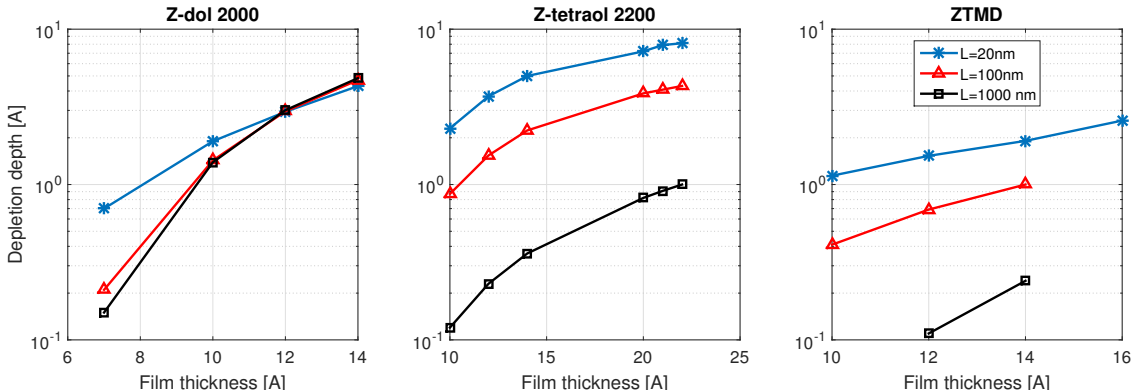
Figure 5.8: Trough depth as a function of the initial film thickness for different lubricant types, and different laser spot sizes of $L = 20nm, 100nm, 1\mu m$

shows the trough depth as a function of film thickness for each lubricant, and laser spot size. It shows that, for Z-tetraol and ZTMD, the larger laser spot sizes have significantly smaller depletion depths. However, for larger film thicknesses of Z-dol 2000, it shows that the depletion depth is almost the same for different laser spot sizes, since the curves coincide for larger film thicknesses.

As discussed in Section 5.2, unlike Z-dol, the evaporation is small for Z-tetraol 2200 and ZTMD since they have a strong bonding to the disk. Therefore, the main source of the lubricant depletion is the thermo-capillary shear stress, for these two lubricant types. So

for Z-tetraol and ZTMD, increasing the laser spot size (FWHM) decreases the intensity of the temperature and surface tension gradients, leading to a major decrease in the lubricant deformation and trough depth. But for Z-dol, the main source of depletion is evaporation, and therefore, the depletion is almost the same for different laser spot sizes. This explains why Z-dol 2000, in Fig. 5.8, has a different depletion behavior than Z-tetraol and ZTMD for different laser spot sizes.

5.5 Discussion

We found in this study that as the number of functional end-groups in a PFPE lubricant increases, a number of effects can be observed in the behavior of the lubricants, such as an increase in viscosity, a decrease in mobility, and a considerable decrease in evaporation; specifically, evaporation almost vanishes in the cases of Z-tetraol 2200 and ZTMD, which agrees with experimental measurements of the vapor pressure for these lubricants [42]. As the molecular weight and the backbone chain length increase, a decrease in depletion due to evaporation can be observed as well as an increase in depletion due to disjoining pressure effects. Simulations predict relatively small depletion for ZTMD, which can be attributed to its evaporation and disjoining pressure properties and the low mobility of this lubricant. We also found that the depletion speed decreases with time. During the $2ns$ laser exposure, all the cases reach almost 70% of their final trough size after $1ns$.

No experimental data could be found for $20nm$ laser spots to be compared with the predictions of this study. The laser spot size in the experiments can be only as low as a few hundred nanometers due to the resolution of the Optical Spectrum Analyzers (OSA) and the limit of the Near Field Transducers. However, this study predicts the effects of lubricant design parameters such as molecular weight and polar end-groups and their impact on disjoining pressure, viscosity, mobility, and evaporation properties of the lubricants, which alter the performance of the lubricant under HAMR conditions. It should also be observed that the Z-dol family of lubricants as well as Z-tetraol and ZTMD are conventional lubricants that cannot resist against high temperatures since thermal degradation is serious issue for these lubricants at greater temperatures beyond $350^{o}C$. In order to avoid uncertainties with regard to the thermal decomposition of the lubricants, we kept the peak temperature of the laser spot at a medium temperature of $350^{o}C$ [43]. Another issue is the polydispersivity of the polymer molecules, which is not considered in this study since the experimental data for these lubricants are scarce, specifically for the Z-tetraol and ZTMD family.

Chapter 6

Simulation of Viscous Lubricant Reflow after Laser Exposure

In the head-disk interface (HDI), the lubricant covering the disk plays a vital role in the stability of the slider's flying over the disk. In the developing HAMR technology, the disk is exposed to a laser irradiation during the writing process, causing the lubricant to deplete due to evaporation, thermal-degradation, and thermo-capillary effects. The resulting non-uniform lubricant profile can cause slider modulations leading to the poor mechanical stability for the HDI, as seen in some experiments [39]. A good lubricant design should lead to rapid recovery in the lubricant profile to maintain the HDI reliability. Accordingly, there is a need to better understand the lubricant behavior during the recovery process, especially prior to the next reading/writing cycle (one disk rotation) which can happen within $4-10ms$.

In this chapter, we present the results of simulations for the lubricant reflow after the disk has been subjected to HAMR conditions. Chapter 5 presented the simulation results for the behavior of a group of lubricants under laser irradiation, including Z-dol, Z-tetraol, and ZTMD with various molecular weights [41]. Here, we focus on the effect of the molecular end-groups by selecting Z-dol 2000, Z-tetraol 2200, and ZTMD with the same molecular weights. Molecular weight should be equal across the lubricants since it has a significant impact on the thin-film material properties such as viscosity, vapor pressure, and disjoining pressure [36].

As discussed in Chapters 2 and 5, we assumed that the lubricant was irradiated by a Gaussian temperature distribution with a Full Width Half Maximum (FWHM) of $L = 20nm$ and a peak temperature of $T = 350^oC$, close to the target for HAMR [44]. Additionally, Chapter 5 discussed the effect of the laser spot size on the lubricant depletion for three laser spot sizes of $L = 20nm, 100nm, 1\mu m$. These results presented in Chapter 5 are used as the initial conditions for the recovery (reflow) simulations presented here. After the laser irradiation, we assume the lubricant cools to room temperature immediately, so during the reflow process the lubricant is isothermal, and the thin-film properties such as viscosity and disjoining pressure are functions of only the lubricant thickness. The lubricant starts from a deformed profile, and it transitions to a uniform profile after a certain time period known as the recovery time.

Using a similar method, Refs. [15, 16] investigated the effects of the laser spot size and lubricant thickness on the depletion and recovery behavior of Z-dol 2000, a widely used

lubricant in the HDDs in 1990s. Here, we investigate the effect of hydroxyl end-groups on the recovery time by studying more modern lubricants such as Z-tetraol and ZTMD, and draw a performance comparison between the different types of lubricants with similar molecular weights. We follow the Finite Volume method developed in Refs. [15, 16] but have improved the efficiency of the numerical scheme up to 10X.

After each set of simulations under HAMR conditions, we impose the ambient temperature on the lubricant and let it reflow to less than 0.01nm depletion, about the resolution of the optical surface analyzers (OSA). Our results include film thicknesses of $h_0 = 0.7, 1.0, 1.2, 1.4nm$ for Z-dol 2000, $h_0 = 1.0, 1.2, 1.4, 2.0, 2.1, 2.2nm$ for Z-tetraol 2200, and $h_0 = 1.0, 1.2, 1.4, 1.6$ for ZTMD. Lubricant films with larger thicknesses are avoided since they show a dewetting behavior with unstable disjoining pressure properties ($d\Pi/dh > 0$). Also, lubricants with smaller thicknesses ($h_0 < 1nm$) are mostly avoided since the lubricant depletion is negligible in that case (Chapter 5). References [15] and [16] developed the set of simulations for Z-dol 2000, under HAMR writing and recovery conditions respectfully, whose results are included here and are compared with our simulation results for Z-tetraol 2200 and ZTMD, using the same finite volume method.

6.1 Effect of Material Properties on Reflow

6.1.1 Effective Viscosity

The viscosity $\eta(T, h)$ (a function of local thickness and temperature) for the lubricants of this study is introduced and discussed in Section 4.3. In this chapter we simulate the Post-HAMR recovery process assuming the temperature has cooled down to room temperature. Accordingly, the viscosity needs to be calculated for the Post-HAMR recovery condition with a uniform lubricant temperature of $T = 25^oC$. Therefore, the thin-film viscosity is only a function of the local lubricant thickness $\eta = \eta(h)$.

Figure 6.1 presents the viscosity η as a function of the lubricant thickness h for Z-dol, Z-tetraol, and ZTMD. This figure shows that at the room temperature conditions, the viscosity for ZTMD is about one order of magnitude larger than that for Z-tetraol and is two orders larger than for Z-dol. It also shows that the thin-film viscosity increases rapidly as the lubricant thickness decreases to less than 5 Angstroms. As discussed in Chapter 5, this huge difference in viscosity is the main reason for the significant decrease in the lubricant depletion for sub-nanometer thick lubricants, when comparing the three families of lubricants.

Since viscosity experimental measurements for Z-tetraol and ZTMD are very limited in the literature, we have calculated their viscosities using the same method as in [12] and shown in Fig. 6.1. In the future, the results of this study can be compared with reflow experiments to verify the thin-film viscosity model presented in this work.

6.1.2 Disjoining pressure properties

The inter-molecular forces between the thin-film lubricant and its substrate, and between the lubricant and air, can be modeled in terms of the disjoining pressure [29]. In the lubricant
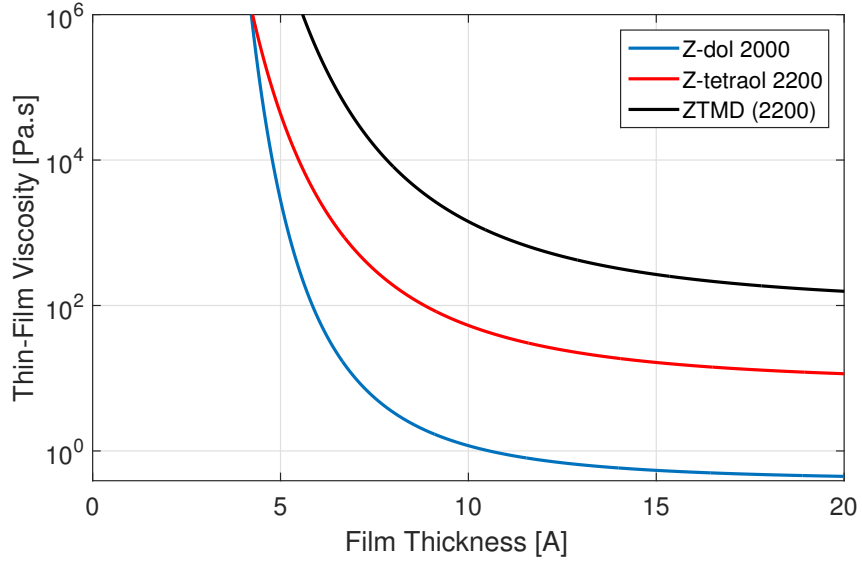
Figure 6.1: viscosity $\eta(h)$ as a function of lubricant thickness h at room temperature $T = 25^oC$ for Z-dol 2000 [15], Z-tetraol 2200, and ZTMD [41].

recovery after HAMR conditions, the main driving force for reflow is the disjoining pressure gradient.

The reflow governing equation (Eq. 3.20) shows that the pressure gradient ∇p is the driving force for the lubricant to recover, and the disjoining pressure gradient $\nabla \Pi$ is a significant portion of ∇p. As discussed in Eq. 4.10 The disjoining pressure is solely a function of the lubricant thickness $\Pi = \Pi(h)$ and therefore, we can use a chain rule to relate the disjoining pressure gradients to the film thickness gradient as $\nabla \Pi = d\Pi/dh.\nabla h$ where $d\Pi/dh = \Pi'(h)$ is the disjoining pressure derivative. So, the recovery time directly depends on the disjoining pressure derivative, and the intensity of the lubricant thickness gradient ∇h.

In Section 4.2, we introduced the disjoining pressure and surface energy measurements for the Z-dol, Z-tetraol, and ZTMD families of lubricants. Based on the measurements, we can calculate the disjoining pressure derivative $d\Pi/dh$, and the results are presented in Fig. 6.2.

The disjoining pressure is the restoring force for the lubricant displacement, and therefore, the lubricant thickness in the governing equation (Eq. 3.20) is stable only if the disjoining pressure derivative is negative, i.e. $d\Pi/dh < 0$. When this condition is met, the Poiseuille flow due to the disjoining pressure gradient directs from the higher to the lower thickness regions, similar to a stable diffusion equation. The term "film stiffness" was introduced in Ref. [36] for the disjoining pressure derivative $d\Pi/dh$ since it represents the lubricant's ability to resist mechanical disturbances and to reflow quickly if depleted.

Figure 6.2 shows that the condition $d\Pi/dh < 0$ is met for all of the lubricants with lubricant thickness smaller than a critical lubricant thickness in which $d\Pi/dh = 0$. This critical film thickness is around 1.5nm for Z-dol 2000, 2.3nm for Z-tetraol 2200, and 1.8nm
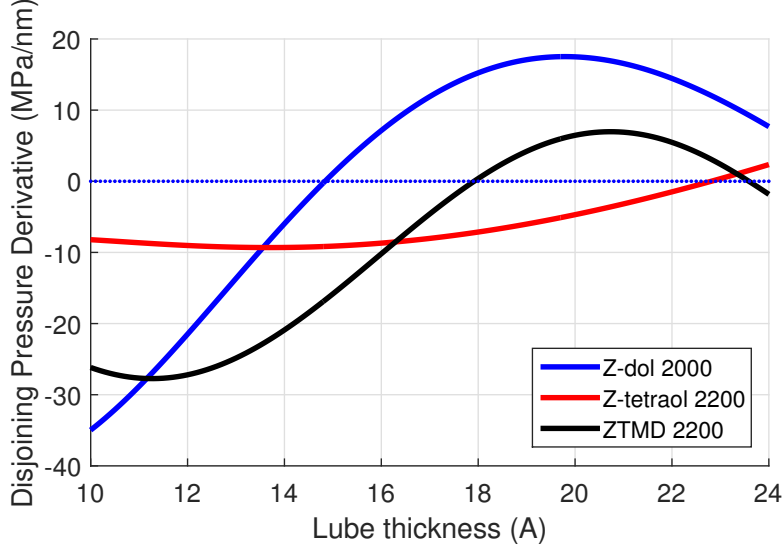
Figure 6.2: Disjoining pressure derivative $d\Pi/dh$ as a function of lubricant thickness h for Z-dol2000 [15], Z-tetraol2200 [34], and ZTMD2200 [13].

for ZTMD. Beyond the critical lubricant thickness, the lubricant becomes unstable and a dewetting phenomenon occurs. Figure 6.2 shows that the disjoining pressure derivative becomes positive, after the critical dewetting thickness causing the lubricant to become unstable [45], and this unstable condition is known in the literature to be closely related to the terracing and layering phenomena [46, 47, 31], due to the polar interaction between the lubricant molecules. As shown in [48, 45] for $d\Pi/dh > 0$, the disjoining pressure transitions from a restoring agent to a force breaking up the lubricant uniform layer into droplets. Reference [45] uses this phenomenon to measure the polar disjoining pressure for PFPE lubricants near the dewetting state. In that work, the curvature of the lubricant droplets are measured as a function of their heights. This can lead to an estimation of the Laplace pressure from which the disjoining pressure can be deduced. Here, we investigate the effect of lubricant dewetting, and show that as lubricant approaches the critical thickness of $d\Pi/dh = 0$, it loses the ability to recover.

6.1.3   Laplace Pressure

Laplace pressure, as introduced in Eq. 4.3, exists due to the inter-molecular forces between the lubricant molecules, and it is proportional to the surface curvature in the lubricant. It has the form $p_{Lap} = \gamma \nabla^2 h$ for a thin-film subjected to the lubrication assumptions. Here, h is the lubricant local thickness, and γ is the surface tension, as a function of temperature. This equation suggests that the Laplace pressure becomes less important compared to the disjoining pressure, as the laser spot size increases. The reason is that the Laplace pressure is roughly proportional to L^{-2}, while the disjoining pressure gradient is roughly proportional to L^{-1}, where L is the characteristic length of the depletion, equal to the laser spot size in the case of HAMR. Therefore, Laplace pressure becomes negligible as the laser spot size becomes

larger. For example, for Z-tetraol 2200 with $1.0nm$ film thickness, our simulations show that the ratio of the disjoining pressure gradient to the Laplace pressure gradient is $F_\Pi/F_L = 2.7$ for a laser spot size of $L = 20nm$, $F_\Pi/F_L = 49$ for $L = 100nm$, and $F_\Pi/F_L = 3500$ for $L = 1\mu m$.

Our calculations show that the effect of Laplace pressure is negligible for most cases of this study, except when the lubricant thickness is close to the dewetting point of the lubricant. In this case, the disjoining pressure derivative approaches zero and the effect of the Laplace pressure on reflow becomes more pronounced.

Reference [15] studied the effect of the lubricant thickness on the significance of the Laplace pressure for Z-dol during the HAMR writing process. They showed that as the lubricant thickness increases, the Laplace pressure becomes more important, e.g. for a case of 1.2nm film thickness, they report the ratio between the disjoining pressure gradient to the Laplace pressure gradient is around $F_\Pi/F_L = 4.1$ meaning that the Laplace pressure is negligible and disjoining pressure is dominant. For the case of $1.4nm$ however, this ratio decreases to $F_\Pi/F_L = 0.76$ meaning that the Laplace pressure is as important as the disjoining pressure. Figure 6.2 explains this observation. For Z-dol 2000, this figure shows that increasing the lubricant thickness from $1.0nm$ to $1.4nm$ decreases the absolute value of the disjoining pressure derivative significantly. Especially, at the critical dewetting thickness of $1.5nm$ the disjoining pressure derivative is $d\Pi/dh = 0$. This explains why the Laplace pressure becomes more important with increase in lubricant thickness for Z-dol 2000. We found the same trend for Z-tetraol and ZTMD. Our simulations show that the Laplace pressure has a minor effect on the recovery process for these lubricants, but for the thicknesses close to the dewetting region it becomes more important.

Keeping the Laplace pressure in the numerical analysis slows down the simulations significantly, by a factor of 10 or more. Therefore it can often be neglected with a significant benefit for the calculations. However, it is sometimes necessary to keep the Laplace pressure in the numerical solution, since it protects the numerical analysis against unwanted numerical instabilities. This is because the Laplace pressure gradient is proportional to the surface curvature, and accordingly, it is highly sensitive to the numerical noises with small wavelengths of the order of the numerical grid spacing $\Delta x, \Delta y$.

6.2 Timescale and Dimensional Analysis

In the previous section we showed that the main driving force for the recovery is the disjoining pressure gradient since the Laplace pressure is negligible in comparison to it. This simplification allows us to carry out an order of magnitude analysis to find the proper time-scale for the recovery problem, assuming the disjoining pressure is the main recovery force.

We can substitute the disjoining pressure for the pressure term into the governing equation, apply the chain rule (Eq. 4.10) for disjoining pressure and obtain the following equation:

$$\frac{\partial h}{\partial t} + \frac{\partial}{\partial x}\left[-\frac{h^3}{3\eta}\Pi'\frac{\partial h}{\partial x}\right] + \frac{\partial}{\partial y}\left[-\frac{h^3}{3\eta}\Pi'\frac{\partial h}{\partial y}\right] = 0. \tag{6.1}$$

Assuming that the recovery time has a timescale of t_s, x and y have the length-scale L, h

has a scale equal to the initial lubricant thickness of h_0, and the values of Π' and η have the scales $\Pi'_0 = \Pi'(h_0)$ and $\eta_0 = \eta(h_0)$ we can balance the terms in the above equation as:

$$\frac{h_0}{t_s} = \frac{1}{L}\frac{h_0^3}{3\eta_0}\Pi'_0\frac{h_0}{L},\tag{6.2}$$

and find the timescale of the problem:

$$t_s = \frac{3L^2\eta_0}{h_0^3\Pi'_0} = \frac{L^2}{D(h_0)},\tag{6.3}$$

where $D(h_0)$ is the nominal value of the diffusion coefficient $D(h)$ defined by Eq. 3.21. So, we can calculate the recovery timescale t_s in terms of the disjoining pressure derivative Π'_0 and viscosity η_0, or in terms of the diffusion coefficient $D(h_0)$.

Equation 6.3 suggests that the timescale of the recovery is proportional to the length scale squared $t_s \propto L^2$, due to the diffusive nature of the governing equation. This means that smaller laser spots should recover much faster than larger ones. Additionally, as the viscosity η_0 increases, the recovery time becomes longer. In other words, the lubricant becomes less mobile and needs more time to recover. Finally, this equation highlights the importance of the disjoining pressure. If the disjoining pressure derivative Π'_0 becomes zero or approaches zero, the lubricant recovery timescale t_s becomes very large. In other words, a lubricant with a film thickness close to the critical dewetting thickness never recovers.

6.3   Effect of Hydroxyl End-groups on Recovery Time

Figure 6.3 shows a typical reflow process, close to the HAMR conditions, for an initial film thickness of $h_0 = 1.2nm$, a laser spot size of $L = 20nm$ for Z-dol 2000 (Fig. 6.3a), Z-tetraol 2200 (Fig. 6.3b), and ZTMD (Fig. 6.3c). This figure not only shows the difference in depletion for the studied lubricants under typical HAMR conditions, but also draws a clear comparison of the recovery time between these lubricants. According to this figure, after the laser exposure ends, Z-dol recovers in $10\mu s$, Z-tetraol in $700\mu s$ and ZTMD in $1.5ms$. This suggests the recovery time is significantly longer for Z-tetraol compared to Z-dol, but the difference between Z-tetraol and ZTMD is not as significant. In the following sections, we present the results of the reflow simulations in more details and discuss the effects of the functional end-groups on the recovery time for various film thicknesses and laser spot sizes.

Reference [16] showed that the Z-dol 2000 irradiated by a laser spot size of $L < 100nm$ reflows to within $0.01nm$ depletion in less than $1ms$. This means that after one disk revolution, the lubricant is fully recovered, and the depletion is not distinguishable by the OSA. However, this is not the case for lubricants with a higher number of hydroxyl end-groups.

Figure 6.4 shows that the recovery time for ZTMD is a few milliseconds, even for the laser spot sizes as small as $L = 20nm$. Additionally, It suggests that in the case of $L = 100nm$, the recovery times for Z-tetraol and ZTMD are significantly longer, around tens of milliseconds, meaning that these lubricants cannot recover completely before the next laser exposure. This finding agrees with the Ref. [23] recent study for the recovery time of Z-tetraol in which the diffusion coefficient for Z-tetraol was measured, and the reflow simulations were
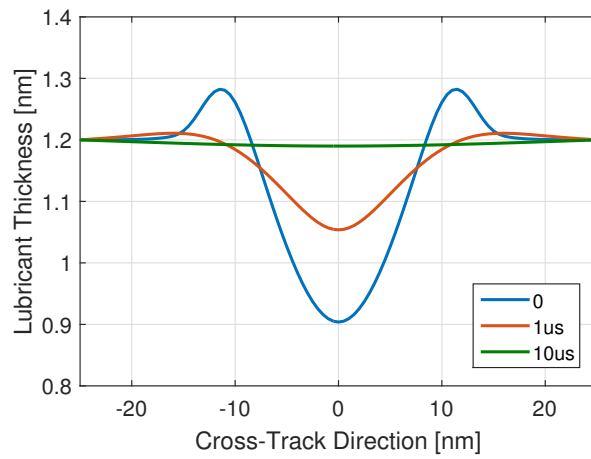
(a) Z-dol 2000
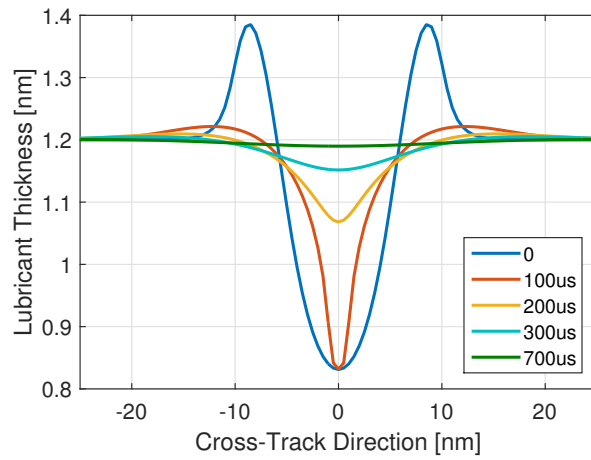
(b) Z-tetraol 2200
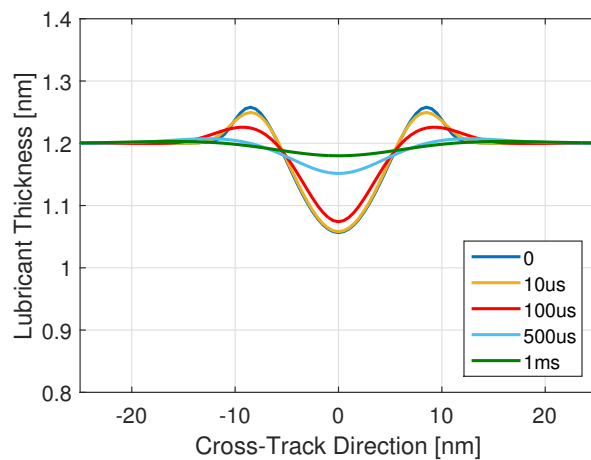
(c) ZTMD

Figure 6.3: The cross-track view of a reflow process for three types of lubricants in time for the case of laser spot-size $L = 20nm$ and initial lubricant thickness $h_0 = 1.2nm$

performed using those measurement results. It was found that in some cases, the trough is still detectable after 1000ms of recovery.

As discussed earlier, evaporation makes a significant contribution to the depletion for Z-dol, but it is negligible for Z-tetraol and ZTMD. This is because the absolute value of the disjoining pressure $\Pi(h)$, and activation evaporation energy ΔE_{vap} and entropy ΔS_{vap} are higher for Z-tetraol and ZTMD compared to Z-dol, due to the stronger bonding to the disk [41]. This improvement in the evaporation properties is an apparent advantage of adding extra hydroxyl end-groups to the lubricant. However, our results (Fig. 6.4 and 6.5) show that the increase in hydroxyl-end groups from 2 (Z-dol) to 4 (Z-tetraol) can increase the recovery time significantly, by a factor of 100 or more. This significant increase in the recovery time is due to the large increase in the viscosity of Z-tetraol compared to Z-dol. On the other hand, the increase in the number of hydroxyl end-groups from 4 (Z-tetraol) to 8 (ZTMD) decreases the amount of depletion significantly (Fig. 5.8), but it increases the recovery time by a factor of 2 only, which is not as severe as the previous step between Z-dol and Z-tetraol. This is because the extra 4 hydroxyl end-groups are added to the middle chain for ZTMD. This addition not only increases the disjoining pressure and viscosity, but also improves the disjoining pressure derivative properties for ZTMD (in contrast to the trade-off between evaporation and disjoining pressure properties for the conventional lubricants).

Figure 6.2 shows for a lubricant thickness of $h = 1.2nm$ the absolute value of the disjoining pressure derivative is $\Pi' = 28Mpa/nm$ for ZTMD and $9Mpa/nm$ for Z-tetraol, a factor of 3 difference. Considering the significant role that $d\Pi/dh$ plays as the main source of recovery, this larger $d\Pi/dh$ value for ZTMD explains why its recovery process is not as slow as expected from the viscosity curve (Fig. 6.1). This is a great advantage of a multi-dentate lubricant like ZTMD over a conventional one like Z-tetraol. Reference [49] conducted early measurements on ZTMD and reported that the superiority of a multi-dentate lubricant over its conventional counterpart is its ability to achieve higher molecular weights and the shorter free chain lengths at the same time, improving the evaporation and film stiffness properties simultaneously.
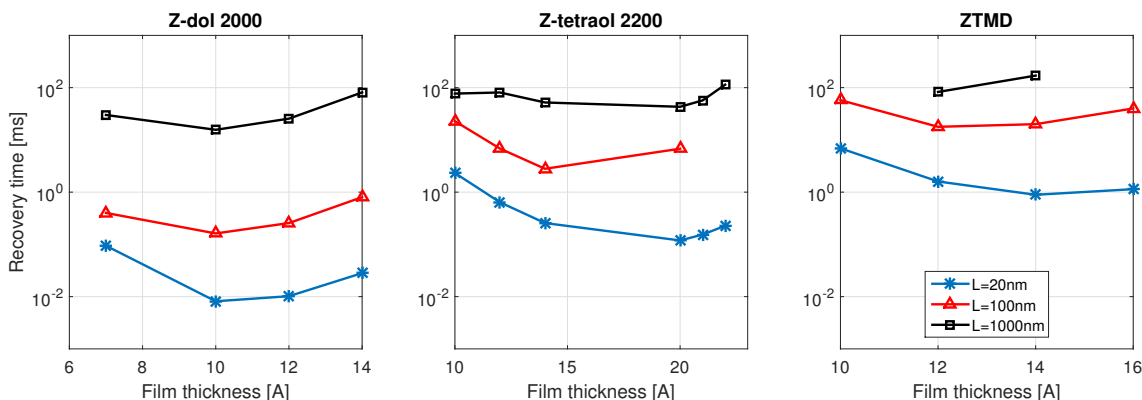
Figure 6.4: The recovery time as a function of the initial film thickness for different lubricant types, and different laser spot sizes of $L = 20nm, 100nm, 1\mu m$

6.4 Optimum Film thickness for Reflow Process

Figure 6.4 shows the recovery time as a function of the lubricant thickness, for Z-dol 2000, Z-tetraol 2200 and ZTMD, and for three laser spot sizes of $L = 20nm, 100nm, 1.0\mu m$. It shows for Z-dol 2000 that the increase in the lubricant thickness from $0.7nm$ to $1.4nm$ first decreases the recovery time, but after reaching an optimal recovery time thickness of around $h_0 = 1.0nm$, the recovery time increases as the thickness increases. This trend can be seen for all laser spot sizes for Z-dol 2000. Z-tetraol and ZTMD exhibit similar behaviors with different optimum points. This means that for all the studied lubricant types, there is an optimal thickness for recovery time. For Z-tetraol, the recovery time decreases by increasing the lubricant thickness from $1.0nm$ to around $2.0nm$, and after passing this point, the recovery time increases until it reaches the $2.2nm$ film thickness, close to the dewetting point for Z-tetraol where $d\Pi/dh \approx 0$. For ZTMD, Fig. 6.4 shows that the optimum point of interest occurs around $1.4nm$.

6.5 Effect of Laser Spot Size on Recovery Time

Reference [16] showed that Z-dol 2000 recovers faster for the smaller laser spots. Figure 6.5 presents the results of reflow simulations for Z-tetraol 2200 and ZTMD along with the results for Z-dol 2000, where the recovery time is plotted as a function of the the laser spot size L, for three different lubricants with three initial film thicknesses of $h_0 = 1.0, 1.2, 1.4nm$. This figure shows that, for all three different types of lubricants, the recovery time increases as the the laser spot size increases, however, the rate of increase varies for the different lubricants. In Eq. 6.3, we showed that the recovery timescale is proportional to the length-scale squared,
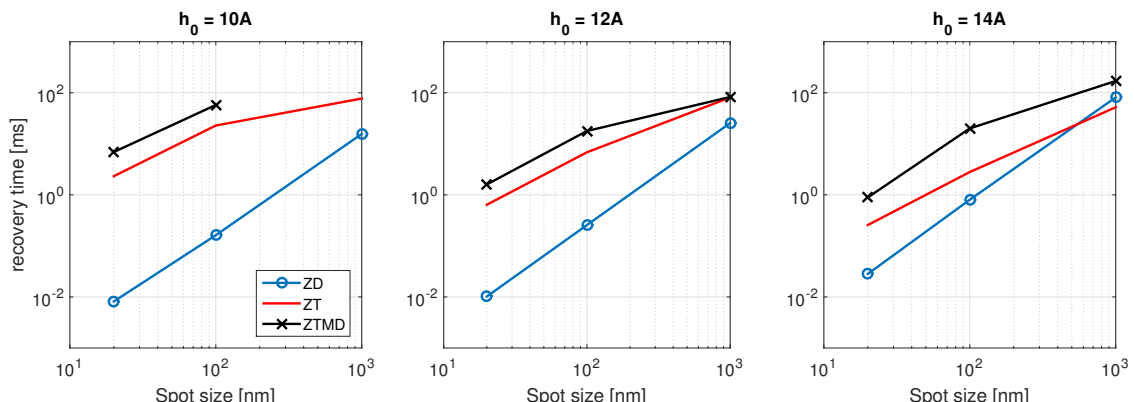
Figure 6.5: The recovery time as a function of the laser spot size for different lubricants different initial film thicknesses of $h_0 = 1.0, 1.2, 1.4nm$

$t_r \propto L^2$. Figure 6.5 shows that Z-dol follows this trend for the three different film thicknesses of $h_0 = 1.0, 1.2, 1.4nm$. For Z-tetraol and ZTMD however, the trend is different since the curves for Z-tetraol and ZTMD can be modeled as $t_r \propto L^m$ with $m < 2$. The parameter m decreases even more as the laser spot size increases to $L = 1\mu m$.

The reflow time depends on the depletion depth, meaning that less depletion needs less time to recover. Figure 5.8 shows the depletion depth as a function of the film thickness

for different laser spot sizes and lubricants. As discussed earlier, this figure shows that Z-tetraol and ZTMD have different depletion behaviors than Z-dol. For a film thickness range of $1.0nm < h_0 < 1.4nm$, Fig. 5.8 shows that the depletion is almost constant for Z-dol for different laser spot sizes. On the other hand, it shows for Z-tetraol and ZTMD that the depletion depth decreases significantly with the laser spot size, to the point that the depletion depth for a laser spot size of $L = 1\mu m$ for ZTMD is very small, close to $0.01nm$ the resolution of OSA, meaning that the lubricant is almost undepleted. This explains why the recovery time in Fig. 6.5 doesn't follow the trend of $t_r \propto L^2$ for Z-tetraol and ZTMD, since they deplete much less than Z-dol and need less time to recover.

6.6 Discussion

For Z-dol 2000, Ref. [16] showed that a spot generated by a HAMR laser irradiation with a beam size smaller than 100nm, recovers to within $0.01nm$ trough depth in less than 1ms. Our results show that the recovery times for lubricants with higher numbers of hydroxyl end-groups are much longer. In fact, the recovery times of Z-tetraol and ZTMD can be a few milliseconds, especially close to the target lubricant and laser dimensions of HAMR, around $h_0 = 1.0nm$ film thickness, and $L = 20nm$ laser spot size. The main reasons are the extra functional end-groups for these lubricants, which lead to stronger bonding to the disk, as well as a significant increase in the viscosity, and a decrease in mobility. These findings suggest that the lubricant recovery is not fast enough for Z-tetraol and ZTMD to reach a uniform thickness before the next disk revolution. Due to this slow reflow process, the depletion can grow significantly, if the lubricant is subjected to a repetition of the laser irradiation.

Reference [23], based on experimental measurements of the diffusion coefficient, suggests that a trough width of $L = 50nm$ in a $1.0nm$ thick Z-tetraol 2200 should recover in about 1000ms. However, Fig. 6.5 suggests that this number should be around 10-50ms for the mentioned conditions. Reference [50] suggests that a Z-tetraol lubricant with a $h_0 = 0.95nm$ initial film thickness and a trough size of $L = 25\mu m$ recovers after almost 22 minutes. The recovery time reported by these experiments are much longer than the predicted values in this study for the following reasons.

First, the $25\mu m$ spot size used in [50] is much larger than the target of HAMR. As discussed earlier, the larger spots recover much slower ($t_r \propto L^2$), and therefore, for those experiments we expect a much longer recovery time as well. Second, the experiments mentioned above measured the recovery time for a continuous laser track depletion rather than a single spot depletion. For our simulation case of a single spot, reflow occurs from all directions, leading to a 2-dimensional diffusion process. However, for experiments for a depleted track by Ref. [50], the reflow occurs only from the sides of the track leading to a much longer recovery time, a 1-dimensional diffusion process. Reference [23] also models the lubricant by a 1-D flow and shows that the multiple depleted tracks side by side increase the recovery time because the tracks coalesce and form a larger trough with a far slower recovery rate. Finally, the effect of the repetition can be another significant effect on the recovery time as experimented by Ref. [50] and modeled by Ref. [24].

For a Z-tetraol film Ref. [51] reports that a depleted track with an initial thickness of $h_0 = 1.2nm$ and a track width of $L = 25\mu m$ takes 5 hours to recover. However, Ref.

[50] shows that under almost similar conditions ($h_0 = 0.95nm$), the recovery time is much shorter, around 22 minutes.

We developed a 1-D Finite Volume code to solve for a track reflow, using the material properties introduced earlier in Chapter 4 and the initial lubricant profiles from Ref. [51]. Our track-reflow solver predicts a much shorter recovery time of 17 minutes for Z-tetraol, close to the 22 minutes reported by Ref. [50]. Reference [23] measured the diffusion coefficient (Eq. 6.3) as a function of lubricant thickness for Z-tetraol 2200 and showed that his measurements match the calculated values by Ref. [52]. Using the reflow measurements by Ref. [50], one can also calculate the diffusion coefficient for Z-tetraol, and it turns out to be very close to what Ref. [52] predicts and Ref. [23] measures. However, the recovery time reported by Ref. [51] seems to be much longer than other studies, meaning that they measure a much smaller value for diffusion coefficient. In other words, the material properties obtained by Ref. [51] are much different than the ones used here in this paper, as well as in the works of Refs. [52], [23], and [50]. The reason could be that Ref. [51] only measured a single case for recovery, whereas the other papers captured a more comprehensive set of measurements for different lubricant thicknesses and different time intervals. For ZTMD, no measurements of diffusion coefficient or recovery time are published to date, and this work is the first attempt to model the recovery behavior of this multi-dentate lubricant under HAMR conditions.

In Fig. 6.4, the recovery time t_r is plotted as a function of the initial film thickness for three different types of lubricants. An optimal film thickness for the recovery is observed for all three lubricants. This optimal point is around 1.0nm for Z-dol, 1.8nm to 2.0nm for Z-tetraol, and 1.4nm for ZTMD (Fig. 6.4). On one hand, the viscosity grows and recovery speed decreases significantly as the film thickness decreases. On the other hand, the disjoining pressure derivative, the driving force for recovery, decreases as the film thickness increases and approaches the critical dewetting thickness of the lubricant, leading to a significant decrease in the recovery speed. These two effects together produce the optimal thickness with the fastest recovery speed. The mentioned viscosity and disjoining pressure effects depend on the lube-disk bonding and the polar properties of the lubricant. We also investigated the effect of the dewetting on the recovery speed after HAMR conditions.

The recovery simulations presented here is a useful tool to engineer the next generation of lubricants for HAMR, since it can connect the lubricant characterization studies to the HAMR reflow prediction. Upon using an accurate lubricant characterization, this tool can obtain a good prediction of the lubricant recovery, and on the other hand, it can verify the lubricant characterization results of the former studies using the experimental results from the depletion and recovery measurements. This tool can also estimate the reflow time for small laser spot sizes close to the target for HAMR, to be verified by future experiments.

Chapter 7

Material Viscoelasticity

The earlier part of this dissertation (Chapters 3-6) as well as numerous works in the literature have investigated the HDD lubricant behavior, both experimentally and numerically, while assuming the lubricant to be a purely viscous material [15, 16, 41, 19, 21].

However, experiments show that HDD lubricants behave similar to linear viscoelastic multi-stage generalized Maxwell fluids, e.g. 3-stage in case of Z-tetraol 2000 (Fig. 7.1) [12, 53]. The constitutive relation between the stress and strain for a general linear viscoelastic material can be described as [54]:

$$\boldsymbol{\sigma} = -p\boldsymbol{I} + \int_0^t 2G(t-\tau)\frac{d\boldsymbol{e}}{d\tau}d\tau, \tag{7.1}$$

where $\boldsymbol{\sigma}$ is the stress tensor, p is the pressure, $\boldsymbol{e}(\tau)$ is the deviatoric strain tensor, $G(t)$ is the time-dependent shear modulus, and the integral updates the stress tensor in time, taking into account the deformation history of the material.

The shear modulus $G(t)$ is a function of time t and depends on the viscoelastic model describing the material behavior as well as the specific choice of material.

The most basic model for a linear viscoelastic fluid is the Maxwell model which includes a spring and a dashpot, representing the material elasticity and viscosity, respectively. In a more complex model, a number of spring-dashpot units can be paralleled together to form a multi-stage Maxwell fluid analog (Fig. 7.1). The shear modulus $G(t)$ for a multi-stage Maxwell fluid has the following form:

$$G(t) = \sum_{i=1}^{n} G_i \exp\left(-t/\lambda_i\right), \tag{7.2}$$

where n is the number of stages (Fig. 7.1). For each stage, λ_i is the Maxwell relaxation time, and G_i is the shear rigidity. $G(t)$ represents the stress response of the material to a unit-step displacement, and varies for different material models. Reference [12] reports that a single-stage model suffices to describe the shear modulus $G(t)$ for Z-dol 2500, and a 3-stage model is the best fit for $G(t)$ for Z-tetraol 2000. The measurements for λ_i and G_i show that for multi-stage models, normally one of the stages is dominant. Since this study is the first attempt to model the viscoelastic behavior of PFPE lubricants under HAMR conditions, we
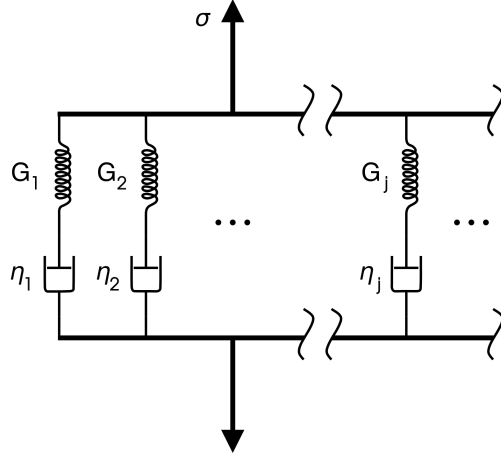
Figure 7.1: Spring-Dashpot analog for the linear viscoelastic multi-stage generalized Maxwell fluids

only consider the dominant stage and reduce the Ref. [12] model to a single-stage one, with the following expression for the shear modulus:

$$G(t) = G_0 \exp\left(-t/\lambda\right), \tag{7.3}$$

where G_0 and λ are the shear rigidity and the Maxwell relaxation time of the dominant stage. In future studies, the effect of the non-dominant stages can be considered as well. Table 7.1 shows the Maxwell relaxation time, λ for Z-dol, and Z-tetraol for the temperature of $T = 25^o C$.

For Maxwell fluids, the essential relation between the viscoelastic parameters (G_0, λ) and viscosity η can be expressed as:

$$\eta = G_0 \lambda. \tag{7.4}$$

This equation is important since it connects the viscoelastic parameters, G_0 and λ, to the lubricant viscosity η which is very well studied for PFPE lubricants. As discussed earlier in Section 4.3, numerous experiments have investigated the temperature and thin-film effects on the lubricant viscosity, using techniques such as spin-off [37], blow-off, and diffusion studies [18]. So, the knowledge about the lubricant viscosity helps us understand the effects of temperature and material confinement on the viscoelastic parameters as discussed in the following sections.

7.1 Maxwell Relaxation Time

Maxwell relaxation time λ describes the viscoelastic behavior of the Maxwell fluids, since it appears in the exponential of Eq. 7.3. Based on the value of the Maxwell relaxation time, this equation can represent three different behaviors for the material.

First, at the limit of small Maxwell relaxation time when $\lambda \to 0$ (compared to the timescale of the problem), the shear modulus $G(t)$ in Eq. 7.3 approaches the expression $G(t) = G_0 \lambda \delta(t)$. Substituting this into the constitutive equation (Eq. 7.1) we get

$$\boldsymbol{\sigma} = -p\boldsymbol{I} + 2G_0 \lambda \frac{d}{dt} \boldsymbol{e}(t), \tag{7.5}$$

which represents the constitutive equation for a Newtonian incompressible viscous fluid because the term $G_0\lambda$ can be interchanged with the viscosity η (Eq. 7.4).

Second, at the limit of large Maxwell relaxation time when $\lambda \to \infty$, the exponential in Eq. 7.3 approaches unity, and the shear modulus simplifies to $G(t) = G_0$. Substitution of this into the constitutive equation (Eq. 7.1) gives

$$\boldsymbol{\sigma} = -p\boldsymbol{I} + 2G_0 \boldsymbol{e}(t). \tag{7.6}$$

This equation restores the constitutive equation for an incompressible linear elastic solid.

Finally when none of the extremes $\lambda \to 0$ or $\lambda \to \infty$ occur, and the Maxwell relaxation time λ and HAMR timescale t_s have the same order of magnitude, the material behaves like a viscoelastic fluid, and the original form of the constitutive equation (Eq. 7.1) cannot be simplified. The two extreme limits for λ show the significant effect of this parameter on the lubricant behavior.

7.2 Viscoelastic Measurements

Under HAMR conditions, the material experiences a variation of temperatures from the room temperature of $T_\infty = 25^o C$ to a HAMR peak temperature of $T_p = 350^o C$. Additionally, experiments show that the Maxwell relaxation time λ is very sensitive to the temperature [12]. Therefore, it is necessary to include the effect of temperature on the Maxwell relaxation time, based on the experimental data.

For each lubricant, the Maxwell relaxation time $\lambda(T)$ can be expressed as a function of temperature:

$$\lambda(T) = \tau_0 a_{T_0}(T) \tag{7.7}$$

where τ_0 is the relaxation time at the reference (or glass) temperature T_0, and $a_{T_0}(T)$ is the time-temperature shift function from the glass temperature to the current temperature. $\lambda(T)$ and $a_{T_0}(T)$ are decreasing functions of temperature, and for temperatures $T_0 < T$ the shift function $a_{T_0}(T) < 1$.

Depending on the temperature range and lubricant type, a specific shift function describes the relation between the Maxwell relaxation time and temperature. For the PFPE lubricants a Williams-Landel-Ferry (WLF) model [55] is used for the shift function:

$$\log a_{T_0} = -\frac{C_1(T - T_0)}{C_2 + (T - T_0)}, \tag{7.8}$$

where T_0 is the reference (glass) temperature, C_1 and C_2 are the WLF coefficients correspond-

ing to T_0. Based on the values for τ_0, T_0, C_1, C_2, the relaxation time λ can be calculated for every temperature.

Reference [56] investigated the effect of molecular weight on the glass temperature and WLF coefficients for the Fomblin Y and Z family of HDD lubricants. Reference [12] performed oscillatory shear and creep tests for a multitude of lubricants and measured the Maxwell relaxation time λ for different temperatures. Accordingly, he calculated the WLF coefficients for each lubricant, using a nonlinear regression analysis, the results of which are consistent with those for nonpolar PFPEs Y and Z reported by Ref. [56]. These result are summarized in Table 7.1 for Z-dol 2500 and Z-tetraol 2000.

Table 7.1: WLF coefficients (T_0, C_1, C_2) and Maxwell relaxation time at the glass temperature T_0 and room temperature, for Z-dol 2500 and and Z-tetraol 2000

Lubricant	Z-dol 2500	Z-tetraol 2000
T_0	-113.6^oC	-112.2^oC
C_1	13.62	23.22
C_2	59.72	45.81
τ_0	$5.03 \times 10^4 s$	$4.02 \times 10^{13} s$
λ at $T = 25^oC$	$1.5 \times 10^{-5} s$	$1.6 \times 10^{-4} s$

For each temperature, the Maxwell relaxation time $\lambda(T)$ is calculated by Eqs. 7.7 and 7.8 and the parameters listed in Table 7.1. Accordingly, Fig. 7.2 shows the calculated Maxwell relaxation times $\lambda(T)$ for a temperature range of $T_\infty = 25^oC$ to $T_p = 350^oC$ for Z-dol 2500 and Z-tetraol 2000.
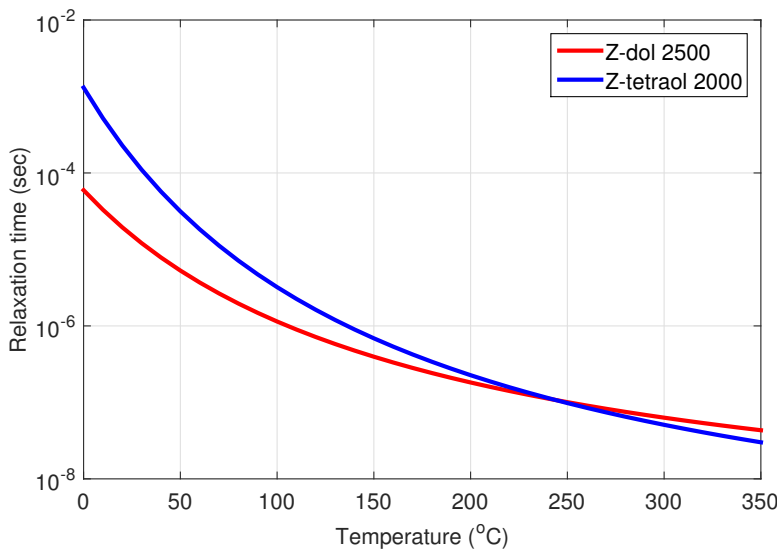
Figure 7.2: Maxwell relaxation time as a function of temperature for Z-dol 2500 and Z-tetraol 2000

This figure shows that the Maxwell relaxation time λ is larger for Z-tetraol compared to Z-dol, for a large range of temperatures. This suggests that as the number of hydroxyl functional end-groups increases in the lubricant molecular structure, the lubricant behaves more elastically, since it becomes more bonded to the disk. For example, Ref. [12] reports the Maxwell relaxation time for a non-polar lubricant like Z03 to be around $3\mu s$, for Z-dol 2500 with 2 hydroxyl groups around $4\mu s$, and for Z-tetraol 2000 with 4 hydroxyl groups around $20\mu s$. (Fig. 22.7a from [12])

As discussed in Section 4.3, Ref. [12] applied Eyring's rate theory [57] to HDD lubricants and characterized the viscosity $\eta(T, h)$ as a function of lubricant thickness h and temperature T. This calculation suggests that viscosity decreases significantly with temperature, similar to the relation between Maxwell relaxation time $\lambda(T)$ and temperature T (Fig. 7.2). Furthermore, Ref. [12] reports that the effects of temperature on the Maxwell relaxation time $\lambda(T)$ and viscosity $\eta(T)$ are similar, and viscosity $\eta(T)$ can be calculated in terms of a shift function as $\eta(T) = \eta(T_0)a_{T_0}(T)$, which is similar to Eq. 7.7. Accordingly, we assume that the shear rigidity G_0 does not depend on temperature, since $G_0 = \eta/\lambda$ (Eq. 7.4), and both η and λ vary by the same rate with temperature.

7.3   Thin-film Viscoelastic Effects

The measurements discussed earlier have studied some of the rheological properties of PFPEs for bulk material. However, the effect of material confinement can be significant on the parameters such as viscosity η, shear rigidity G_0, and Maxwell relaxation time λ. Each of these can be a function of both temperature T and film thickness h for ultra-thin films of lubricants covering the disk.

Former studies have investigated the effect of the film thickness h on the viscosity η [37, 15]. However, no quantitative measurement is found in the literature to investigate the effect of material confinement on the Maxwell relaxation time λ for the PFPE lubricants. Some qualitative measurements are done in Ref. [53] on thin films of Z-dol and Z03, using a fiber wobbling method. These measurements report that the relaxation time λ increases and the lubricant behaves more elastic as the film thickness decreases.

Since no accurate quantitative data is provided in the literature about the effect of material confinement on the Maxwell relaxation time, here we use the values measured for bulk material in Ref. [12], given in Table 7.1. Accordingly, we assume that the Maxwell relaxation time is only a function of temperature ($\lambda = \lambda(T)$), and the shear rigidity is only a function of the film thickness ($G_0 = G_0(h)$), while viscosity is a function of both temperature and film thickness ($\eta(h, T) = G_0(h)\lambda(T)$). We should also keep in mind that the thin-film lubricants behave more elastic compared to the bulk counterpart, according to the qualitative measurements.

Chapter 8

Theory of Viscoelasticity for HAMR Lubricants

The lubricant is in the form of a thin layer that is bonded to the disk as a substrate. One could model the lubricant behavior under HAMR conditions either of two ways: by modeling a fixed laser and mobile disk-lubricant substrate, or else by modeling a fixed disk-lubricant substrate and a mobile laser. We choose the second alternative and fix the disk and the lubricant and move the laser down the track. The difference is the centripetal acceleration force on the lubricant due to disk rotation, which in our case can be shown to be negligible. We model the laser by prescribing a Gaussian temperature distribution (Eq. 2.1) on the disk and lubricant, which has an ambient temperature of $T_\infty = 25^oC$, a peak temperature of $T_p = 350^oC$, and a Full-Width Half-Maximum (FWHM) of $L = 20$nm. The laser spot scans the track with the speed $U = 5m/s$, and the lubricant has an initial film thickness of $h_0 = 1nm$.

We apply a no slip boundary condition on the bottom of the lubricant layer where it is bonded to the fixed disk. We also assume that the lubricant thickness far from the laser has a uniform value of h_0. We model the boundary conditions on top of the lubricant with the thermo-capillary shear stress and the disjoining pressure. Thermo-capillary shear stress is the driving force for the lubricant depletion, and it exists due to the non-uniform temperature, followed by non-uniform surface tension on the lubricant free surface. Accordingly, the thermo-capillary shear stress has the form $\boldsymbol{\tau} = \boldsymbol{\nabla}\gamma$ where γ is the surface tension, as discussed in the Section 4.1.

Here, the shear rigidity $G_0(h)$ is only a function of lubricant thickness, Maxwell relaxation time $\lambda(T)$ is a function of temperature, and viscosity $\lambda(T, h)$, a function of both local temperature and lubricant thickness. So, each of these parameters can vary in time and along the lubricant film (x, y, t) and are assumed to be uniform across the film since the lubricant layer is very thin.

8.1 Disjoining pressure

First introduced by Derjaguin [30], disjoining pressure is defined as an equivalent pressure exerted on the lubricant surface representing the intermolecular forces between lubricant

molecules and surrounding lubricant, disk, and gas molecules . The disjoining pressure model for HDD lubricants including Z-dol, Z-tetraol, and ZTMD families of PFPE lubricants is discussed earlier in Section 4.2. When the lubricant thickness becomes non-uniform, the disjoining pressure gradient in the lubricant drives a Poiseuille flow leading the lubricant to recover. Thus disjoining pressure can be considered as the main force for the lubricant recovery and resistance against disturbances [36]. In Chapter 6, we showed that as $d\Pi/dh$ decreases the lubricant reflow takes longer, and if $d\Pi/dh = 0$ the lubricant ceases to recover [58]. Disjoining pressure has two components: polar Π_p and dispersive Π_d. The polar component of disjoining pressure is due to the polar interactions of the lubricant end-groups with one another and with the Carbon Over-Coat (COC) molecules. The dispersive component of disjoining pressure is due to the Van der Waals force interaction of the molecules. The lubricant thickness in this study is around $h_0 = 1nm$, far from the dewetting thickness for Z-tetraol 2000, around $h = 2.3nm$ where the polar interactions are important [34]. Therefore, it is reasonable to simplify the analysis by neglecting the polar component of disjoining pressure. Accordingly, we only include the dispersive part of the disjoining pressure, which can be written in the form of:

$$\Pi(h) = \frac{A}{h^3}, \tag{8.1}$$

where $\Pi(h)$ is the disjoining pressure, A is the Hamaker constant, and h is the lubricant local thickness. The Hamaker constant is chosen as $A = 2.6 \times 10^{-21} J$ based on the surface energy measurements by Ref. [33].

8.2 Depletion Timescale

Reference [15] studied Z-dol 2000 under HAMR conditions, using a viscous model, and suggested that the timescale of the lubricant depletion has the following form:

$$t_{s1} = 2\frac{\eta_0 L^2}{h_0 c \Delta T},$$

where η_0 is the nominal viscosity of the thin-film, calculated at the ambient temperature T_∞ and initial lubricant thickness h_0. L is the laser spot size, U is the disk speed (or laser speed in our case), $c = d\gamma/dT$ is the slope of the surface tension-temperature curve, and ΔT is the difference between the HAMR peak T_p and ambient T_∞ temperatures.

An alternative possibility for the timescale of the problem is the simple choice of

$$t_{s2} = \frac{L}{U},$$

where L is the laser spot size, and U is the disk speed.

For the target of HAMR, we can assume $\Delta T = 325^oC$, disk speed $U = 5m/s$, laser spot size $L = 20nm$, viscosity $\eta_0 = 1pa.s$, initial lube thickness $h_0 = 1nm$, and surface tension slope of $c = 0.06mN/m^oC$. Using these typical values, we find the timescales $t_{s1} = 40\mu s$ and $t_{s2} = 4ns$, and these timescales have a 4 order of magnitude difference. The essential
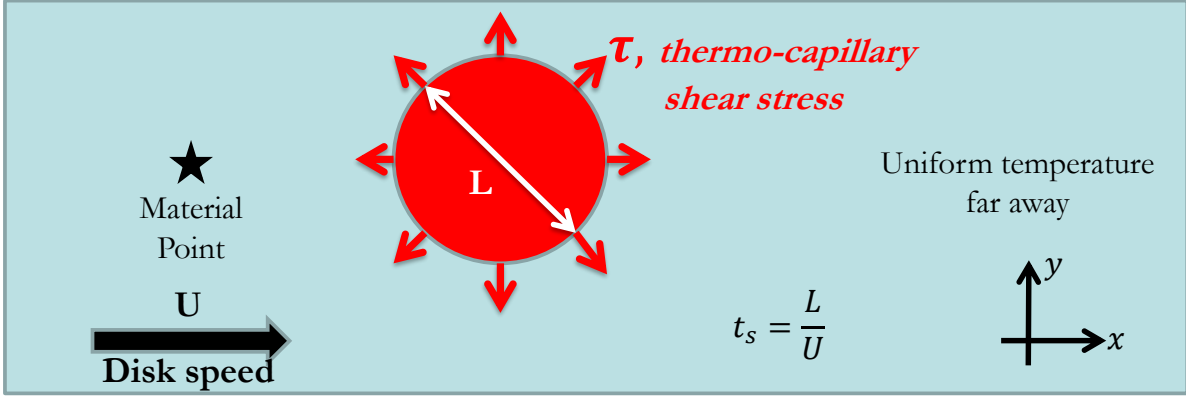
Figure 8.1: The schematic view of the disk under laser irradiation. The laser spot has a length scale L, causing the thermo-capillary shear stress to deplete the lubricant. The temperature in the laser center reaches the HAMR peak temperature, whereas the one far away from the laser is close to the room temperature. The material point travels with the disk speed U and passes through the laser spot.

question is, therefore, which of these timescales is effective to model the lubricant depletion?

The timescale t_{s1} is over which the thermo-capillary shear stress balances the material viscous forces due to the velocity gradient across the lubricant (i.e. $d\gamma/dx \sim \eta dv_x/dz$). The thermo-capillary shear stress $d\gamma/dx$ is proportional to the thermal gradient and is of the order of $c\Delta T/L$. Also, the material viscous forces $\eta dv_x/dz$ are of the order of $\eta_0 v_s/h_0$ where v_s is the velocity scale of the material deformation. By balancing the thermo-capillary shear stress and viscous forces, we find v_s as

$$v_s = \frac{h_0 c \Delta T}{L\eta},$$
(8.2)

and the timescale for trough generation is $t_{s1} = L/v_s$, since the material points move to the outside of the laser spot and this motion has a length scale of L and a timescale of t_{s1}, in the model by Ref. [15]. However, the main assumption in the calculation above is that the material behaves as a viscous material, and the thermo-capillary forcing on the lubricant can be balanced by the viscous terms. This assumption might not be applicable to the case of PFPE lubricants when the viscoelastic effects are included.

As illustrated in Fig. 8.1, consider a material particle away from the laser spot and thermo-capillary effects. This particle travels with the disk speed U on the length scale L and after the corresponding timescale of the travel, L/U, it reaches the middle of the laser spot where the thermo-capillary effects are present. So, the timescale over which the thermo-capillary shear stress changes for the moving material point is $t_{s2} = L/U$. Accordingly, the material also responds to the shear stress, and depletes on the same timescale as the forcing timescale. So, we choose t_{s2} as the effective time scale of the thermo-capillary forcing and lubricant depletion.

8.3 Deborah Number

Originally introduced in [59], the Deborah number is a key parameter in the theory of viscoelasticity, which describes the rheological behavior of the materials. In this section we discuss the significance of the Deborah number for modeling the lubricant under HAMR conditions. Accordingly, we calculate it for Z-tetraol 2000 as a function of the laser spot size. We also include it as a new parameter in our model's governing equation. In the following sections, we discuss how the numerical results of this study agree with the material behavior that the Deborah number predicts.

We discussed above the significant effect of the Maxwell relaxation time λ on the material behavior. Maxwell relaxation time is a dimensional parameter and needs to be compared with the timescale of the problem. Considering the Maxwell relaxation time λ and the chosen timescale of the problem ($t_{s2} = L/U$), we introduce the non-dimensional parameter known in the theory of viscoelasticity as the Deborah number:

$$De = \frac{\lambda}{t_s} = \frac{\lambda U}{L}, \tag{8.3}$$

where $\lambda(T)$ depends on the local temperature, and the choice of the material (Fig. 7.2). So, the Deborah number is a function of the material choice for the lubricant, the HAMR temperature T, disk speed U, and laser spot size L. We call the latter three parameters the HAMR conditions. Fig. 8.2 shows schematically the connection of the Deborah number to each parameter.

In Section 7.1, we discussed the different cases for the magnitude of the Maxwell relaxation time λ and how it can be significantly smaller or larger than, or comparable with, the timescale of the problem. Accordingly, the Deborah number is a good measure to distinguish the different lubricant behaviors under HAMR conditions.

As illustrated in Fig. 8.2, if $De \gg 1$, the forcing and the material flow occur at a much faster rate than the relaxation response, i.e. $\lambda \gg t_s$, and the material behaves predominantly like an elastic solid. Whereas, if $De \ll 1$, the material has sufficient time to relax the stress, $\lambda \ll t_s$, and therefore, it behaves like a viscous fluid. Finally, if $De \approx 1$, and the relaxation time λ and timescale t_s are of the same order of magnitude, then the lubricant behaves like a viscoelastic fluid.

For a typical case of HAMR conditions, we can calculate the Deborah number. Using the material properties given for Z-tetraol 2000 (Table 7.1), and assuming a disk speed of $U = 5m/s$, we find the Deborah number as a function of laser spot size L, for three different HAMR peak temperatures of $T = 350^oC, 500^oC, 650^oC$, plotted in Fig. 8.3.

This figure shows that as the laser spot size decreases and approaches the target of HAMR, the Deborah number grows. For the micron size spots, the material behaves predominantly as a viscous fluid and $De \ll 1$. Around the laser spot size of $L = 200nm$ where $De = 1$, the lubricant's behavior transitions to an intermediary viscoelastic regime. For smaller laser spot sizes like $L = 20nm$, the Deborah number increases significantly, and the material behavior approaches the elastic limit.
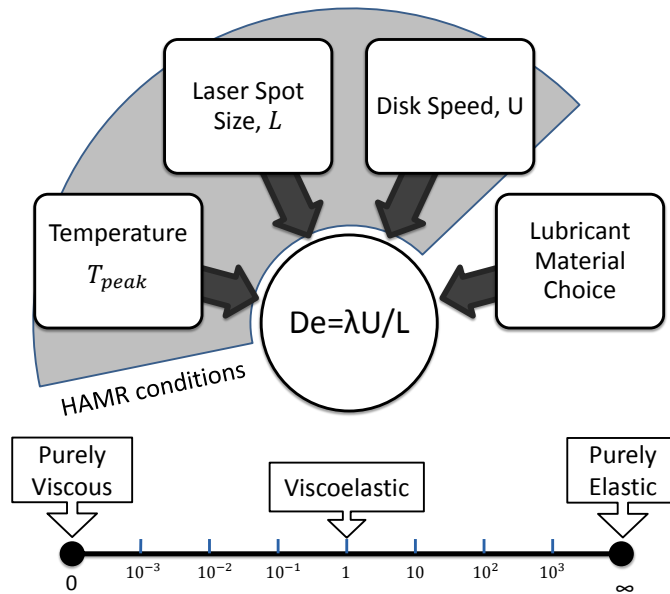
Figure 8.2: Deborah number is a function of lubricant material choice and HAMR conditions. Its magnitude determines if the lubricant exhibits the behavior of an elastic solid, a viscous fluid, or a viscoelastic fluid.

8.4   Limitations of the Lubrication Theory

During the development of the HDD lubricants, lubrication theory has been the method widely used and known to describe the behavior of the HDD lubricants very accurately. Many previous works in the literature use this method to model the behavior of the lubricant, both on the disk and the slider surfaces [15, 16, 41, 21, 48]. Some of these works model the lubricant using the lubrication theory, and run simulations to predict the behavior of the lubricant. Others use the lubrication theory as a benchmark to characterize the behavior of the lubricants.

As discussed in Chapter 3, many papers use a diffusion model (Eq. 3.21) for the lubricant evolution and find the diffusion coefficient $D(h)$ as a function of lubricant thickness; others measure the disjoining pressure $\Pi(h)$ and viscosity $\eta(h)$ properties for ultra-thin films of lubricant. For the case of HAMR, the first part of this dissertation along with the previous studies have used the lubrication or Reynolds equation (Eq. 3.19), to describe the behavior of the lubricant.

The derivation of the lubrication equation is discussed in Chapter 3 and can be found in many references such as [60]. To derive this equation, the lubricant is assumed to be Newtonian, and the Navier-Stokes equation is used. Then, lubrication assumptions, such as negligible inertia and quasi-parallel flow, apply for the ultra-thin films, which lead to the simplification of the Navier-Stokes equation. Finally, the flow across the lubricant q is found and is substituted into the integral form of the mass conservation law, the result of which is
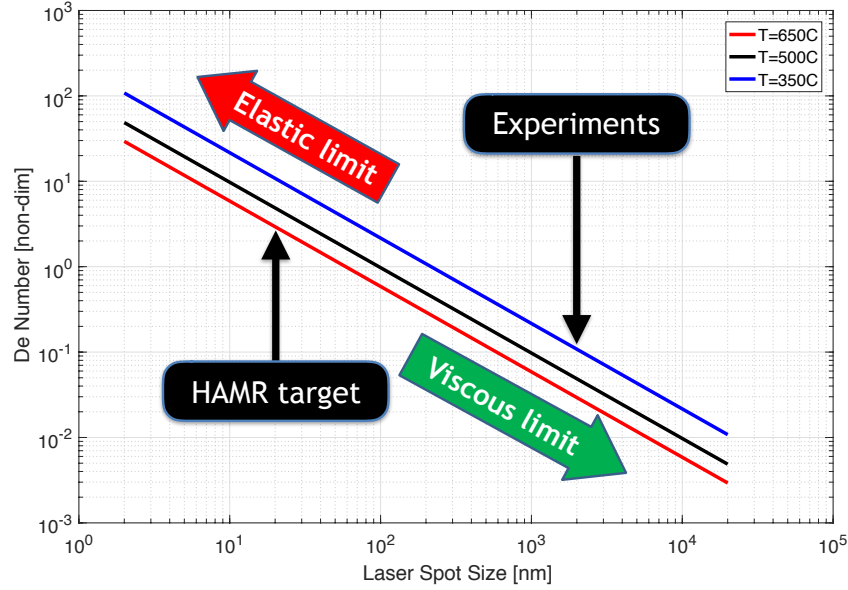
Figure 8.3: Deborah number as a function of laser spot size L, for different HAMR peak temperatures of $T = 350, 500, 650^oC$, for Z-tetraol 2000 and disk speed of $U = 5m/s$

the lubrication equation.

Figure 8.2 shows that when the viscoelastic effects are considered in the model, the only case when the lubricant behaves like a Newtonian viscous fluid is when $De = 0$ or sufficiently small. Therefore, modeling the lubricant with the lubrication (or diffusion) equation is only valid for the small Deborah number limit.

Figure 8.3 shows the Deborah number as a function of the laser spot size for different HAMR peak temperatures, based on experimental measurements for Z-tetraol 2000 [12]. This figure shows that for the micron size (and larger) laser spots, the lubricant behaves viscously and therefore, the lubrication equation applies at this limit. Interestingly, this is where most of the experiments are conducted due to the limited resolution of the focusing and measurement systems such as OSA [50, 23, 22]. However, for the target of HAMR with a length-scale of $L = 20nm$, Fig. 8.3 shows that the calculated Deborah number is larger, and therefore, the elastic behavior of the material can become dominant. In this case the lubrication theory cannot be expected to give valid results. Therefore, it is necessary to accommodate the viscoelastic effects in the numerical analysis, especially for the small laser spots close to the target for HAMR.

In order to include the effect of viscoelasticity and non-zero Maxwell relaxation time, we can pursue two different approaches. First, we can modify the lubrication equation (Eq. 3.19) so that it also accommodates the viscoelastic effects, and solve it with a Finite Volume Method, similar to the method used for depletion and reflow simulations in chapters 3-6. Alternatively, we can develop a direct approach to solve the evolution of a thin film of viscoelastic material (Eq. 7.1) using a Finite Element Analysis, a new approach that is essentially different from the lubrication theory.

The following sections present the methods and the results of this work.

Chapter 9

Lubrication Theory including Viscoelastic Effects

The numerical solutions of the lubrication equation are well established and known to be stable. However, the lubrication equation applies only to the thin-films of viscous Newtonian fluid. Therefore, one can use the solution of this equation as a perturbation leading term to find and solve for nearly-viscous viscoelastic fluids.

9.1 Constitutive Equations for Nonlinear Viscoelastic Maxwell Fluids

Reference [61] used a convected Maxwell model for the viscoelastic Maxwell fluid and simplified the constitutive equations to find a lubrication equation using a perturbation method, for a classic 2D bearing problem. We follow that example to find a direct solution for a 2D thin-film with lubrication assumptions applied. We use the notation and constitutive equations similar to that work.

Equations 9.1-9.4 show the (nonlinear) constitutive equations for a convected Maxwell fluid, along with the Cauchy equation of motion and continuity equation for an incompressible fluid in tensorial form:

$$\boldsymbol{\tau} + \lambda\check{\boldsymbol{\tau}} = \tfrac{\eta}{2}(\boldsymbol{\nabla}\boldsymbol{v} + (\boldsymbol{\nabla}\boldsymbol{v})^T), \tag{9.1}$$

$$\check{\boldsymbol{\tau}} = \tfrac{\partial\boldsymbol{\tau}}{\partial t} + (\boldsymbol{\nabla}\boldsymbol{\tau}).\boldsymbol{v} - (\boldsymbol{\nabla}\boldsymbol{v}).\boldsymbol{\tau} - \boldsymbol{\tau}.(\boldsymbol{\nabla}\boldsymbol{v})^T, \tag{9.2}$$

$$\boldsymbol{\nabla}.\boldsymbol{\tau} + \boldsymbol{\nabla}p = 0, \tag{9.3}$$

$$\boldsymbol{\nabla}.\boldsymbol{v} = 0, \tag{9.4}$$

where $\boldsymbol{\tau}$ is the deviatoric stress tensor, $\check{\boldsymbol{\tau}}$ is the convected stress tensor time derivative, $\boldsymbol{\nabla}\boldsymbol{v}$ is the velocity gradient, η is the lubricant viscosity, and λ is the Maxwell relaxation time. In the Cauchy equation of motion (Eq. 9.3), we have neglected the inertia term due to the lubrication assumptions. Also, in the continuity equation, the right hand side is set to zero, due to the incompressibility assumption. In Eq. 9.1, if $\lambda = 0$, the constitutive equation for a viscous Newtonian fluid is restored and a combination of this equation with Eq. 9.3 results

in the Navier-stokes equation which can be further simplified to the lubrication equation (Eq. 3.19 for HAMR), as discussed in Chapter 3. However, if $\lambda \neq 0$, the viscoelastic effects are considerable, and Eqs. 9.1-9.4 need to be solved together.

9.2 Derivation of Modified Lubrication Equation including Viscoelastic Effects

In the first part of this dissertation, we successfully investigated the solution for the HAMR lubrication equation in the absence of the viscoelastic effects, for both depletion and reflow regimes. This chapter follows upon the same method by finding a modified governing equation for a 2D thin-film of the viscoelastic lubricant, similar to that for a viscous lubricant, i.e. lubrication equation (Eq. 3.19 in 2D), with extra terms related to the viscoelastic effects. For simplicity, we use a 2D lubricant model by keeping the velocity gradients $v_{i,j}$ and the stress values τ_{ij} in the XZ plane only (i.e. $i, j \in \{1, 3\}$).

The next step is to non-dimensionalize the equations above. We use the following non-dimensionalization notation, where the asterisked parameters are dimensional, and the ones without asterisk are non-dimensional

$$
\begin{aligned}
x_1^* &= Lx, & v_1^* &= U + v_s v_1, \\
x_3^* &= h_0 z, & v_3^* &= \frac{v_s h_0}{L} v_3, \\
\tau_{13}^* &= \frac{c\Delta T}{L} \tau_{13} & (\tau_{11}^*, \tau_{33}^*) &= \frac{\eta_0 v_s}{L}(\tau_{11}, \tau_{33}), \\
p^* &= p_s p, & p_s &= \frac{3}{2}\frac{c\Delta T}{h_0}, \\
t^* &= t_s t, & t_s &= L/U, \\
\eta^* &= \eta_0 \eta & v_s &= \frac{h_0 c\Delta T}{2\eta_0 L}.
\end{aligned}
\tag{9.5}
$$

In the above equations, $v_s \ll U$, and the ratio between v_s and U is introduced in Ref. [15] as a non-dimensional advection velocity $C_u = \frac{2\eta_0 L^2}{h_0 c\Delta T}U$.

Finally, we can simplify Eqs. 9.1-9.4 to 2D, clear dimensions, and combine the constitutive equation (Eq. 9.1) with the Cauchy equation of motion:

$$
\tau_{13} + De(\tau_{13,t} + \tau_{13,1}) = \frac{\eta}{2}v_{1,3},
\tag{9.6}
$$

$$
\tau_{13,3} + \frac{3}{2}p_{,1} = 0,
\tag{9.7}
$$

$$
p_{,3} = 0,
\tag{9.8}
$$

where $De = \lambda U/L$ is the Deborah number and η is the normalized viscosity. Setting $\lambda, De = 0$ restores the first equation above to the constitutive equation for a Newtonian fluid. The last equation states that pressure can be considered constant across the lubricant thickness since the pressure gradient across the lubricant is negligible. The integration of Eq. 9.7

across the lubricant gives an expression for τ_{13} as

$$\tau_{13} = -\frac{3}{2} \int_0^h p_{,1} dz = \frac{3}{2} p_{,1}(z-h) + \tau_x, \tag{9.9}$$

where τ_{13} is the 1-3 component of the shear stress within the fluid, p is the pressure, and τ_x is the thermo-capillary shear stress on the lubricant free surface. Next, We integrate Eq. 9.6 twice across the lubricant film (z-direction) and find the (non-dimensional) lubricant flow:

$$q = \frac{2}{\eta} \int_0^h \int_0^z \tau_{13} + De(\tau_{13,t} + \tau_{13,1}) dz dz. \tag{9.10}$$

Combining the last two equations and substituting q into the (non-dimensional) mass conservation law, we find the modified version of the lubrication equation for viscoelastic lubricants:

$$h_{,t} + h_{,1} + \frac{1}{C_u} \frac{\partial}{\partial x_1} [-\frac{h^3}{\eta}(p_{,1} + De(p_{,1t} + p_{,11})) +$$
$$\frac{h^2}{\eta}(\frac{3}{2} De p_{,1}(h_{,1} + h_{,t}) + De\tau_{x,1} + \tau_x)] = 0, \tag{9.11}$$

where De is the Deborah number, η the non-dimensional viscosity, p the non-dimensional pressure, and τ_x is the thermo-capillary shear stress.

Setting $De = 0$ i.e., turning off the viscoelastic effects, we restore the non-dimensional form of the well-known lubrication equation (Eq. 3.19) which is also used in the previous studies for Newtonian viscous lubricants [15].

9.3 Numerical Stability of the Modified Lubrication Equation

Using a dispersive disjoining pressure model $p = A/h^3$ and a Gaussian temperature distribution model and corresponding thermo-capillary shear stress, we simulated the behavior of the lubricant according to the model presented by the governing equation (Eq. 9.11). Fig. 9.1 illustrates the results of these simulations for a thin-film of Z-tetraol 2000, with an initial thickness of $h_0 = 1.4nm$ for laser spot sizes of $L = 100nm, 200nm, 1\mu m$. The red curves in this figure represent the lubricant behavior in the absence of viscoelastic effects ($De = 0$), and the blue curves represent the ones including the viscoelastic effects.

In Fig. 9.1, the difference between the viscoelastic and purely viscous models indicates the effect of the viscoelastic terms in Eq. 9.11. This figure shows that the effect of viscoelasticity becomes more pronounced as the laser spot size decreases, and this agrees with our findings in Fig. 8.3. For example, for a laser spot size around $L = 1\mu m$, the difference between the viscoelastic and the viscous models is small. However, as the laser spot size decreases to $L = 100nm$, the difference between the two solutions becomes considerable, and the viscoelastic solution becomes unstable with a large peak on the trailing side. Especially, our simulations show that for the laser spots smaller than $100nm$, the solution becomes numerically unstable and therefore, the viscoelastic effects modeled by Eq. 9.11 cannot
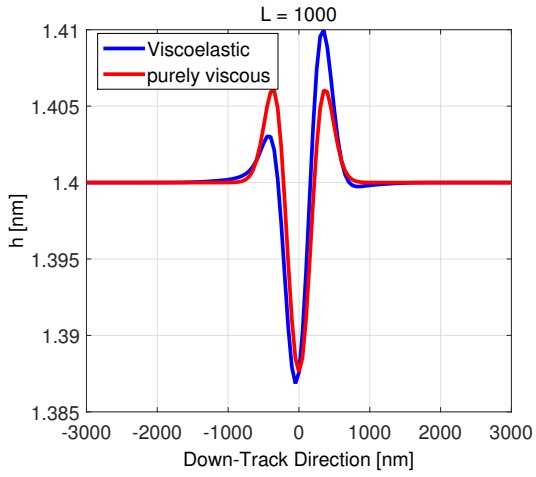
(a) Laser spot size $L = 1\mu m$
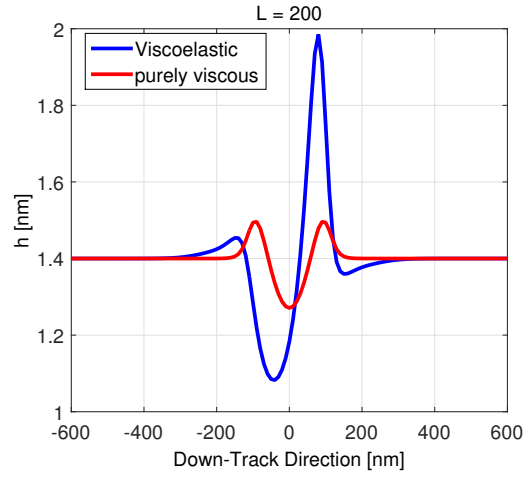
(b) Laser spot size $L = 200nm$
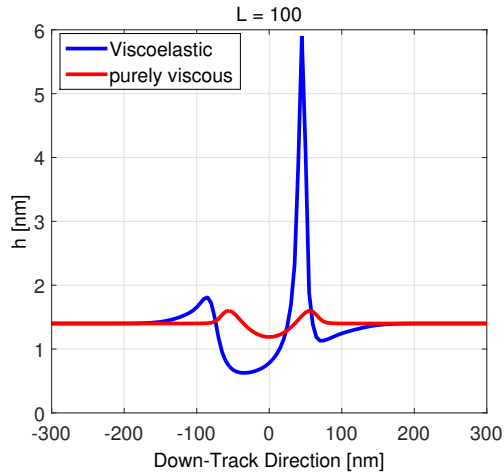
(c) Laser spot size $L = 100nm$

Figure 9.1: The simulation results of the depletion process for three laser spot sizes of $L = 100nm, 200nm, 1\mu m$ with a HAMR peak temperature of $T_p = 650^oC$, using the viscoelastic modified lubrication equation

describe this limit. In other words, the extra modifying nonlinear terms ($\propto De$) in Eq. 9.11 dominate the leading terms of the basic lubrication equation. According to Fig. 8.3, the Deborah number becomes relatively large for small laser spots, leading to a significant growth in the viscoelastic terms in Eq. 9.11, since they are proportional to the Deborah number.

The results of the numerical analysis here shows that although the stated viscoelastic governing equation may describe the lubricant behavior for nearly viscous regimes such as the ones with micron-size laser spots, it is unable to give accurate results for high Deborah number (nearly elastic) regimes like the lubricant under nano-size laser spots. With a careful stability analysis of Eq. 9.11, one can show that for large Deborah numbers, this equation becomes unstable. This numerical issue is well-know in the theory of non-linear viscoelasticity. Earlier studies suggest that the convected Maxwell models such as the one used in this work become numerically unstable, especially for high Deborah number regimes. For example, ref. [61] states that the Reynolds equation is limited to the low Deborah number regimes . Reference [62] states that the nonlinear constitutive equations for viscoelastic fluids can be numerically unstable, especially for high Deborah number regimes. Reference [63] also suggest that the nonlinear constitutive equations for viscoelastic fluids need to be carefully used since sometimes they are unstable for time-dependent flows.

These stability issues corresponding to the lubrication equation and its variations for viscoelastic flow motivated us to develop an essentially different approach to simulate the behavior of lubricants under HAMR conditions. The following chapter is dedicated to the introduction of this new approach.

Chapter 10

Simulation of Viscoelastic Lubricant using Finite Element Analysis

The results of our numerical analysis show that neither the lubrication theory nor its modified version for viscoelastic flow (Eq. 9.11) are able to describe the behavior of the viscoelastic PFPE lubricants under HAMR conditions with small laser spots. This necessitates the development of a new approach to solve for the thin-film viscoelastic PFPE lubricants. To do so, we employ the linear form of the viscoelastic constitutive equations (Eq. 7.1), and a Finite Element Method more suitable for the high Deborah number regimes such as depletion under small HAMR laser spots. Accordingly, the following sections introduce our new method to analyze the viscoelastic lubricants of interest. A requirement of this new method is that it should be stable for the entire range of Deborah numbers (Fig. 8.2), from $De = 0$ (viscous dominant limit) to $De = \infty$ (elastic limit).

10.1 FEA Discretization

We introduced the explicit integral forms of the constitutive equation for linear Maxwell fluids in Eq. 7.1. This nonlinear equation forms the basis for the Finite Element Analysis. First, Eq. 7.1 should be discretized in time in the following form:

$$\boldsymbol{\sigma}^{n+1} = \boldsymbol{\sigma}^n \exp(\frac{-dt}{\lambda}) + 2G_0 \exp(\frac{-dt}{2\lambda})[\boldsymbol{e}^{n+1} - \boldsymbol{e}^n],$$

$$(10.1)$$

where $\boldsymbol{\sigma}^n$, $\boldsymbol{e}^n$ and $\boldsymbol{\sigma}^{n+1}$, $\boldsymbol{e}^{n+1}$ are the deviatoric stress and strain tensors in the current and next time step, λ is the Maxwell relaxation time, dt is the timestep length, and G_0 is the local shear rigidity of the material (Eq. 7.3). The pressure term $-p\boldsymbol{I}$ is the Lagrange multiplier to impose incompressibility to the material elements.

In this analysis, the disk is fixed (accordingly the material elements), and the laser spot as well as the thermo-capillary shear stress (τ_x, τ_y) and the temperature $T(x, y; t)$ move along the track with a speed $U = 5m/s$. Accordingly, the parameters that are functions of the temperature and lubricant thickness also need to be updated at each time-step, including the Maxwell relaxation time λ, viscosity η, and the disjoining pressure $\Pi(h)$.
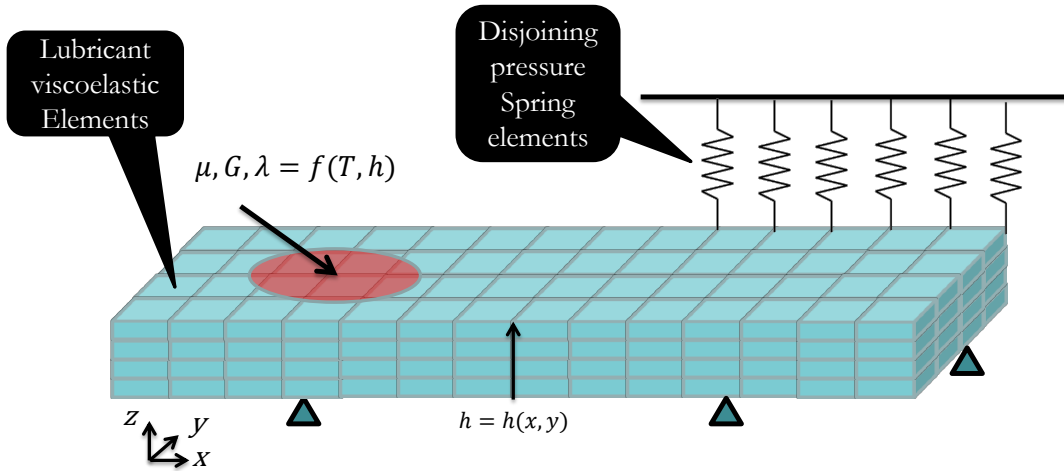
Figure 10.1: A schematic depiction of the 3D mesh used for FEA analysis of the problem.

After the discretization in time, we meshed the physical domain. We use a Lagrangian structured mesh, moving with the material elements, with eight-node brick elements similar to a classical mesh for an elastic solid problem (Fig. 10.1). The aspect ratio of the mesh elements are accepted when the horizontal length scales are of the order of $L = 20nm$, however, we should keep in mind that as we increase the laser spot size and therefore the horizontal domain while keeping the lubricant thickness constant, the aspect ratio of the mesh elements grows. In particular for a lubricant thickness of $h_0 = 1nm$, when the laser spot size exceeds a limit of $L = 5\mu m$, the aspect ratio of the elements becomes too large for the numerical solver to handle.

Figure 10.1 shows a schematic view of the mesh used to model the lubricant. For each timestep we update the position of the laser spot moving down the track, and update the temperature distribution. Also, at each timestep, we read the results of that timestep to find the last updated vertical displacement of each top node (Δh), and then we use it to update the local lubricant thickness of that node ($h = h_0 + \Delta h$). So, by updating the temperature T and lubricant thickness h at each node we can update the thermo-capillary shear stress (τ_x, τ_y), disjoining pressure $\Pi(h)$, and material properties. To each element, we separately assign a specific viscosity $\eta(T,h)$, shear rigidity $G_0(h)$, and Maxwell relaxation time $\lambda(T)$ as functions of temperature T and lubricant thickness h. Here in this study, we assume that these parameters are constant for the elements across the film and vary along the film.

10.2 Disjoining Pressure Model in the FEA

Before the laser irradiation, the lubricant profile is uniform, it has a film thickness of h_0, and the disjoining pressure is also uniform and has a reference value of $\Pi(h_0) = A/h_0^3$. So when the lubricant depletes and its profile becomes non-uniform, the film thickness will be an arbitrary value $h(x,y) = h_0 + \Delta h(x,y)$ for each local point, and therefore, the difference $\Delta\Pi(\Delta h)$ between the corresponding disjoining pressure and the reference disjoining pressure
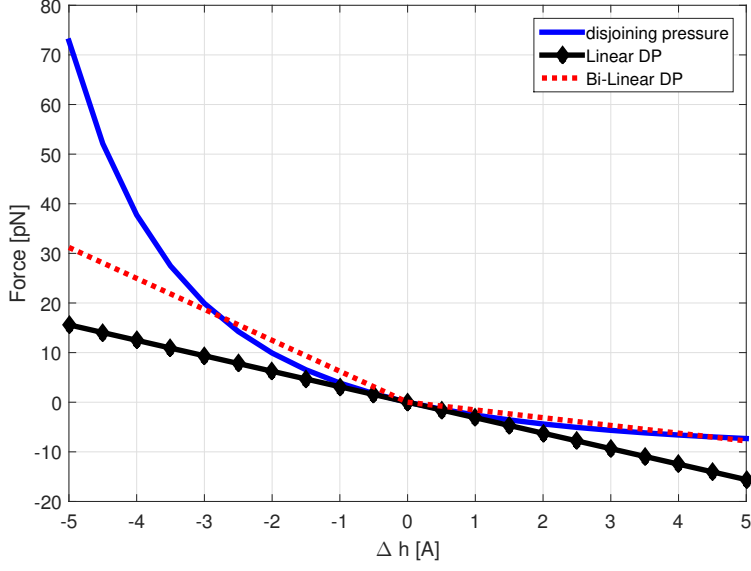
Figure 10.2: Nonlinear $F(\Delta h)$, linear $F_L(\Delta h)$, and bi-linear $F_{BL}(\Delta h)$ Element Disjoining force as a function of lubricant thickness difference Δh

becomes:

$$\Delta\Pi(\Delta h) = \Pi(h_0 + \Delta h) - \Pi(h_0)$$
$$= \frac{A}{(h_0 + \Delta h)^3} - \frac{A}{h_0^3}. \qquad (10.2)$$

This equation suggests when the lubricant is disturbed, $\Delta h \neq 0$, and a non-zero disjoining pressure difference appears ($\Delta\Pi \neq 0$) that forces the lubricant surface to move to the initial undisturbed thickness $h = h_0$ with $\Delta h = 0$. In fact, the disjoining pressure plays the role of a non-linear spring force acting on the lubricant surface. Considering a surface element with the size $dx \times dy$ corresponding to the lubricant with a local thickness of $h \neq h_0$, the restoring force on the surface element is:

$$F(\Delta h) \quad = \Delta\Pi(\Delta h)dxdy$$
$$= \left(\frac{A}{(h_0 + \Delta h)^3} - \frac{A}{h^3}\right)dxdy. \qquad (10.3)$$

Using values $A = 2.6 \times 10^{-21} J$, $h_0 = 1nm$, and $dx = dy = 2nm$, we plotted the disjoining force $F(\Delta h)$ as a function of lubricant thickness difference Δh in Fig. 10.2.

This formulation for disjoining force $F(\Delta h)$ states that when Δh is zero, the forcing $F(\Delta h)$ is also zero. When Δh is negative, the forcing on the surface element is positive, and vice versa. This suggests that the disjoining pressure acts similar to a non-linear spring on the material elements, whose force-displacement relation obeys Eq. 10.3 and the blue curve in Fig. 10.2. So, for each node on top of the lubricant surface (Fig. 10.1), we add a

71

spring element with the force-displacement relation $F(\Delta h)$ as in Eq. 10.3 and Fig. 10.2. A schematic of the disjoining pressure non-linear springs is illustrated in Fig. 10.1.

According to Fig. 10.1 and Fig. 10.2, when the lubricant depletes ($\Delta h < 0$) the spring's stiffness ($F - \Delta h$ slope) increases, and the forcing increases significantly, similar to the disjoining pressure curve. From a disjoining pressure point of view, when the lubricant thickness decreases, the disjoining pressure derivative $d\Pi/dh$ increases as well.

To use nonlinear springs is numerically expensive in a Finite Element Analysis since it imposes an extra iteration cycle on the analysis. Also, modeling the nonlinear springs as active forces on the nodes can invoke numerical instabilities in the analysis. Conversely, linear springs cost only a tiny fraction of that numerical expense, since they only populate the global stiffness matrix with static values, and this helps the numerical analysis to become even more stable. Considering the numerical issues, we choose to linearize the the function $F(\Delta h)$ in Eq. 10.3 around $h = h_0$ or $\Delta h = 0$:

$$F_L(\Delta h) = -[3\frac{A}{h_0^4}dxdy]\Delta h. \tag{10.4}$$

Therefore, the spring constant of each of the disjoining pressure elements becomes $K = 3\frac{A}{h_0^4}dxdy$, and as illustrated in Fig. 10.1, each spring connects a top node on the lubricant to a fixed point. One should note that for a general format of the disjoining pressure $\Pi(h)$, the spring constant K is determined by the slope of the Π-h curve which is actually the disjoining pressure derivative $d\Pi/dh$ (Fig. 6.2), and it is $K = -[d\Pi/dh]_{h=h_0}dxdy$. So, the larger the disjoining pressure derivative, the stiffer the disjoining pressure elements become. When the disjoining pressure derivative is negative (as it is in the case of $\Pi(h) = A/h^3$), the spring constant is positive and the springs act as restoring agents. However in the presence of the dewetting and polar effects, if the disjoining pressure derivative becomes positive, the spring constant becomes negative, pushing the Finite Element model towards the dewetting unstable region. So, the Finite Element springs can capture the lubricant disjoining pressure behavior completely.

Reference [36] was the first to interpret the disjoining pressure derivative $d\Pi/dh$ as "film stiffness" since the disjoining pressure derivative is proportional to the lubricant driving force to reflow. This interpretation is similar to the linear spring analog that we consider here for the disjoining pressure. In Chapter 6, we discussed the importance of the disjoining pressure derivative as well.

Figure 10.2 shows that the linear spring model (black curve) is very close to the actual disjoining force curve (blue one) only for a limited thickness change of $-1A < \Delta h < 1A$. However beyond this limit, the difference between the actual disjoining force $F(\Delta h)$ and the linearized version $F_L(\Delta h)$ becomes considerable. To solve the problem and expand the accuracy limit of the linear model, we transform the linear model to a bi-linear one ($F_{BL}(\Delta h)$) also shown in Fig. 10.2. This bi-linear model assigns two different stiffness values to the disjoining springs depending on if they are under compression ($\Delta h < 0$) or tension ($\Delta h > 0$). As a result, the corresponding bi-linear function $F_{BL}(\Delta h)$ becomes very close to the actual nonlinear forcing function $F(\Delta h)$ in the limit $-3A < \Delta h < 5A$ (Fig. 10.2), and it has the

form:

$$F_{BL}(\Delta h) = \begin{cases} -[6\frac{A}{h_0^4}dxdy]\Delta h & \text{for } \Delta h < 0, \\ -[\frac{3}{2}\frac{A}{h_0^4}dxdy]\Delta h & \text{for } \Delta h > 0. \end{cases} \qquad (10.5)$$

So, the bi-linear model has different spring constants under tension and compression. It is accurate enough and computationally cost effective and is used accordingly. In the future work, we can add a more accurate spring model that modifies the stiffness dynamically and takes into account the effect of the polar disjoining pressure as well.

The developed FEA for this study consists of more than 300 lines of code in ANSYS APDL for the core calculations, and then, the nodal solutions are exported to MATLAB for post-processing. For a typical problem with a laser spot size of $L = 20nm$, lubricant thickness of $h_0 = 1nm$, and laser exposure time of $t_{exp} = 20ns$, we considered a time-step of $dt = 0.1ns$ and a mesh size of $dx, dy = 2nm$, and $dz = 0.1nm$. For larger laser spot sizes of $L = 200nm$ and $L = 2\mu m$ the exposure time t_{exp}, time-step size dt, and mesh size (dx, dy) scale accordingly.

An essential requirement for the accuracy of the lubrication theory is the separation of the length scales. In other words, lubrication theory is known to give more accurate results as $h/L \to 0$, or in the case of HAMR for larger laser spots [60]. For the FEA approach however, an increase in the laser spot size ($h/L \to 0$) increases the aspect ratio of the mesh elements, leading to the reduction in the numerical stability and accuracy of finite element analysis. Our calculations show that for a typical lubricant layer with a film thickness of $h_0 = 1nm$, the maximum laser spot size possible for the FEA to solve is around $L = 5\mu m$. For smaller laser spots including the HAMR target of $L = 20nm$, the mesh element aspect ratio is appropriate, and the FEA is stable.

10.3   FEA Method Validation

In Section 8.3, we discussed the non-dimensional Deborah number as the indicator of the behavior of the material (Fig. 8.2). When the Deborah number is relatively large, the lubricant behaves elastically, and when it is close to zero, the lubricant behaves like a Newtonian viscous fluid, and the lubrication equation (Eq. 3.19) describes the behavior of the lubricant at this limit. So, the Deborah number indicates a spectrum of behavior, and our viscoelastic FEA approach should describe the entire scope of that spectrum.

When viscoelastic effects are present, the Maxwell relaxation time λ and the Deborah number are non-zero, and the strength of the viscoelastic effects is proportional to the Deborah number. In Fig. 8.3 we plotted the typical Deborah numbers for Z-tetraol 2000 according to the Maxwell relaxation time measurements by Karis.

In the absence of the viscoelastic effects, the Deborah number is zero, and the lubricant is fully described by the lubrication theory. The earlier part of this dissertation as well as previous works [15, 16] have successfully simulated the behavior of the lubricant under HAMR conditions using lubrication theory. Before we proceed to simulate the viscoelastic lubricants using the FEA approach, it is essential to verify that, in the absence of the viscoelastic effects, the FEA approach calculates the same results as lubrication theory in the previous studies. To do so, we artificially suppress the viscoelastic effects by setting λ

(a) 3D view of the depleted track

(b) Cross-Track view of the depleted lube

(c) Down-Track view of the depleted lube

(d) Depletion/Accumulation time history
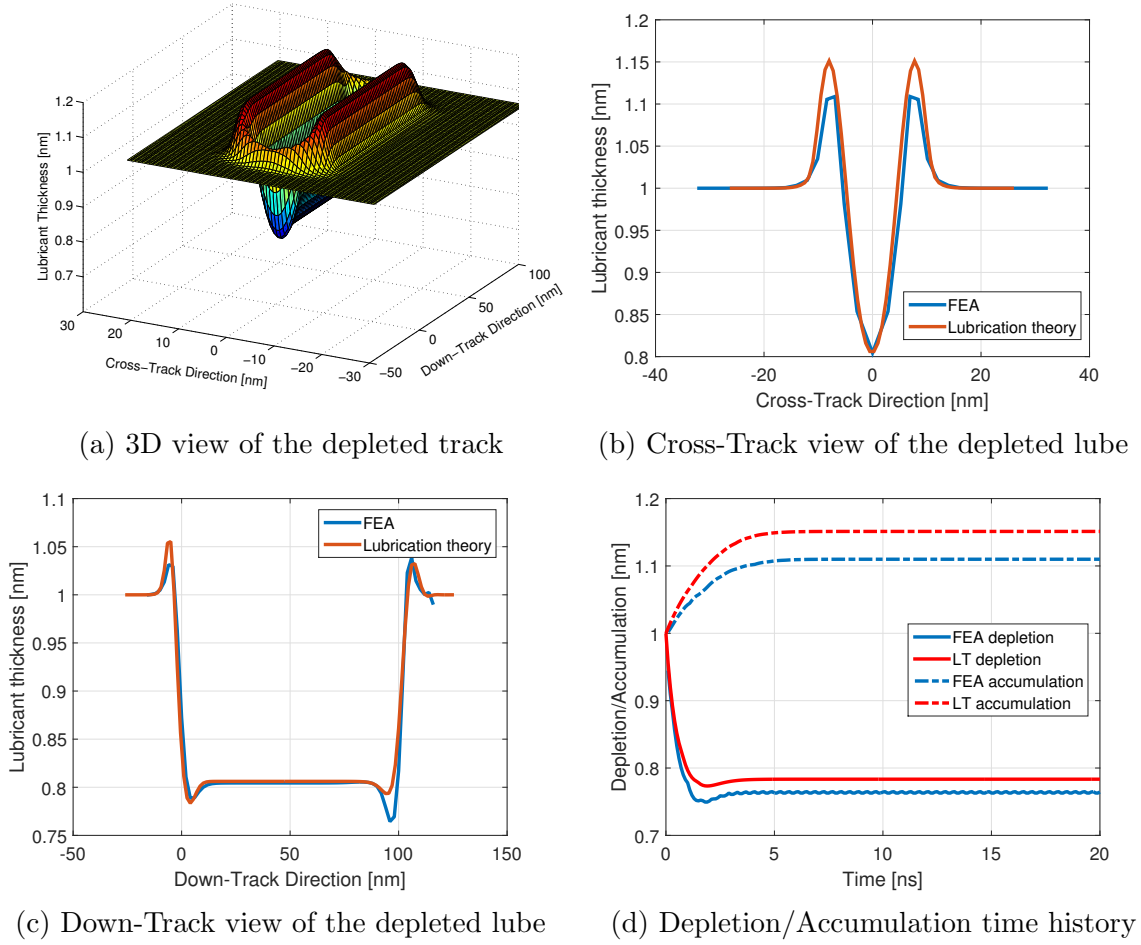
Figure 10.3: A comparison between results of viscous fluid using lubrication theory, and FEA with suppressed viscoelastic effects ($De = 0$)

and De to zero, and apply the new FEA to see if its results match the lubrication theory results from previous studies. If this condition is satisfied for $De \to 0$, with the knowledge that FEA is reliable for elastic solids ($De \to \infty$), we can guarantee that the new developed FEA works accurately for the entire range of viscoelasticity ($0 < De < \infty$).

Using the same method from our previous simulations for viscous lubricants [41], we solved Eq. 3.19 for Z-tetraol 2000 and simulated the depletion process with an initial thickness of $h_0 = 1nm$ exposed to a laser with the speed $U = 5m/s$, spot size of $L = 20nm$, peak temperature of $T_p = 350^oC$, and an exposure time of $t_{exp} = 20ns$ during which the laser travels down the track by $\Delta x = 100nm$, and it forms a trough and two side ridges along the track. The results of this calculation are shown in Fig. 10.3b. The red curves in this figure show the cross-track (Fig. 10.3b) and down-track (Fig. 10.3c) sections of the depleted trough as well as the depletion and accumulation as a function of time (Fig. 10.3d).

Alternatively, we repeated the simulations of the case mentioned above using the viscoelastic FEA, while we (artificially) suppressed the effects of viscoelasticity, and pushed the lubricant's Maxwell relaxation time λ and De to zero ($De = 0.003$). As shown in Fig. 10.3,

74

the results from lubrication theory and viscoelastic FEA are close to each other, in the limit of $De \rightarrow 0$.

Figs. 10.3b and 10.3c show that after $20ns$ of laser exposure, the shape of the troughs are close to each other, in both cross-track and down-track directions. Additionally, Fig. 10.3d shows that the time constants of depletion and accumulation are the same for both cases. It takes almost $2ns$ for the depletion to fully develop, and $5ns$ for side ridges to grow to the full extent.

Overall, these results show that the lubricant's FEA solution for the limit of $De \rightarrow 0$ is very close to the results of the Lubrication Theory from previous studies. This means that the FEA solver gives reasonable results in this limit. Therefore, we can conclude that the FEA solver is reliable in the whole range of Deborah numbers and behavior spectrum, from purely viscous to purely elastic.

10.4 FEA Results for a Viscoelastic Lubricant

In the previous section, we excluded the viscoelastic effects by setting the Deborah number to zero. Here, we present the simulation results for the behavior of Z-tetraol 2000 under HAMR conditions, including the viscoelastic effects, where the viscoelastic parameters are non-zero, given in Table 7.1.

In this section, we present the result of the simulations for different laser spot sizes of $L = 20nm$ close to the target of HAMR, $L = 200nm$ an intermediary size, and $L = 2\mu m$ a usual experimental condition for focused laser without NFT. In all of these cases, we simulate a thin-film of Z-tetraol 2000 with an initial uniform thickness of $h_0 = 1nm$. The laser speed in all cases is $U = 5m/s$, and the HAMR peak temperature is $T_p = 350^oC$. For each simulation, we set the exposure time proportional to the laser spot size "L" so that the laser travels a distance of about 5L. In this case, we observe the whole development stage as well as steady state form of the trough. Therefore, for $L = 20nm, 200nm, 2\mu m$, we simulate the laser exposure times of $t_{exp} = 20ns, 200ns, 2\mu s$ respectively. After the exposure process, we remove the laser effects, such as thermo-capillary shear stress and high-temperature effects, and continue the simulations for a few more timesteps. This helps investigate the transient reflow behavior of the lubricant right after the laser exposure ends.

10.4.1 Depletion/Recovery Profile

At the target conditions for HAMR, the laser spot size is about $L = 20nm$. For this case the characteristic timescale of the lubricant evolution is around $t_s = L/U = 4ns$, and the corresponding Deborah number is around $10 < De < 10^5$. Figure 10.4 shows the lubricant evolution for this case. Figure 10.4a shows the lubricant deformation right after the laser exposure starts. It shows that the trough forms instantaneously. The trough is axisymmetric and has a depth of $5A$. The side ridges are circular and have a height of $1A$. The trough width (i.e. side ridge radius) is around $40nm$, twice the size of the laser spot size ($\approx 2L$). The laser irradiation continues for $20ns$ during which the laser moves down the track by $\Delta x = 100nm$, and Fig. 10.4b shows the state of the trough after $20ns$. A comparison between Fig. 10.4a and Fig. 10.4b indicates that during the laser exposure the trough

shape remains constant and translates with the laser spot, leaving no trail behind it. Figure 10.4c shows the lubricant profile right after the laser exposure ends and the laser effects are removed. This figure suggests that the viscoelastic lubricant recovers immediately after the laser is removed.
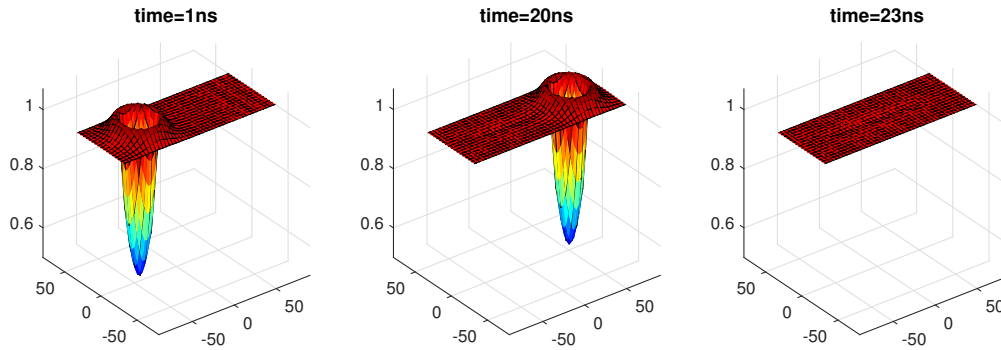
Figure 10.4: Viscoelastic FEA results for lubricant deformation and a laser spot size of $L = 20nm$ a) right after the laser exposure, b) after a $20ns$ period, c) right after the laser exposure ends

Figure 10.5 shows the simulation results for an intermediary laser spot size of $L = 200nm$. Figure 10.5a shows the lubricant profile right after the laser exposure, for the laser spot size of $L = 200nm$. The trough depth in this case is much smaller than for the laser spot size of $L = 20nm$ since the thermo-capillary shear stress is 10X smaller for this case compared to $L = 20nm$. One should remember that in this part, we only take into account the thermo-capillary effects that cause the mechanical deformation, and neglect the evaporation and thermal degradation effects. In the case of $L = 200nm$ the trough takes almost $10ns$ to form, and after that, as the laser spot moves, two stages of deformation appear. First, an axisymmetric trough is formed similar to the $L = 20nm$, moving with laser spot down the track. Second, a tail forms behind the trough whose depth and width is smaller than but comparable with the trough. Figure 10.5b shows the lubricant profile after $200ns$ of laser exposure during which the laser moves down the track by $\Delta x = 1\mu m$. This picture indicates that the tail behind the trough is visible and has a length equal to the laser travel distance of $\Delta x = 1\mu m$. After $200ns$ of laser exposure, we remove the laser effects to observe the recovery behavior. Figure 10.5c shows the lubricant profile right after the laser is removed. It shows that the first part of the deformation, i.e. the trough under the laser spot, vanishes, similar to the case of $L = 20nm$. However unlike the case of $L = 20nm$ the second part of the deformation, i.e. the tail behind, stays after the laser is removed.

Figure 10.6 shows the lubricant profile history for a large laser spot size of $L = 2\mu m$. Figure 10.6a shows that the trough formation is a gradual process in this case, and the trough takes $100ns$ to form. After that, as the laser moves down the track, the tail behind the trough has the same depth as the leading trough right under the laser spot. Figure 10.6b shows the lubricant profile after $2\mu s$ of laser exposure during which the laser travels $10\mu m$ down the track. This figure shows that although the laser spot size is $L = 2\mu m$, the trough length is $10\mu m$ equal to the distance that the laser traveled during the $2\mu m$ of exposure. Afterward, we remove the laser, and let the lubricant recover. Figure 10.6c shows the state
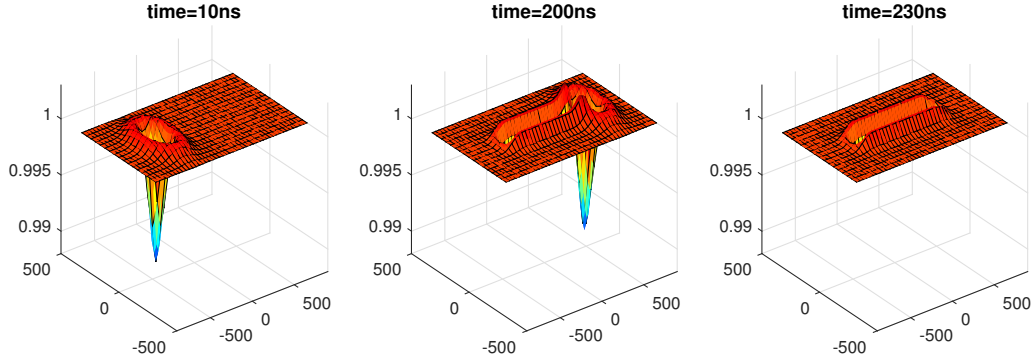
Figure 10.5: Viscoelastic FEA results for lubricant deformation and a laser spot size of $L = 200nm$ a) right after the laser exposure, b) after a $200ns$ period, c) right after the laser exposure ends

of the lubricant slightly after the laser is removed. However, we observe no instant recovery in lubricant profile when we compare the profile before and after the laser is removed (Figs. 10.6b and 10.6c). This shows that the depletion generated by the laser in this case stays in form of a long-term deformation after the laser is removed, in contrast with the case of $L = 20nm$.
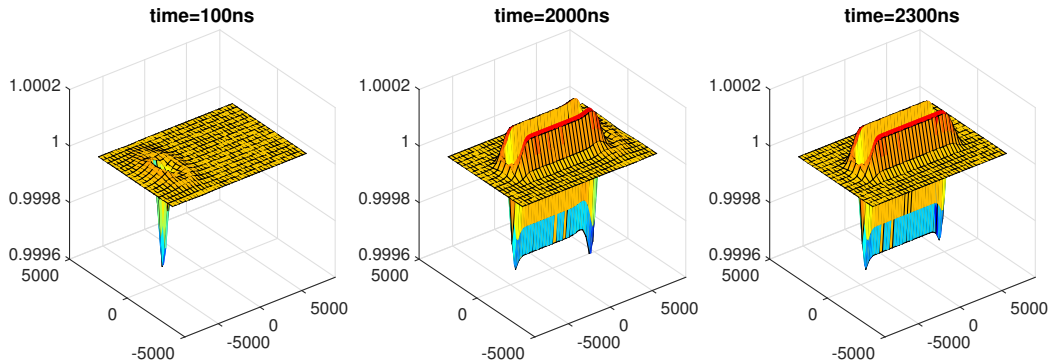
Figure 10.6: Viscoelastic FEA results for lubricant deformation and a laser spot size of $L = 2\mu m$ a) right after the laser exposure, b) after a $2\mu s$ period, c) right after the laser exposure ends

In summary, for the three cases of $L = 20nm, 200nm, 2\mu m$, we showed that the lubricant exhibits different behaviors in terms of the tail behind the spot, with a meaningful trend. The case of $L = 20nm$ generates no tail behind the laser spot. The case of $L = 200nm$ generates a tail behind the laser spot, which is comparable with the main trough in terms of depth and width. In the case of $L = 2\mu m$, the trough and the tail have the same depth, such that the trough right under the laser spot, and the tail behind it are not very distinguishable.

10.4.2 Depletion/Recovery Rate

The three cases of $L = 20nm, 200nm, 2\mu m$ show different behaviors in terms of the depletion recovery rate. Figure 10.7 shows the non-dimensional trough depth as a function of non-dimensional time, for each case of $L = 20nm, 200nm, 2\mu m$, with corresponding time scales of $t_s = 4ns, 40ns, 400ns$ respectively. So, for all cases, the non-dimensional laser exposure time interval is $0 < t < 5$. After this time interval, we continue the simulations for lubricant recovery for a short period of $5 < t < 6$.
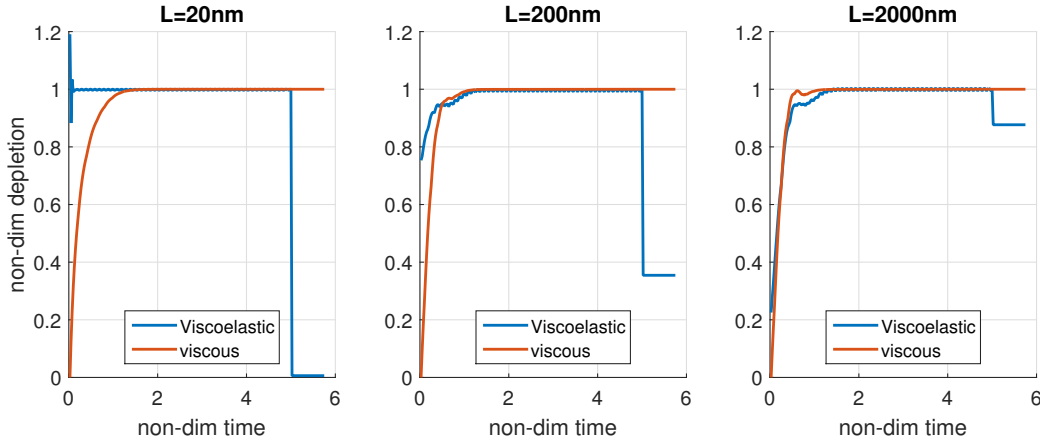
Figure 10.7: Time history of the depletion for 3 laser spot sizes of $L = 20nm, 200nm, 2\mu m$. In each plot the results of the viscoelastic FEA are compared to the case of the viscous lubricant where the viscoelastic effects are suppressed. The time is normalized by the timescale and depletion by maximum depletion of each case.

The red curves in Fig. 10.7 are the results of the lubrication theory (Eq. 3.19), when the viscoelastic effects are absent. In terms of depletion, the red curves in all three cases start from zero, and over time the depletion builds up to the maximum. In terms of recovery, after the laser is removed at $t = 5$, no significant change is observed in the lubricant profile. This is because the lubrication theory predicts the time scale of recovery to be far longer than the timescale of depletion [58]. According to that theory, the timescale for depletion is determined mainly by the balance between the thermo-capillary shear stress and the thin-film viscosity, whereas the time scale for recovery is determined by the balance between the disjoining pressure gradient and the viscosity.

The blue curves in Fig. 10.7 are the FEA results for the viscoelastic lubricants. The major difference between the red curves (no viscoelasticity) and the blue curves (viscoelasticity included) is in the jumps observed right after the start of laser exposure, $t = 0$, and right after the laser is removed, $t = 5$.

For case of $L = 20nm$, the blue and red curves are very different (Fig. 10.7a). Unlike the viscous model, the viscoelastic lubricant instantaneously reaches its maximum depletion, as soon as the laser effects are present, and the depletion immediately recovers after the irradiation. Figure 10.7a shows that the depletion for the viscoelastic lubricant has the form of a step function for $L = 20nm$.

For case of $L = 200nm$, Fig. 10.7b shows that a major part of the depletion occurs instantaneously, and part of it occurs gradually, over a course of $10ns$. After the laser is

removed in this case, about 60% of the depletion recovers instantaneously, and the rest 40% remains as a long-term depletion to be recovered by the Poiseuille flow driven by the disjoining pressure gradient. The recovery timescale for this post-HAMR deformation is much larger the one for the HAMR depletion, as discussed in Chapter 6.

For case of $L = 2\mu m$, the blue and red curves in Fig. 10.7c are very close to each other. The viscoelastic lubricant shows almost no instantaneous depletion. Instead, the trough takes almost 100ns to develop from zero. After the laser is removed, almost 90% of the depletion remains as a long-term depletion to be recovered. Accordingly, the depletion/recovery speed curves suggest that the viscoelastic behavior of the lubricants is very different from the viscous limit for small laser spots like $L = 20nm$, but it approaches the viscous limit for larger spots like $L = 2\mu m$.

10.5   Discussion

The results presented above along with Deborah number (Fig. 8.3) show that for the larger laser spots, the difference between the viscoelastic and viscous models is small, as illustrated in Figs. 10.6 and 10.7c for $L = 2\mu m$. However as the laser spot size decreases, approaching the target of HAMR, the viscoelastic effects grow, and the difference between the viscous and viscoelastic models becomes more pronounced. Figure 8.3 shows that $De = 0.11(< 1)$ for $L = 2\mu m$ and it grows to $De = 11(> 1)$ for $L = 20nm$, suggesting that the lubricant behavior must shift from a Newtonian viscous fluid to a predominantly elastic solid. This effect can be seen in terms of the depletion shapes, depletion/recovery rate, and the trough depth and width.

For the case of $L = 20nm$, the shape of the trough is significantly different when the viscoelastic and viscous models are compared. Figure 10.3a shows the lubricant depletion when the viscoelastic effects are disabled. This figure suggests that in the absence of the viscoelastic effects, the resulting profile is a depleted track with two side ridges. Conversely, Fig. 10.4b shows when the viscoelastic effects are present, the trough shape changes significantly to an axisymmetric one which follows the location and the axisymmetric shape of the laser spot and the thermo-capillary shear stress.

In the case of $L = 20nm$, the depletion/recovery rate is also different for the viscous and viscoelastic models. Figure 10.7a compares the depletion speed between the cases of viscoelastic and Newtonian lubricants for $L = 20nm$. It shows that depletion for the viscoelastic lubricant has a step behavior in time, whereas, the Newtonian lubricant needs time to gradually deplete. In addition, after the laser is removed and the uniform temperature is returned to the lubricant, the lubricant behavior is different for the viscoelastic and Newtonian cases. For the case of the Newtonian lubricant, the lubricant depletion (Figs. 10.3b and 10.3c) needs a relatively long time to recover since the reflow timescale is determined through the balance of the disjoining pressure gradient and thin-film viscosity. But for the case of the viscoelastic lubricant, the depletion recovers immediately after the laser is removed, according to Fig. 10.7a. This instantaneous recovery can also be seen in Figs. 10.4b and 10.4c illustrating the lubricant profile right before and after the laser removal.

This significant change in the depletion characteristics indicate that the viscoelastic effects are very important for the case of $L = 20nm$, close to the target of HAMR. In fact, the

viscoelastic effects in this case are so significant that they shift the behavior of the lubricant from a purely viscous fluid to a purely elastic solid.

Both the viscoelastic lubrication equation (Chapter 9) and the FEA approach (results above) in this study suggest that the behavior of the viscoelastic lubricant significantly deviates from the one for a viscous material as the laser spot size decreases. In this case, the use of the lubrication equation for a purely viscous model can be highly misleading. For a Newtonian viscous fluid model, the shear stress relaxes instantaneously, whereas the measurements show that it takes a few microseconds for the lubricant stress to relax (Fig. 7.2). Considering that the HAMR writing process takes place in a few nanoseconds, the lubricant stress does not have enough time to relax, leading to an elastic behavior.

In contrast to the case of $L = 20nm$, the results for the case of $L = 2\mu m$ show that the viscoelastic and Newtonian viscous solutions are quite close to each other in terms of depletion/recovery shape and rate, suggesting that the viscoelastic effects are not that important in the case of micron size spots. This meaningful difference between the case of $L = 20nm$, and $L = 2\mu m$ suggests that the experiments in the micron-size regime cannot describe the behavior of the material in the nano-size regime at the target of HAMR. Moreover, it points to a necessity to develop a different modeling protocol for the lubricant behavior under nano-size laser spot conditions.

Chapter 6 along with the previous studies on the HAMR depletion problem are based on lubrication theory and suggest that the depletion is significant for laser spot sizes close to the target of HAMR, and the recovery time can vary between tens of microseconds to hundreds of milliseconds [19, 23, 16]. Conversely, our viscoelastic Finite Element Analysis for the laser spot size of $L = 20nm$, close to the target of HAMR, suggests that lubricant depletion is significant, at $5A$ depth for a $1nm$ film thickness of Z-tetraol2000, but it recovers almost instantaneously, as soon as the laser exposure ends, similar to an elastic solid. Therefore, considering the viscoelastic effects, this study predicts that lubricant depletion due to the thermo-capillary effects will not be a significant issue in the development of the HAMR technology, since it produces no residual depletion in the laser track.

In this study, we neglected the effects of evaporation and thermal degradation on depletion, and took into account only the effect of lubricant mechanical deformation (flow) due to the thermo-capillary effects. The key difference between depletion due to evaporation and depletion due to thermo-capillary effects is in the existence of the side ridges. In a depletion due to thermo-capillary effects, the lubricant can only deplete to the side ridges since the conservation of mass holds. Conversely, in a depletion due to thermal degradation and evaporation, no side ridges should be observed since each particle leaves its local position, decreasing the local lubricant thickness only. Therefore, when the effect of evaporation is combined with high Deborah number HAMR conditions, the resulting depletion should be a trough with negligible side ridges. This is because the mechanical deformation is elastic and recovers as soon as the laser is passed, but the depletion due to the evaporation needs a significant time to recover.

Some HAMR experiments agree with the findings of this study for a viscoelastic lubricant, although due to the size limitations for NFT and measurement systems like OSA, a direct validation for the results of this study may be difficult. Reference [51] investigated the effect of exposure time on lubricant depletion for a thin-film of Z-tetraol A20H with an initial thickness of $h_0 = 1.2nm$ exposed to a focused laser with a spot size of $L \approx 1\mu m$. They

expose the disk to the laser for durations of $t_{exp} = 2ns$ with time intervals of around $50ns$ and different repetitions. Although the laser spot size in their experiments is relatively large, the exposure time is very small, leading to a high Deborah number. They show that for a total laser exposure time of $12ns$, the lubricant profile has negligible side ridges. As the laser exposure time increases the side ridges grow, which is an accumulative effect of the repetition and the residual depletion. For a total laser exposure of almost $5\mu s$ the lubricant deformation shows relatively large side ridges. When the exposure time is small, the lubricant material has no time to relax the stress, and therefore, thermo-capillary effects cannot make any long-term deformation in the lubricant. But when the exposure time increases to around $5\mu s$ thermo-capillary effects have enough time to deplete the lubricant and accumulate it on the side ridges. Although no experiments close to the target of HAMR with high Deborah number have been published to date, this experiment and similar ones are strong evidence for the effect of viscoelastic behavior on lubricant depletion under HAMR conditions.

Chapter 11

Conclusion and Future Work

11.1 Conclusion

This dissertation is dedicated to the development of hard disk drive lubricants for the promising Heat Assistant Magnetic Recording technology. Through these simulation studies, we investigated the performance of PFPE lubricants and found a more realistic model describing them. Hopefully this will help the developers and researchers in the HDD industry have a better understanding of the physics of the lubricants under HAMR conditions. This dissertation models the HAMR lubricants with two major approaches.

   The first approach describes the behavior of PFPE lubricants based on a Newtonian viscous fluid model where the lubrication theory applies and has been a well-known tool for decades in HDD research and development. Lubrication theory is a simple yet powerful tool to simulate these lubricants. Applying lubrication theory for these lubricants has unique challenges as addressed in this work. Although the disjoining pressure is very well measured and reported for Z-dol, Z-tetraol, and ZTMD lubricants, the thin-film properties for viscosity and evaporation for the latter two lubricants are not found in the literature. Accordingly, we estimated these values for Z-tetraol and ZTMD as discussed in Chapter 4. This is a preliminary step towards the characterization of these lubricants which can be significantly improved by the future experiments.

   Based on lubrication theory, the lubricant dynamics can be described in two stages. First, the disk is exposed to the laser and the lubricant depletes. In the second stage, the laser is removed and the depleted lubricant reflows and recovers to the uniform profile. We found that ZTMD shows a better depletion behavior due to its improved disjoining pressure properties and significantly higher viscosity. Especially, for the sub-nanometer lubricant thicknesses this lubricant shows almost no depletion. For reflow, we found that Z-tetraol and ZTMD show much longer recovery times than Z-dol. The recovery time for these two lubricants could even take longer than 5 to 10ms which means that the lubricant depletion is not fully recovered prior to the next laser exposure, after one disk revolution. Additionally, we found a trade-off between the depletion intensity and the recovery time when considering the viscosity. So, a viable solution for the lubricants under HAMR conditions is to modify the disjoining pressure properties with higher values for disjoining pressure derivative to improve the lubricant's ability to resist against disturbances and increase the recovery speed

at the same time.

The second major approach of this dissertation is to investigate the effect of viscoelasticity on the lubricants behavior under HAMR conditions.

The viscoelastic behavior of PFPE lubricants under HAMR conditions is very complicated since it depends greatly upon the local temperature. In the case of HAMR, non-uniform temperature not only affects the viscosity and surface tension properties, but also has a large impact on the Maxwell relaxation time. Depending on the timescale of the problem, the lubricant responds differently inside the thermal spot and outside of it, exhibiting a range of behaviors from purely viscous to purely elastic ones. We developed a new FEA approach to simulate the viscoelastic behavior of the lubricants, including all of the stated complexities. We showed that this new analysis predicts expected results for the entire viscoelastic domain $(0 < De < \infty)$.

Along with the FEA approach, we also developed a modified version of a viscoelastic lubrication equation. However, this viscoelastic lubrication equation is numerically stable only for nearly viscous Maxwell fluids, with small Deborah numbers and large laser spot sizes. Both methods developed here show that the viscoelastic effects grow significantly as the laser spot size decreases. This suggests that the tradition of modeling the viscoelastic HDD lubricants using lubrication theory is not valid for the HAMR target of $L = 20nm$ laser spot size.

The results of our viscoelastic simulations using a FEA approach for $L = 20nm$ suggest that the lubricant behaves similar to a purely elastic solid at this limit. The forcing on the lubricant at this limit occurs so rapidly that the stress does not have enough time to relax. Accordingly, the lubricant depletion recovers instantaneously as soon as the laser effects disappear. Therefore, considering the viscoelastic effects, this study predicts that lubricant flow due to thermo-capillary effects will not be a significant issue in the development of the HAMR technology. Rather, the future research should concentrate more on the thermal degradation and evaporation of the HAMR lubricants as other sources of depletion.

11.2   Future Work

Though not presented in this study, we have investigated the effect of the lubricant thickness on the inter-molecular forces between the slider and the disk. For the new generation of TFC sliders, the presence of the lubricant does not modify the slider's dynamics significantly because the area of active inter-molecular interaction between the slider and the disk is very small for this kind of modern sliders.

The lubrication theory in this work predicts the depletion intensity and recovery time for Z-dol, Z-tetraol, and ZTMD. These predictions can be verified by future experiments and Molecular Dynamics simulations.

The theory of viscoelasticity predicts the lubricants to behave nearly elastically for the small laser spots as discussed in Chapter 10. Accordingly, future experiments and MD simulations need to verify this prediction as the laser spot size approaches the 20nm target for HAMR. In this study, we used the Maxwell relaxation time for the bulk Z-tetraol while studies show that the relaxation time increases for the thin-films. Accordingly, better measurements can increase the accuracy of the Maxwell relaxation time which has a significant effect on

the lubricant's behavior. In the current analysis, a single stage Maxwell model is used to describe the constitutive behavior of the material which can be improved by considering the effect of the non-dominant stages in the future. Also, the non-linear disjoining pressure for the FEA model was reduced to a bi-linear form which can be improved by taking into account the effect of disjoining pressure derivative. This enables us to add the effect of polar disjoining pressure to the model as well.

The FEA method developed in this work is a new concept, and throughout the dissertation we showed that it matches the results of the lubrication theory when the viscoelastic effects are disabled. The FEA code seems to have a great performance compared to the previous lubrication theory analysis for the lubricant in the depletion stage. As a result, it can be used more widely even for the viscous lubricants.

Bibliography

[1] IBM. *IBM Archives: IBM 350 disk storage unit.* https://www-03.ibm.com/ibm/history/exhibits/storage/storage_350.html. Retrieved 2016-12-16.

[2] *HDD vs. SSD.* http://www.diffen.com/difference/HDD_vs_SSD. Retrieved 2016-12-16. 2012.

[3] *Hard Drive Data Recovery Glossary.* http://www.newyorkdatarecovery.com/hard-drive-glossary.html. Retrieved 2016-12-16. 2011.

[4] Aleksey Meyev. *SSD, i-RAM and Traditional Hard Disk drives.* http://www.xbitlabs.com/articles/storage/display/ssd-iram.html. Retrieved 2016-12-16. Apr. 2008.

[5] Charles M. Kozierok. *The PC Guide: Spindle Speed.* http://www.pcguide.com/ref/hdd/perf/perf/spec/postransSpindle-c.html. Retrieved 2016-12-16. Apr. 2001.

[6] Andrew Ku. *Investigation: Is Your SSD More Reliable Than A Hard Drive?* http://www.tomshardware.com/reviews/ssd-reliability-failure-rate,2923-4.html. Retrieved 2016-12-16. July 2011.

[7] F Talke and R Tseng. "An experimental investigation of the effect of medium thickness and transducer spacing on the read-back signal in magnetic recording systems". In: *IEEE Transactions on Magnetics* 9.2 (1973), pp. 133–139.

[8] Toshiba Press Release. *Toshiba Leads Industry in Bringing Perpendicular Data Recording to HDD.* http://www.toshiba.co.jp/about/press/2004_12/pr1401.htm. Retrieved 2016-12-16. Dec. 2004.

[9] Mahmoud A Fowzy. *PFPE, A unique lubricant for a unique application.* Tech. rep. DTIC Document, 1998.

[10] Ganping Ju, Yingguo Peng, Eric KC Chang, Yinfeng Ding, Alexander Q Wu, Xiaobin Zhu, Yukiko Kubota, Timothy J Klemmer, Hassib Amini, Li Gao, et al. "High Density Heat-Assisted Magnetic Recording Media and Advanced Characterization—Progress and Challenges". In: *IEEE Transactions on Magnetics* 51.11 (2015), pp. 1–9.

[11] *International Technical Roadmap: Magnetic Data Storage - the technology of magnetic hard disk drives (HDDs).* Tech. rep. IDEMA Advanced Storage Technology Committee (ASTC), 2013.

[12] "Lubricant Additives: Chemistry and Applications". In: ed. by Tom E Karis and Leslie R Rudnick. CRC Press, 2009. Chap. 22, pp. 523–584.

[13]   X-C Guo, B Knigge, B Marchon, RJ Waltman, M Carter, and J Burns. "Multidentate functionalized lubricant for ultralow head/disk spacing in a disk drive". In: *Journal of applied physics* 100.4 (2006), p. 044306.

[14]   Lin Wu. "Modelling and simulation of the lubricant depletion process induced by laser heating in heat-assisted magnetic recording system". In: *Nanotechnology* 18.21 (2007), p. 215702.

[15]   Joanna Bechtel Dahl and David B Bogy. "Lubricant flow and evaporation model for heat-assisted magnetic recording including functional end-group effects and thin film viscosity". In: *Tribology Letters* 52.1 (2013), pp. 27–45.

[16]   Joanna Bechtel Dahl and David B Bogy. "Simulation of lubricant recovery after heat-assisted magnetic recording writing". In: *Tribology Letters* 52.1 (2013), pp. 163–174.

[17]   Alejandro Rodriguez Mendez and David B Bogy. "Lubricant flow and accumulation on the slider's air-bearing surface in a hard disk drive". In: *Tribology Letters* 53.2 (2014), pp. 469–476.

[18]   Michael A Scarpulla, C Mathew Mate, and Malika D Carter. "Air shear driven flow of thin perfluoropolyether polymer films". In: *The Journal of chemical physics* 118.7 (2003), pp. 3368–3375.

[19]   B Marchon and Y Saito. "Lubricant thermodiffusion in heat assisted magnetic recording". In: *IEEE Transactions on Magnetics* 48.11 (2012), pp. 4471–4474.

[20]   D Dowson. "A generalized Reynolds equation for fluid-film lubrication". In: *International Journal of Mechanical Sciences* 4.2 (1962), pp. 159–170.

[21]   Lin Wu and Frank E Talke. "Modeling laser induced lubricant depletion in heat-assisted-magnetic recording systems using a multiple-layered disk structure". In: *Microsystem technologies* 17.5-7 (2011), pp. 1109–1114.

[22]   C Mathew Mate. "Spreading kinetics of lubricant droplets on magnetic recording disks". In: *Tribology Letters* 51.3 (2013), pp. 385–395.

[23]   Robert J Waltman. "Z-Tetraol Reflow in Heat-Assisted Magnetic Recording". In: *Tribology Online* 11.1 (2016), pp. 50–60.

[24]   Robert J Waltman. "Duty Cycle Effects in Z-Tetraol Reflow in Heat-Assisted Magnetic Recording". In: *Tribology Online* 11.4 (2016), pp. 503–511.

[25]   Xiaoding Ma, J Gui, L Smoliar, K Grannen, B Marchon, MS Jhon, and CL Bauer. "Spreading of perfluoropolyalkylether films on amorphous carbon surfaces". In: *The Journal of chemical physics* 110.6 (1999), pp. 3129–3137.

[26]   Adam P Bowles, Yiao-Tee Hsia, Paul M Jones, James W Schneider, and Lee R White. "Quasi-equilibrium AFM measurement of disjoining pressure in lubricant nano-films I: Fomblin Z03 on silica". In: *Langmuir* 22.26 (2006), pp. 11436–11446.

[27]   Hiroshige Matsuoka, Koji Oka, Yusuke Yamashita, Fumihiro Saeki, and Shigehisa Fukui. "Deformation characteristics of ultra-thin liquid film considering temperature and film thickness dependence of surface tension". In: *Microsystem technologies* 17.5-7 (2011), pp. 983–990.

[28] G K Batchelor. "An introduction to fluid dynamics". In: *Cambridge University Press. Cambridge. UK* 515 (1967), P13.

[29] Jacob N Israelachvili. *Intermolecular and surface forces: revised third edition.* Academic press, 2011.

[30] Nikolai V Churaev, Boris V Derjaguin, and Vladimir M Muller. *Surface forces.* Springer Science & Business Media, 2013.

[31] C Mathew Mate. "Taking a fresh look at disjoining pressure of lubricants at slider-disk interfaces". In: *IEEE Transactions on Magnetics* 47.1 (2011), pp. 124–130.

[32] GW Tyndall, PB Leezenberg, RJ Waltman, and J Castenada. "Interfacial interactions of perfluoropolyether lubricants with magnetic recording media". In: *Tribology Letters* 4.2 (1998), pp. 103–108.

[33] RJ Waltman and H Deng. "Low molecular weight Z-Tetraol boundary lubricant films in hard disk drives". In: *Advances in Tribology* 2012 (2012).

[34] RJ Waltman. "Autophobic dewetting of Z-tetraol perfluoropolyether lubricant films on the amorphous nitrogenated carbon surface". In: *Langmuir* 20.8 (2004), pp. 3166–3172.

[35] TE Karis and GW Tyndall. "Calculation of spreading profiles for molecularly-thin films from surface energy gradients". In: *Journal of non-newtonian fluid mechanics* 82.2 (1999), pp. 287–302.

[36] Bruno Marchon. "Lubricant design attributes for subnanometer head-disk clearance". In: *IEEE Transactions on Magnetics* 45.2 (2009), pp. 872–876.

[37] TE Karis, B Marchon, V Flores, and M Scarpulla. "Lubricant spin-off from magnetic recording disks". In: *Tribology Letters* 11.3-4 (2001), pp. 151–159.

[38] RE Powell, WE Roseveare, and Henry Eyring. "Diffusion, thermal conductivity, and viscous flow of liquids". In: *Industrial & Engineering Chemistry* 33.4 (1941), pp. 430–435.

[39] Remmelt Pit, Qing-Hua Zeng, Qing Dai, and Bruno Marchon. "Experimental study of lubricant-slider interactions". In: *IEEE transactions on magnetics* 39.2 (2003), pp. 740–742.

[40] Y Ma, A Ghafari, BV Budaev, and DB Bogy. "Controlled heat flux measurement across a closing nanoscale gap and its comparison to theory". In: *Applied Physics Letters* 108.21 (2016), p. 213105.

[41] Mohammad Soroush Ghahri Sarabi and David B Bogy. "Simulation of the Performance of Various PFPE Lubricants Under Heat Assisted Magnetic Recording Conditions". In: *Tribology Letters* 56.2 (2014), pp. 293–304.

[42] Solvay Solexis. *Fomblin Z Derivatives Product Data Sheet.* http://bikvar.ru/Fombl/Magn_disk.pdf. Retrieved 2017-2-21. Dec. 2002.

[43] Shaomin Xiong and David B Bogy. "Experimental study of head-disk interface in heat-assisted magnetic recording". In: *IEEE Transactions on Magnetics* 50.3 (2014), pp. 148–154.

[44]   Haoyu Wu, Shaomin Xiong, Sripathi Canchi, Erhard Schreck, and David Bogy. "Nanoscale heat transfer in the head-disk interface for heat assisted magnetic recording". In: *Applied Physics Letters* 108.9 (2016), p. 093106.

[45]   Hyun I Kim, C Mathew Mate, Kelly A Hannibal, and Scott S Perry. "How disjoining pressure drives the dewetting of a polymer film on a silicon surface". In: *Physical review letters* 82.17 (1999), p. 3496.

[46]   Robert J Waltman, Hong Deng, Yu-Chen Wu, and Hiroyuki Matsumoto. "Boundary Lubricant Film Properties versus Molecular Polarity of Perfluoropolyethers Containing a Pendant Chain". In: *Tribology Online* 7.1 (2012), pp. 41–45.

[47]   GW Tyndall, RJ Waltman, and DJ Pocker. "Concerning the interactions between Zdol perfluoropolyether lubricant and an amorphous-nitrogenated carbon surface". In: *Langmuir* 14.26 (1998), pp. 7527–7536.

[48]   Alejandro Rodriguez Mendez and David B Bogy. "Lubricant Dewetting on the Slider's Air-Bearing Surface in Hard Disk Drives". In: *Tribology Letters* 61.3 (2016), pp. 1–11.

[49]   B Marchon, X-C Guo, T Karis, H Deng, Q Dai, J Burns, and Robert Waltman. "Fomblin multidentate lubricants for ultra-low magnetic spacing". In: *IEEE transactions on magnetics* 42.10 (2006), pp. 2504–2506.

[50]   Haoyu Wu, Alejandro Rodriguez Mendez, Shaomin Xiong, and David B Bogy. "Lubricant reflow after laser heating in heat assisted magnetic recording". In: *Journal of Applied Physics* 117.17 (2015), 17E310.

[51]   Yansheng Ma, Xiuying Chen, and Bo Liu. "Experimental study of lubricant depletion in heat assisted magnetic recording over the lifetime of the drive". In: *Tribology Letters* 47.2 (2012), pp. 175–182.

[52]   Kyosuke Ono. "Diffusion equation for spreading and replenishment in submonolayer lubricant film". In: *Tribology Letters* 57.2 (2015), pp. 1–14.

[53]   Shintaro Itoh, Kenji Fukuzawa, Yuya Hamamoto, Hedong Zhang, and Yasunaga Mitsuya. "Fiber wobbling method for dynamic viscoelastic measurement of liquid lubricant confined in molecularly narrow gaps". In: *Tribology Letters* 30.3 (2008), pp. 177–189.

[54]   Richard Christensen. *Theory of viscoelasticity: an introduction*. Elsevier, 2012.

[55]   Malcolm L Williams, Robert F Landel, and John D Ferry. "The temperature dependence of relaxation mechanisms in amorphous polymers and other glass-forming liquids". In: *Journal of the American Chemical society* 77.14 (1955), pp. 3701–3707.

[56]   G Marchionni, G Ajroldi, and G Pezzin. "Molecular weight dependence of some rheological and thermal properties of perfluoropolyethers". In: *European polymer journal* 24.12 (1988), pp. 1211–1216.

[57]   RE Powell, WE Roseveare, and Henry Eyring. "Diffusion, thermal conductivity, and viscous flow of liquids". In: *Industrial & Engineering Chemistry* 33.4 (1941), pp. 430–435.

[58] Soroush Sarabi and David B Bogy. "Effect of Functional End-Groups on the Lubricant Recovery After Heat-Assisted Magnetic Recording (HAMR) Writing". In: *ASME 2016 Conference on Information Storage and Processing Systems*. American Society of Mechanical Engineers. 2016, V001T01A021–V001T01A021.

[59] M Reiner. "The deborah number". In: *Physics today* 17.1 (1964), p. 62.

[60] Alexander Oron, Stephen H Davis, and S George Bankoff. "Long-scale evolution of thin liquid films". In: *Reviews of modern physics* 69.3 (1997), p. 931.

[61] JA Tichy. "Non-Newtonian lubrication with the convected Maxwell model". In: *Journal of tribology* 118.2 (1996), pp. 344–348.

[62] Dennis A Siginer. *Stability of non-linear constitutive formulations for viscoelastic fluids*. Springer, 2014.

[63] "Complex Fluids in Biological Systems: Experiment, Theory, and Computation". In: ed. by Alexander Morozov and Saverio Spagnolie. Springer, 2014. Chap. 1.